UCSF
UC San Francisco Electronic Theses and Dissertations

Title
The Role of Apoptosis in Differentiation and Disease

Permalink
https://escholarship.org/uc/item/3v92x78c

Author
Wang, Eric

Publication Date
2015

Peer reviewed|Thesis/dissertation

eScholarship.org Powered by the California Digital Library
University of California

The Role of Apoptosis in Differentiation and Disease

by

Eric S. Wang

DISSERTATION

Submitted in partial satisfaction of the requirements for the degree of

DOCTOR OF PHILOSOPHY

in

Biomedical Sciences

in the

GRADUATE DIVISION

of the

UNIVERSITY OF CALIFORNIA, SAN FRANCISCO

Copyright 2015

by

Eric S. Wang

I dedicate my dissertation to my family. Thanks for all of the support!

ACKNOWLEDGEMENTS

First, I'd like to thank my dad for all of his support, and especially for always letting me come home and escape from lab whenever I needed.

Secondly, I'd like to thank my thesis committee members, Eric Huang, Andrei Goga, and Doug Gould, for all of their scientific input and support.

I would also like to thank some of the amazing scientists with whom I have collaborated: Robert Blelloch and Andrei Goga, for their assistance with the embryonic stem cell story (Chapter 2) – their technical expertise in this area has been incredibly helpful, and they've been very generous with sharing data, and reagents, and even manpower from their own labs; and Feroz Papa and Doug Gould, for their generous help and support on the IRE1α story (Chapter 3) – Feroz's creativity and Doug's invaluable knowledge of the retina have both been extremely helpful in pushing this project forward.

I also want to thank the members of the Oakes lab, past and present (Nikki Reyes, Katie Austgen, Debbie Caswell, JP Upton, Jason Nguyen, Jenny Qi, Annie Hiniker, Paul Moore, Elizabeth Earley, and Adrienne Stormo) for making my time in lab as enjoyable as it was. Grad school is hard, but getting to spend it with all of you has been a blast.

Finally, I would first like to thank my thesis advisor, Scott Oakes, for all of his help and support during my graduate school career. Scott has been a fantastic mentor, always giving me the freedom to pursue different ideas but also making sure that I stayed on track. He's been incredibly patient with me when things didn't work, and has

had the creativity and insight to chase after new exciting topics. It has been great to have a mentor like Scott who makes everything go as smoothly as possible.

Chapter 3 of this thesis is a reprint of the material as it appears in “Allosteric inhibition of the IRE1α RNase preserves cell viability and function during endoplasmic reticulum stress.” Rajarshi Ghosh, Likun Wang, Eric S. Wang, *et al*. Cell. 2014 Jul 31;158(3):534-48.

The Role of Apoptosis in Differentiation and Disease

By

Eric S. Wang

ABSTRACT

Apoptosis is a highly conserved form of programmed cell death in multicellular organisms where a cell activates caspase proteases to trigger its own demise. It has critical functions under physiological conditions in removing superfluous or damaged cells from a healthy organism. However, dysregulated apoptosis plays an important role in diseases: improper or elevated apoptosis leads to diseases of cell loss, such as diabetes or neurodegeneration, while deficiencies in apoptosis can contribute to tumor cell growth and survival.

While the importance of apoptosis during late embryogenesis is well-established, its function during the earliest stages of development, namely the exit of embryonic stem cells (ESC) from the pluripotent state, is unclear. Here, I discovered that apoptosis plays a critical role in removing slow-differentiating murine ESC from the total cell population. This is initiated by p53-dependent upregulation of the Fas death receptor on straggling ESCs, which then triggers apoptosis specifically in these cells. An inability to initiate apoptosis, by transient knockdown or genetic deletion of components of this pathway, causes retention of slow-differentiating ESCs and a global delay in differentiation, both *in vitro* and in an *in vivo* teratoma model. Thus, apoptosis is crucial in promoting the efficient differentiation of ESCs.

While apoptosis is important for normal development, elevated levels due to cellular stress can cause inappropriate cell loss and degeneration, leading to disease. One such example is retinitis pigmentosa, an inherited disease where rod photoreceptors are progressively lost from the neural retina, eventually leading to blindness. There is increasing evidence that accumulation of unfolded proteins within the endoplasmic reticulum (ER) of rod photoreceptors causes ER stress and subsequent cell death. Here, I utilize a novel small molecule inhibitor to show that inhibition of IRE1α, an ER transmembrane kinase/endoribonuclease that can signal both adaptation and apoptosis in response to ER stress, preserves rod photoreceptor viability and function in two rodent models of ER stress-induced photoreceptor degeneration.

These findings reveal new insights into the role of apoptosis under both normal and stressed conditions, and may have implications for human diseases such as cancer and neurodegeneration.

TABLE OF CONTENTS

List of Figures

CHAPTER 1

Introduction

CELLULAR APOPTOTIC PATHWAYS

Apoptosis, a form of programmed cell death, is an essential cellular process in multicellular organisms that removes superfluous or damaged cells both during development and to maintain homeostasis during adulthood [1]. Cells can initiate apoptosis through the extrinsic or intrinsic apoptotic pathways. In the extrinsic pathway, ligands such as FasL or TRAIL bind to their cognate death receptors on the cell surface, triggering the recruitment of adaptors proteins to form a Death Inducing Signaling Complex (DISC). This complex then recruits and activates initiator caspases (e.g. Caspase-8,-10), which in turn activate effector caspases, such as Caspase-3 (CASP3) [2].

In contrast, initiation of the intrinsic apoptotic pathway is controlled by the levels of pro- and anti-apoptotic BCL-2 family proteins. When stresses such as DNA damage or oxidative stress tip the balance in favor of apoptosis, BAX and BAK, two pro-apoptotic members of the BCL-2 family, oligomerize and permeabilize the outer mitochondrial membrane [3]. This results in the release of pro-apoptotic factors such as cytochrome *c* and Smac/Diablo. Cytochrome *c* forms a complex with Apaf-1 and Caspase-9 to generate the apoptosome, while Smac/Diablo binds to and inactivates members of the Inhibitor of Apoptosis (IAP) family of proteins [2]. After activation by the apoptosome, Caspase-9 cleaves Caspase-3 and other effector caspases, setting off a proteolytic cascade that results in apoptosis [2]. BAX and BAK are known as the

“gatekeepers” to the mitochondrial-dependent apoptotic pathway, as double deletion of BAX and BAK results in essentially complete resistance to apoptosis via the intrinsic pathway [3].

The phenotypes of mice deficient for apoptotic proteins reveal the importance of apoptosis during development. For example, double deficiency in BAX and BAK leads to perinatal lethality and developmental defects, including persistence of interdigital webs and excess cells within the central nervous and hematopoietic systems [4]. Deletion of Apaf-1 also results in perinatal lethality due to exencephaly or cranioschesis, although a small percentage of mice survive to adulthood [5]. Finally, loss of Caspase-3 results in embryonic and perinatal lethality, with a dominant phenotype of hyperplasia in the central nervous system [6]. In most cases, loss of pro-apoptotic factors results in the lethal over-accumulation of cells in organ systems, indicating a crucial role of apoptosis in removing unnecessary or damaged cells during mammalian development.

THE ROLE OF APOPTOSIS IN ESC DIFFERENTIATION

Embryonic stem cells (ESCs) are cells that arise early during development and are derived from the inner cell mass of blastocysts. The defining characteristics of ESCs are self-renewal and pluripotency, or the ability to differentiate into cell types of all three germ layers [7]. Maintenance of the pluripotent state in ESCs has been ascribed to the transcription factors Oct4, Sox2, and Nanog [8]. Evidence suggests that these core transcription factors form an autoregulatory loop where they positively promote their own expression, upregulate expression of genes that help maintain a pluripotent state, and repress expression of lineage-specific genes [8].

Given their ability to propagate indefinitely and to differentiate into any cell type, ESCs have been heavily investigated for their potential role regenerative therapy, especially for degenerative diseases and tissue replacement. However, the utility of ESCs is not restricted to their therapeutic potential; ESCs also serve as an *in vitro* system where it is possible to study the molecular mechanisms of cellular differentiation and to model diseases after directed differentiation. Although much has been learned about the basic biology of ESCs, many important questions remain unanswered regarding the regulation of their differentiation.

Interestingly, proteins involved in apoptosis have been implicated in playing key roles during differentiation [9, 10]. For instance, a recent study reported that under differentiation conditions, ESCs activate CASP3 to promote differentiation without inducing apoptosis by cleaving the pluripotency factor Nanog [9]. Others have also reported that caspases have non-apoptotic functions during differentiation. For instance, the effector caspase drICE is required for sperm differentiation in *Drosophila* [11]. Similarly, Caspase-3 is necessary for the terminal differentiation of erythroid cells and epidermal keratinocytes in humans [12, 13]. In contrast, several groups have reported that apoptosis does occur during differentiation. For example, one study demonstrated that ESCs undergo apoptosis after withdrawal of the pluripotency-promoting cytokine leukemia inhibitory factor (LIF) [14], and another report found that apoptosis occurs during directed differentiation of ESCs into cardiomyocytes [15]. Therefore, it remains unclear whether apoptosis has critical functions during ESC differentiation.

Recently, single cell studies have revealed that ESCs are not homogeneous, even when cultured in conditions that promote pluripotency. For example, several studies have shown that Nanog and Oct4 expression do not always occur synchronously [16, 17]. Moreover, studies using fluorescent-tagged Nanog have demonstrated that not all cells within a pluripotent ESC culture express Nanog [16, 18]. Thus, ESCs exhibit striking heterogeneity, and this non-uniformity could have functional effects. Indeed, some have speculated that a mix of “more pluripotent” and “less pluripotent” cells within a population would allow the total population to both efficiently maintain a pluripotent state under appropriate conditions and also to quickly differentiate when induced to do so (reviewed in [17]).

This suggests that ESCs would need some mechanism to efficiently eliminate slowly differentiating cells, and apoptosis is a prime candidate for playing this role. To evaluate the potential functions of apoptosis and the intrinsic apoptotic pathway in ESC differentiation, we generated murine ESCs doubly deficient for *Bax* and *Bak*. Using these cells, we demonstrate that apoptosis occurs in a BAX/BAK-dependent manner during ESC differentiation, and that cell death primarily occurs in a subpopulation of poorly differentiating ESCs. Thus, we show that apoptosis serves to eliminate slowly differentiating cells to enhance the efficiency and robustness of ESC differentiation at the population level.

ENDOPLASMIC RETICULUM STRESS

While apoptosis occurs as a part of the normal developmental program, it can also be triggered in response to cellular injury, such as endoplasmic reticulum (ER)

stress. The ER is the major site of protein folding for transmembrane or secreted proteins, which together represent over a third of all proteins made in the cell [19]. Certain specialized cells, such as the pancreatic β-cell or retinal photoreceptors, have extremely high protein folding burdens. For example, each pancreatic β-cell is estimated to release nearly 1 million molecules of insulin per minute [20]. Proteins destined for the secretory pathway are co-translationally translocated into the ER lumen, where they are post-translationally modified by enzymes such as chaperones, glycosylating enzymes, and oxidoreductases, and ultimately folded into their proper shape [21, 22].

A variety of insults can elevate the protein-folding demand on a cell, including genetic mutations that cause protein misfolding, oxidative stress and hypoxia, chemical insults, or differentiation into professional secretory cells (i.e. pancreatic β-cell or antibody-secreting plasma cells). Under these conditions, cells experience “ER stress” and activate a set of signaling pathways known as the unfolded protein response (UPR). Under low levels of ER stress, UPR signaling will promote adaption by increasing the protein folding capacity and reducing the protein folding burden on the ER (“adaptive” UPR) [23]. However, if levels of ER stress are irremediable, then the UPR switches strategies and instead signals cell death (“terminal” UPR) [24].

The three major signal transducers of the UPR are the ER transmembrane proteins ATF6, PERK, and IRE1α. During ER stress, ATF6 translocates from the ER to the Golgi, where it is cleaved by proteases to release its cytoplasmic domain (ATF6(N)), a transcription factor that enters the nucleus to activate transcription of target genes that enhance ER protein folding capacity [25, 26]. When PERK senses unfolded proteins through its ER lumenal domain, its cytosolic kinase domain phosphorylates eukaryotic

translation initiation factor 2α (eIF2α), inhibiting global cap-dependent translation and thereby reducing the protein-folding load on the ER [27]. Under irremediable ER stress, PERK can induce ATF4-dependent upregulation of the pro-apoptotic transcription factor CHOP [28, 29].

Like PERK, IRE1α also senses unfolded proteins through its ER lumenal domain, either indirectly due to dissociation of the ER chaperone BiP or by directly binding to misfolded proteins [30, 31]. Oligomerization of IRE1α's lumenal domain causes kinase *trans*-autophosphorylation, which induces activation of the RNase. During low levels of ER stress, IRE1α's RNase removes a 26 nucleotide intron from the mRNA of the transcription factor *Xbp1*. Re-ligation allows for translation of full-length spliced XBP1 protein (XBP1s) [32, 33], which promotes adaption to low levels of ER stress by upregulating transcription of ER resident proteins that promote protein folding [34]. However, during irremediable levels of ER stress, IRE1α becomes hyperphosphorylated, promoting formation of higher-order oligomers and relaxed RNase specificity. This hyperactivated RNase cleaves and degrades ER-localized mRNAs [35-37], which may at first have a homeostatic effect by reducing the protein-folding burden on the ER. However, continual degradation of important factors for the ER, such as chaperones, eventually causes significant loss of ER function.

Several labs have now demonstrated that ER stress-induced apoptosis is mediated through the intrinsic apoptotic pathway, as genetic deletion of *Bax* and *Bak* confers significant protection against ER stress [38, 39]. Previous work demonstrated that Caspase-2 (CASP2) cleavage of the BH3-only protein BID is a key trigger for activation of BAX and BAK during severe ER stress [40]. Interestingly, IRE1α was found

to be responsible for the upregulation and activation of CASP2 by cleaving microRNAs (miRNAs) responsible for repressing CASP2 levels [41]. Moreover, IRE1α cleaves miRNAs that repress levels of thioredoxin-interacting protein (TXNIP), and increased levels of TNXIP can induce activation of the inflammasome and pyroptotic cell death [42].

TARGETING THE UPR IN DEGENERATIVE DISEASES

Chronic ER stress and UPR signaling have increasingly been implicated to play important roles in the pathogenesis of a variety of human diseases. This is especially true for neurodegenerative diseases, where protein misfolding and aggregation (and subsequent UPR signaling) are common hallmarks (reviewed in [43]). For example, some familial cases of amyotrophic lateral sclerosis (ALS) are caused by toxic gain-of-function mutations in superoxide dismutase 1 (SOD1), and these mutations lead to protein aggregation and subsequent ER stress [44]. In fact, PERK activation was found to be selectively upregulated in the subset of motor neurons that are most susceptible to degeneration in a murine model of familial ALS, well before motor neuron degeneration [45]. A second example is retinitis pigmentosa (RP), a degenerative disease where rod photoreceptors of the neural retina are gradually lost. RP can be caused by mutations in the rod-specific photopigment *Rhodopsin*, and there is strong evidence of IRE1α hyperactivation in rod photoreceptors in multiple murine models of RP [46-48].

As the UPR effectors play important roles in the pathogenesis of a variety of diseases, there has been increasing interest in developing small molecule inhibitors that target them, especially the kinases PERK and IRE1α. For instance, GlaxoSmithKline

recently developed highly specific and potent inhibitors of PERK, which were demonstrated to have a therapeutic effect in delaying the loss of neurons in a murine model of prion-mediated neurodegeneration [49].

RETINITIS PIGMENTOSA (RP)

There is accumulating evidence that ER stress plays an important role in several forms of RP, an inherited disease that results in the degeneration of photoreceptors in the neural retina. RP can be caused by mutations in over 60 genes, and can be inherited in an autosomal dominant (30-40%), autosomal recessive (50-60%) or X-linked (5-15%) fashion; roughly 100,000 Americans (and one in 4,000 people globally) suffer vision loss due to RP [50].

Although RP has a variety of genetic causes, several common clinical features are present in all RP cases, including deposition of retinal pigmentation, photoreceptor dysfunction, and progressive photoreceptor loss. During the typical course of disease, rod photoreceptors are lost first, resulting in reduced ability to see in low-light conditions ("night blindness"). This is followed by progressive loss of peripheral vision, which worsens and eventually results in blindness. Although a large percentage of the genetic causes of RP have been identified, no disease-modifying therapies have been approved [51].

One of the most commonly mutated genes in RP is *Rhodopsin*, a G protein-coupled receptor expressed in rod photoreceptors that is essential in phototransduction. Rhodopsin is made up of the protein opsin, which is folded and coupled to 11-*cis*-retinal in the ER to form the holoenzyme rhodopsin [52]. Rhodopsin is then transported to

discs in the outer segment of rod photoreceptors where it functions in phototransduction.

Many mutations in *Rhodopsin* can cause RP, and they have been organized into several classes [53, 54]. Class II mutations, which occur throughout the coding region of *Rhodopsin*, result in retention of misfolded Rhodopsin in the ER and subsequent aggregation, which ultimately causes ER stress. The prototypical Class II *Rhodopsin* mutation is P23H, which is also the most common cause of autosomal dominant RP in the US [53, 54].

Activation of IRE1α has been documented in multiple models of retinal degeneration, including P23H rhodopsin [46, 47, 55, 56]. As hyperactivation of IRE1α and subsequent terminal UPR signaling can lead to cell death, we sought to determine whether pharmacological inhibition of IRE1α would be sufficient to reduce ER stress-induced degeneration. We found that intravitreal delivery of an advanced IRE1α kinase inhibitor called KIRA6 could improve cell survival and preserve cellular function in two models of ER stress-induced retinal degeneration, including a P23H rhodopsin transgenic rat model of RP. In sum, our data demonstrate that inhibiting IRE1α's terminal UPR outputs can promote cell survival and ameliorate ER stress-induced neurodegeneration in an *in vivo* setting.

REFERENCES

1. Meier, P., Finch, A., and Evan, G. (2000). Apoptosis in development. Nature *407*, 796-801.
2. Danial, N.N., and Korsmeyer, S.J. (2004). Cell Death: Critical Control Points. Cell *116*, 205-219.
3. Wei, M.C., Zong, W.-X., Cheng, E.H.Y., Lindsten, T., Panoutsakopoulou, V., Ross, A.J., Roth, K.A., MacGregor, G.R., Thompson, C.B., and Korsmeyer, S.J. (2001). Proapoptotic BAX and BAK: A Requisite Gateway to Mitochondrial Dysfunction and Death. Science *292*, 727-730.
4. Lindsten, T., Ross, A.J., King, A., Zong, W.-X., Rathmell, J.C., Shiels, H.A., Ulrich, E., Waymire, K.G., Mahar, P., Frauwirth, K., et al. (2000). The Combined Functions of Proapoptotic Bcl-2 Family Members Bak and Bax Are Essential for Normal Development of Multiple Tissues. Molecular cell *6*, 1389-1399.
5. Yoshida, H., Kong, Y.-Y., Yoshida, R., Elia, A.J., Hakem, A., Hakem, R., Penninger, J.M., and Mak, T.W. (1998). Apaf1 Is Required for Mitochondrial Pathways of Apoptosis and Brain Development. Cell *94*, 739-750.
6. Kuida, K., Zheng, T.S., Na, S., Kuan, C.-Y., Yang, D., Karasuyama, H., Rakic, P., and Flavell, R.A. (1996). Decreased apoptosis in the brain and premature lethality in CPP32-deficient mice. Nature *384*, 368-372.
7. Jaenisch, R., and Young, R. (2008). Stem Cells, the Molecular Circuitry of Pluripotency and Nuclear Reprogramming. Cell *132*, 567-582.
8. Young, Richard A. (2011). Control of the Embryonic Stem Cell State. Cell *144*, 940-954.

9. Fujita, J., Crane, A.M., Souza, M.K., Dejosez, M., Kyba, M., Flavell, R.A., Thomson, J.A., and Zwaka, T.P. (2008). Caspase Activity Mediates the Differentiation of Embryonic Stem Cells. Cell Stem Cell *2*, 595-601.

10. Yamane, T., Dylla, S.J., Muijtjens, M., and Weissman, I.L. (2005). Enforced Bcl-2 expression overrides serum and feeder cell requirements for mouse embryonic stem cell self-renewal. Proceedings of the National Academy of Sciences of the United States of America *102*, 3312-3317.

11. Arama, E., Agapite, J., and Steller, H. (2003). Caspase Activity and a Specific Cytochrome C Are Required for Sperm Differentiation in Drosophila. Developmental Cell *4*, 687-697.

12. Weil, M., Raff, M.C., and Braga, V.M.M. (1999). Caspase activation in the terminal differentiation of human epidermal keratinocytes. Current Biology *9*, 361-365.

13. Zermati, Y., Garrido, C., Amsellem, S., Fishelson, S., Bouscary, D., Valensi, F.o., Varet, B., Solary, E., and Hermine, O. (2001). Caspase Activation Is Required for Terminal Erythroid Differentiation. The Journal of experimental medicine *193*, 247-254.

14. Duval, D., Malaise, M., Reinhardt, B., Kedinger, C., and Boeuf, H. (2004). A p38 inhibitor allows to dissociate differentiation and apoptotic processes triggered upon LIF withdrawal in mouse embryonic stem cells. Cell death and differentiation *11*, 331-341.

15. Akbari-Birgani, S., Hosseinkhani, S., Mollamohamadi, S., and Baharvand, H. (2014). Delay in Apoptosome Formation Attenuates Apoptosis in mouse Embryonic Stem Cell Differentiation. The Journal of biological chemistry.

16. Chambers, I., Silva, J., Colby, D., Nichols, J., Nijmeijer, B., Robertson, M., Vrana, J., Jones, K., Grotewold, L., and Smith, A. (2007). Nanog safeguards pluripotency and mediates germline development. Nature *450*, 1230-1234.

17. Torres-Padilla, M.E., and Chambers, I. (2014). Transcription factor heterogeneity in pluripotent stem cells: a stochastic advantage. Development *141*, 2173-2181.

18. Filipczyk, A., Gkatzis, K., Fu, J., Hoppe, P.S., Lickert, H., Anastassiadis, K., and Schroeder, T. (2013). Biallelic expression of nanog protein in mouse embryonic stem cells. Cell stem cell *13*, 12-13.

19. Anelli, T., and Sitia, R. (2008). Protein quality control in the early secretory pathway. Embo J *27*, 315-327.

20. Scheuner, D., and Kaufman, R.J. (2008). The unfolded protein response: a pathway that links insulin demand with beta-cell failure and diabetes. Endocr Rev *29*, 317-333.

21. Tu, B.P., and Weissman, J.S. (2004). Oxidative protein folding in eukaryotes: mechanisms and consequences. J Cell Biol *164*, 341-346.

22. Sevier, C.S., and Kaiser, C.A. (2002). Formation and transfer of disulphide bonds in living cells. Nat Rev Mol Cell Biol *3*, 836-847.

23. Walter, P., and Ron, D. (2011). The unfolded protein response: from stress pathway to homeostatic regulation. Science *334*, 1081-1086.

24. Shore, G.C., Papa, F.R., and Oakes, S.A. (2011). Signaling cell death from the endoplasmic reticulum stress response. Current opinion in cell biology *23*, 143-149.

25. Wu, J., Rutkowski, D.T., Dubois, M., Swathirajan, J., Saunders, T., Wang, J., Song, B., Yau, G.D., and Kaufman, R.J. (2007). ATF6alpha optimizes long-term endoplasmic reticulum function to protect cells from chronic stress. Developmental cell *13*, 351-364.

26. Ye, J., Rawson, R.B., Komuro, R., Chen, X., Dave, U.P., Prywes, R., Brown, M.S., and Goldstein, J.L. (2000). ER stress induces cleavage of membrane-bound ATF6 by the same proteases that process SREBPs. Molecular cell *6*, 1355-1364.

27. Harding, H.P., Novoa, I., Zhang, Y., Zeng, H., Wek, R., Schapira, M., and Ron, D. (2000). Regulated translation initiation controls stress-induced gene expression in mammalian cells. Molecular cell *6*, 1099-1108.

28. Marciniak, S.J., Yun, C.Y., Oyadomari, S., Novoa, I., Zhang, Y., Jungreis, R., Nagata, K., Harding, H.P., and Ron, D. (2004). CHOP induces death by promoting protein synthesis and oxidation in the stressed endoplasmic reticulum. Genes & development *18*, 3066-3077.

29. McCullough, K.D., Martindale, J.L., Klotz, L.O., Aw, T.Y., and Holbrook, N.J. (2001). Gadd153 sensitizes cells to endoplasmic reticulum stress by down-regulating Bcl2 and perturbing the cellular redox state. Mol Cell Biol *21*, 1249-1259.

30. Credle, J.J., Finer-Moore, J.S., Papa, F.R., Stroud, R.M., and Walter, P. (2005). On the mechanism of sensing unfolded protein in the endoplasmic reticulum. Proceedings of the National Academy of Sciences of the United States of America *102*, 18773-18784.

31. Pincus, D., Chevalier, M.W., Aragon, T., van Anken, E., Vidal, S.E., El-Samad, H., and Walter, P. (2010). BiP binding to the ER-stress sensor Ire1 tunes the homeostatic behavior of the unfolded protein response. PLoS biology *8*, e1000415.

32. Calfon, M., Zeng, H., Urano, F., Till, J.H., Hubbard, S.R., Harding, H.P., Clark, S.G., and Ron, D. (2002). IRE1 couples endoplasmic reticulum load to secretory capacity by processing the XBP-1 mRNA. Nature *415*, 92-96.

33. Yoshida, H., Matsui, T., Yamamoto, A., Okada, T., and Mori, K. (2001). XBP1 mRNA is induced by ATF6 and spliced by IRE1 in response to ER stress to produce a highly active transcription factor. Cell *107*, 881-891.

34. Lee, A.H., Iwakoshi, N.N., and Glimcher, L.H. (2003). XBP-1 regulates a subset of endoplasmic reticulum resident chaperone genes in the unfolded protein response. Mol Cell Biol *23*, 7448-7459.

35. Han, D., Lerner, A.G., Vande Walle, L., Upton, J.P., Xu, W., Hagen, A., Backes, B.J., Oakes, S.A., and Papa, F.R. (2009). IRE1alpha kinase activation modes control alternate endoribonuclease outputs to determine divergent cell fates. Cell *138*, 562-575.

36. Hollien, J., Lin, J.H., Li, H., Stevens, N., Walter, P., and Weissman, J.S. (2009). Regulated Ire1-dependent decay of messenger RNAs in mammalian cells. The Journal of cell biology *186*, 323-331.

37. Ghosh, R., Wang, L., Wang, E.S., Perera, B.G., Igbaria, A., Morita, S., Prado, K., Thamsen, M., Caswell, D., Macias, H., et al. (2014). Allosteric Inhibition of the IRE1alpha RNase Preserves Cell Viability and Function during Endoplasmic Reticulum Stress. Cell *158*, 534-548.

38. Lindsten, T., Ross, A.J., King, A., Zong, W.X., Rathmell, J.C., Shiels, H.A., Ulrich, E., Waymire, K.G., Mahar, P., Frauwirth, K., et al. (2000). The combined functions of proapoptotic Bcl-2 family members bak and bax are essential for normal development of multiple tissues. Molecular cell *6*, 1389-1399.

39. Wei, M.C., Zong, W.X., Cheng, E.H., Lindsten, T., Panoutsakopoulou, V., Ross, A.J., Roth, K.A., MacGregor, G.R., Thompson, C.B., and Korsmeyer, S.J. (2001). Proapoptotic BAX and BAK: a requisite gateway to mitochondrial dysfunction and death. Science *292*, 727-730.

40. Upton, J.P., Austgen, K., Nishino, M., Coakley, K.M., Hagen, A., Han, D., Papa, F.R., and Oakes, S.A. (2008). Caspase-2 cleavage of BID is a critical apoptotic signal downstream of endoplasmic reticulum stress. Mol Cell Biol *28*, 3943-3951.

41. Upton, J.P., Wang, L., Han, D., Wang, E.S., Huskey, N.E., Lim, L., Truitt, M., McManus, M.T., Ruggero, D., Goga, A., et al. (2012). IRE1alpha cleaves select microRNAs during ER stress to derepress translation of proapoptotic Caspase-2. Science *338*, 818-822.

42. Lerner, A.G., Upton, J.P., Praveen, P.V., Ghosh, R., Nakagawa, Y., Igbaria, A., Shen, S., Nguyen, V., Backes, B.J., Heiman, M., et al. (2012). IRE1alpha induces thioredoxin-interacting protein to activate the NLRP3 inflammasome and promote programmed cell death under irremediable ER stress. Cell metabolism *16*, 250-264.

43. Kim, I., Xu, W., and Reed, J.C. (2008). Cell death and endoplasmic reticulum stress: disease relevance and therapeutic opportunities. Nature reviews. Drug discovery *7*, 1013-1030.

44. Nishitoh, H., Kadowaki, H., Nagai, A., Maruyama, T., Yokota, T., Fukutomi, H., Noguchi, T., Matsuzawa, A., Takeda, K., and Ichijo, H. (2008). ALS-linked mutant SOD1 induces ER stress- and ASK1-dependent motor neuron death by targeting Derlin-1. Genes & development *22*, 1451-1464.

45. Saxena, S., Cabuy, E., and Caroni, P. (2009). A role for motoneuron subtype-selective ER stress in disease manifestations of FALS mice. Nature neuroscience *12*, 627-636.

46. Chiang, W.C., Kroeger, H., Sakami, S., Messah, C., Yasumura, D., Matthes, M.T., Coppinger, J.A., Palczewski, K., LaVail, M.M., and Lin, J.H. (2014). Robust Endoplasmic Reticulum-Associated Degradation of Rhodopsin Precedes Retinal Degeneration. Molecular neurobiology.

47. Gorbatyuk, M.S., Knox, T., LaVail, M.M., Gorbatyuk, O.S., Noorwez, S.M., Hauswirth, W.W., Lin, J.H., Muzyczka, N., and Lewin, A.S. (2010). Restoration of visual function in P23H rhodopsin transgenic rats by gene delivery of BiP/Grp78.

Proceedings of the National Academy of Sciences of the United States of America *107*, 5961-5966.

48. Kroeger, H., LaVail, M.M., and Lin, J.H. (2014). Endoplasmic reticulum stress in vertebrate mutant rhodopsin models of retinal degeneration. Advances in experimental medicine and biology *801*, 585-592.

49. Moreno, J.A., Halliday, M., Molloy, C., Radford, H., Verity, N., Axten, J.M., Ortori, C.A., Willis, A.E., Fischer, P.M., Barrett, D.A., et al. (2013). Oral treatment targeting the unfolded protein response prevents neurodegeneration and clinical disease in prion-infected mice. Science translational medicine *5*, 206ra138.

50. Daiger, S.P., Sullivan, L.S., and Bowne, S.J. (2013). Genes and mutations causing retinitis pigmentosa. Clinical genetics *84*, 132-141.

51. Petrs-Silva, H., and Linden, R. (2014). Advances in gene therapy technologies to treat retinitis pigmentosa. Clinical ophthalmology *8*, 127-136.

52. Palczewski, K. (2006). G protein-coupled receptor rhodopsin. Annual review of biochemistry *75*, 743-767.

53. Sung, C.H., Davenport, C.M., Hennessey, J.C., Maumenee, I.H., Jacobson, S.G., Heckenlively, J.R., Nowakowski, R., Fishman, G., Gouras, P., and Nathans, J. (1991). Rhodopsin mutations in autosomal dominant retinitis pigmentosa. Proceedings of the National Academy of Sciences of the United States of America *88*, 6481-6485.

54. Sung, C.H., Davenport, C.M., and Nathans, J. (1993). Rhodopsin mutations responsible for autosomal dominant retinitis pigmentosa. Clustering of functional

classes along the polypeptide chain. The Journal of biological chemistry *268*, 26645-26649.

55. Lin, J.H., Li, H., Yasumura, D., Cohen, H.R., Zhang, C., Panning, B., Shokat, K.M., Lavail, M.M., and Walter, P. (2007). IRE1 signaling affects cell fate during the unfolded protein response. Science *318*, 944-949.

56. Tam, B.M., and Moritz, O.L. (2006). Characterization of rhodopsin P23H-induced retinal degeneration in a Xenopus laevis model of retinitis pigmentosa. Investigative ophthalmology & visual science *47*, 3234-3241.

CHAPTER 2

FAS-activated mitochondrial apoptosis culls stalled embryonic stem cells to promote differentiation

SUMMARY

Apoptosis is crucial to remove superfluous, damaged, or incorrectly specified cells during organogenesis in the embryo. In particular, the pro-death Bcl-2 family proteins BAX and BAK are required for mitochondrial apoptosis, and *Bax*$^{-/-}$*Bak*$^{-/-}$ mice have severe developmental defects during late gestation. Here, we show that *Bax*$^{-/-}$*Bak*$^{-/-}$ murine embryonic stem cells (ESCs) also display defects during the exit from pluripotency, both in culture and during teratoma formation. Specifically, we find that when ESCs are stimulated to differentiate, a subpopulation fails to do so and instead upregulates FAS in a p53-dependent manner to trigger BAX/BAK-dependent apoptosis. Blocking this apoptotic pathway prevents the removal of these poorly differentiated cells, resulting in the retention of cells that have not exited pluripotency. Taken together, our results provide further evidence for heterogeneity in the potential of ESCs to successfully differentiate, and reveal a novel role for apoptosis in promoting efficient ESC differentiation by culling cells that are slow to exit pluripotency.

INTRODUCTION

The intrinsic (mitochondrial) apoptotic pathway is an evolutionarily conserved cell death program shared by all higher eukaryotic cells that is triggered by a wide range of developmental cues or intracellular damage [1]. Healthy cells prevent inappropriate

activation of the intrinsic apoptotic pathway by sequestering critical pro-death components (e.g., cytochrome *c*) within mitochondria. The multi-domain pro-apoptotic BCL-2 proteins BAX and BAK serve as “gatekeepers” of outer mitochondrial membrane permeability [2, 3]. In response to internal injury (e.g., DNA damage, endoplasmic reticulum (ER) stress) or developmental signals, pro-apoptotic BH3-only proteins are activated by transcriptional upregulation and/or post-translational modifications [4]. Once activated, BH3-only proteins translocate to mitochondria where they trigger homo-oligomerization of BAX and/or BAK to permeabilize the outer mitochondrial membrane and induce the release of cytochrome *c* and other pro-death molecules [5]. Upon cytoplasmic entry, cytochrome *c* facilitates formation of the apoptosome and activation of Caspase-9 (CASP9), which in turn cleaves and activates effector caspases such as Caspase-3 (CASP3) to proteolytically dismantle the cell [6].

BAX and BAK play critical roles in triggering programmed cell death during late embryonic development, as mice doubly deficient in these two proteins generally die at approximately embryonic day 17 due to defects in neural tube closure. The rare *Bax*$^{-/-}$ *Bak*$^{-/-}$ mice that are viable at birth only survive a few weeks and possess physical abnormalities, including interdigital webbing, splenomegaly, lymphadenopathy, and imperforate vaginas in females [3]. Interestingly, animals singly deficient in either *Bax* or *Bak* have limited morphological defects, indicating that these proteins are functionally redundant in most tissues [3, 7]. Furthermore, mice genetically deficient for other key players in the intrinsic apoptotic pathway, such as Apaf-1 and CASP9, exhibit phenotypic defects that are similar to, but less dramatic than, those of *Bax*$^{-/-}$*Bak*$^{-/-}$ mice [8-11]. These results indicate that the BAX/BAK-dependent apoptotic pathway is crucial

for the later stages of mammalian development.

In contrast, the role of the mitochondrial apoptotic pathway during early embryogenesis remains poorly defined. A previous study reported that CASP3 plays a nonapoptotic role in the differentiation of murine embryonic stem cells (ESC) [12]. Conversely, other groups have found that ESCs undergo apoptosis after withdrawal of the pluripotency-promoting cytokine leukemia inhibitory factor (LIF) [13] or during differentiation into cardiomyocytes [14]. To carefully investigate the role of apoptosis and the intrinsic apoptotic pathway in ESC differentiation, we generated and analyzed *Bax*$^{-/-}$*Bak*$^{-/-}$ murine ESCs and compared them to *Casp3*$^{-/-}$ ESCs. We observed a significant delay (but not a complete block) in the differentiation of *Bax*$^{-/-}$*Bak*$^{-/-}$ and *Casp3*$^{-/-}$ ESCs either when grown in culture or during teratoma formation in immunocompromised mice. Furthermore, we found high levels of CASP3 activation and apoptosis during ESC differentiation, both of which are dependent on BAX and BAK. Moreover, we show that this apoptosis occurs primarily in a subpopulation of ESCs that fails to fully differentiate; inhibiting the removal of these unspecified cells by blocking mitochondrial apoptosis significantly delays ESC differentiation at a population level. These findings reveal a novel role for the intrinsic apoptotic pathway in removing stalled cells to enhance the efficiency and fidelity of ESC differentiation.

RESULTS

To study the effects of disabling the intrinsic apoptotic pathway on ESC differentiation, we generated ESCs deficient for *Bax* and *Bak*. As germline-deficient *Bax*$^{-/-}$*Bak*$^{-/-}$ mice generally die *in utero* [2], we utilized mice with a previously described floxed

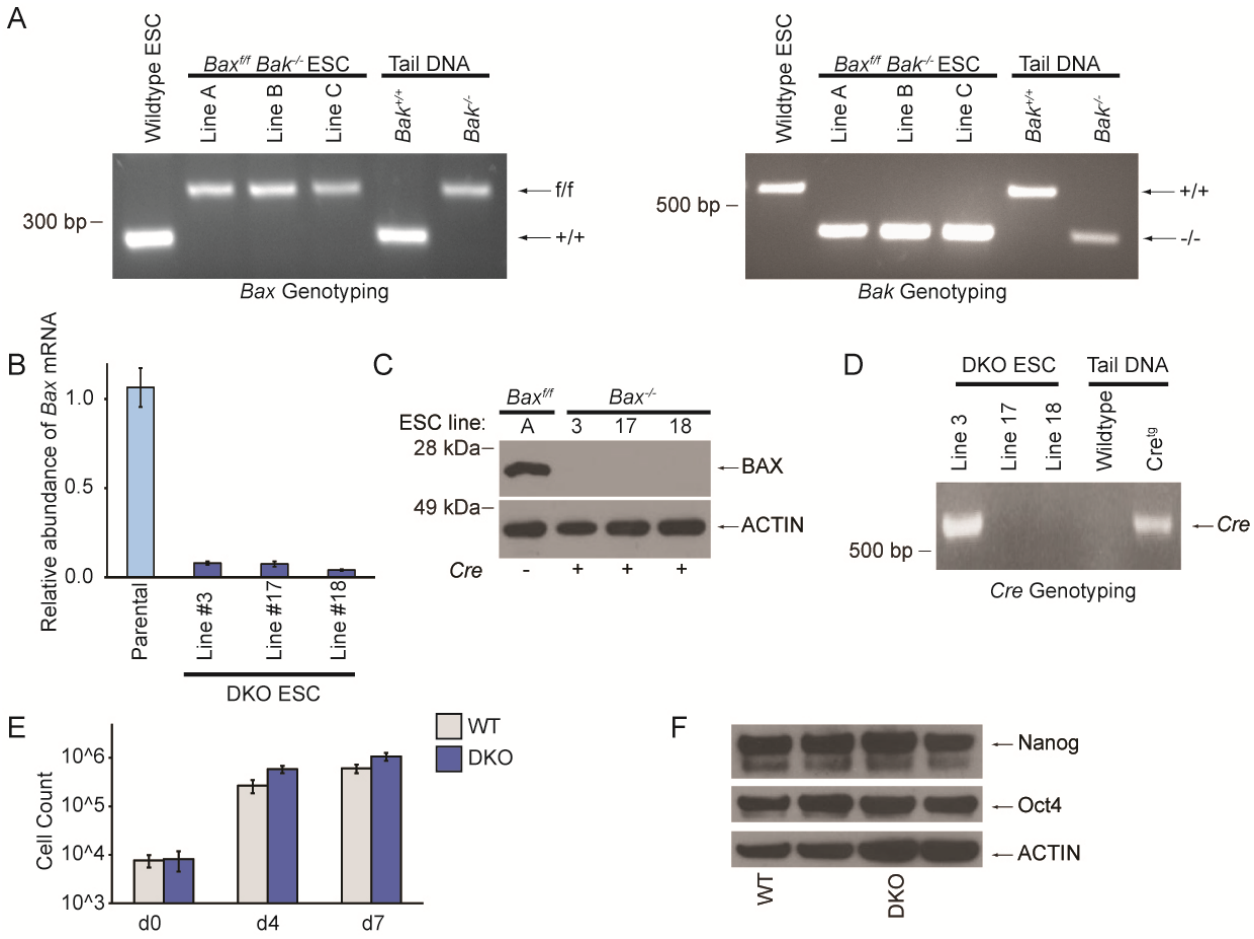

Figure 2.1. Generation of BAX/BAK-deficient embryonic stem cells.
(A) *Bax* and *Bak* genotyping results from three independent *Bax*$^{f/f}$*Bak*$^{-/-}$ ESCs lines. Wildtype ESCs are shown as a control. (B) *Bax* mRNA levels in three independently transfected lines via quantitative RT-PCR. Clones were derived from transfection of *Cre* recombinase in the parental line, "ESC line B," followed by selection in puromycin (C) BAX protein levels after *Cre* mediated excision. (D) *Cre* genotyping results in three DKO lines. DKO, *Bax*$^{-/-}$*Bak*$^{-/-}$ double knockout. (E) Cell count of undifferentiated WT and DKO ESCs over time. (F) Immunoblot of Nanog and Oct4 from undifferentiated ESCs.

(f) conditional allele of *Bax* and germline deletion of *Bak* [15]. Three different ESC lines were generated from C57BL/6 $Bax^{f/f}Bak^{-/-}$ mice (Figure 2.1A) and transiently transfected with *Cre* recombinase to obtain BAX/BAK deficient (double knockout, DKO) ESCs. The resulting three clones were screened and found to be null for *Bax* mRNA and protein expression (Figures 2.1B and 2.1C). These clones were also genotyped for *Cre* recombinase. Two of the ESC lines (DKO-17 and DKO-18) lacked stable integration of *Cre* recombinase and were chosen for further analysis (Figure 2.1D). Deletion of *Bax* and *Bak* had no observable effects on the size, shape, growth rate, or expression of the pluripotency factors Oct4 or Nanog in undifferentiated ESCs (Figure 2.1E,F).

Next, we tested whether the loss of *Bax* and *Bak* affected ESC differentiation. DKO ESCs were induced to differentiate with retinoic acid (RA) and compared to C57BL/6 wild-type ESCs ($Bax^{+/+}Bak^{+/+}$, WT), the parental cell line ($Bax^{f/f}Bak^{-/-}$), and $Casp3^{-/-}$ ESCs. We first performed colony formation assays with RA-treated ESCs and found that both DKO and $Casp3^{-/-}$ ESCs inappropriately retained the ability to form colonies that express the pluripotency marker alkaline phosphatase (AP) [16] (Figures 2.2A,B), a result consistent with a previous study reporting a role for CASP3 in ESC differentiation [12]. Interestingly, DKO ESCs showed an even greater delay in losing this pluripotency marker than $Casp3^{-/-}$ ESCs, as $Casp3^{-/-}$ ESCs failed to form AP+ colonies after 8 days of RA treatment while DKO ESCs were able to generate a few AP positive colonies even after 16 days of RA treatment. To further assess the differentiation defect in DKO ESCs, we measured mRNA levels of the pluripotency factors *Nanog* and *Oct4* [17-19]. We found that *Nanog* and *Oct4* mRNA transcript levels are approximately 2- to 3-fold higher in DKO ESCs in comparison to WT or parental cells after 1 day of RA

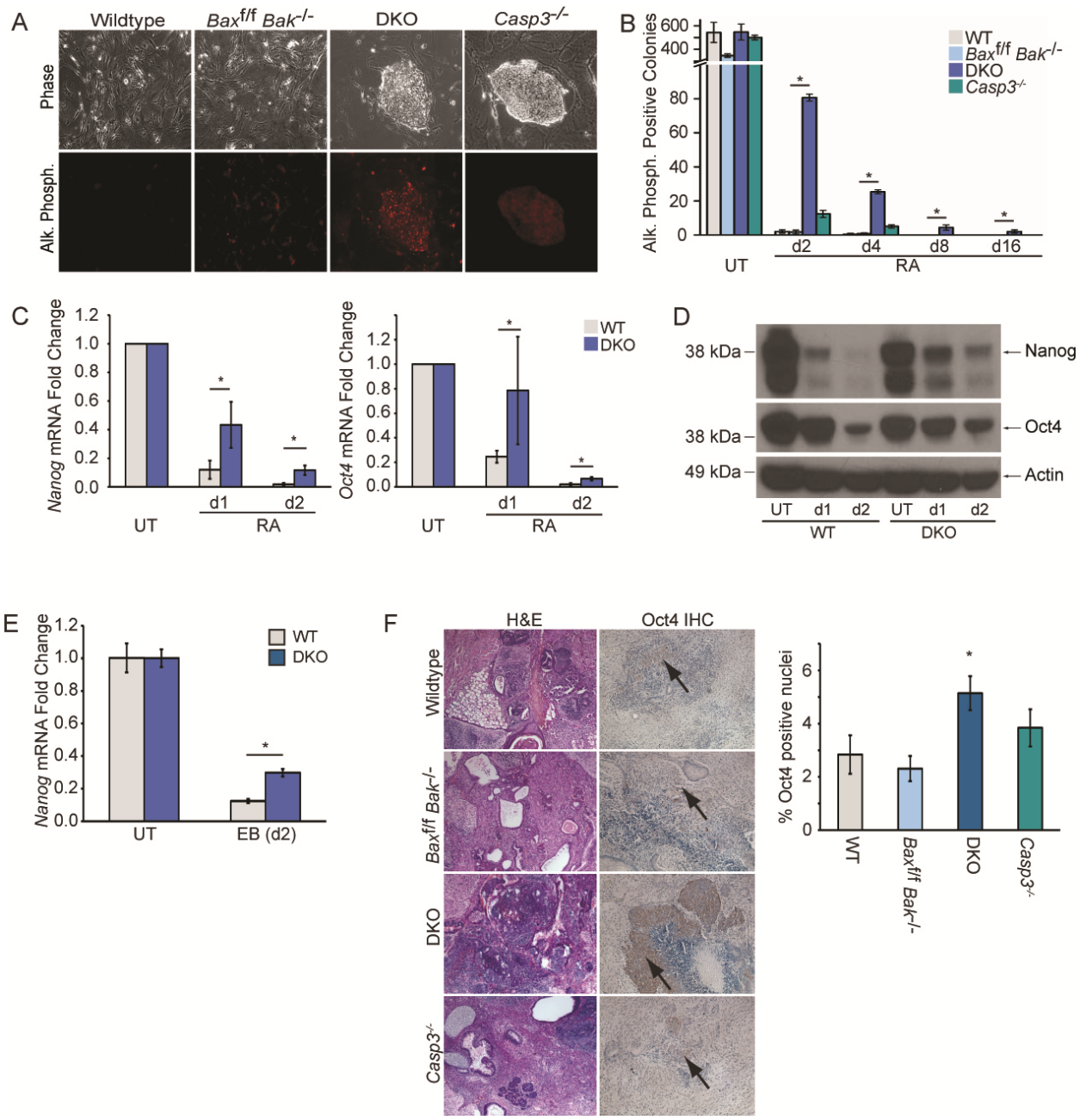

Figure 2.2. Genetic deletion of BAX and BAK results in a delay in ESC differentiation.

(A) Representative phase and fluorescent images of each ESC line stained for AP after 2 days of RA treatment. (B) Quantification of AP positive colonies during RA treatment; data plotted as mean ± SD. (C) *Nanog* and *Oct4* mRNA levels from ESCs analyzed via qPCR; data plotted as mean ± SD. (D) Immunoblot of ESC lysates for Nanog and Oct4. (E) mRNA levels of *Nanog* during EB formation. (F) Sections of teratomas stained with hematoxylin and eosin (H&E) (left panel) or for Oct4 expression (right panel), and quantification of Oct4+ nuclei. At least three independent biological samples were used for the AP colony-reforming assay, and *Nanog* and *Oct4* qPCR. * significant at $p < 0.05$ (Student t test).

treatment (Figure 2.2C). By day 2, transcript levels of *Nanog* and *Oct4* are low in both cell lines, but there is still significantly more of each in DKO relative to WT ESCs (Figure 2.2C). Similarly, loss of Oct4 and Nanog proteins is delayed in DKO ESCs during differentiation (Figure 2.2D). To determine whether this phenomenon is restricted to RA-induced differentiation, we tested whether DKO ESCs also exhibited delayed differentiation during embryoid body (EB) formation. Indeed, *Nanog* mRNA levels were elevated in DKO relative to WT ESCs 2 days after initiating EBs (Figure 2.2E). Thus, DKO ESCs exhibit a marked delay in exiting the pluripotent state *in vitro*.

Next, we tested all four lines of ESCs for their ability to undergo differentiation *in vivo* and give rise to all three germ layers during teratoma formation. ESCs were injected into immunocompromised nude mice and teratoma formation at the injection site was assessed. Hematoxylin and eosin (H&E) stains of the teratomas revealed that WT, $Bax^{f/f}$ $Bak^{-/-}$, and to a lesser extent $Casp3^{-/-}$ lines were mainly comprised of differentiated cells that represented all three germ layers (Figure 2.2F). In contrast, DKO teratomas consisted largely of sheets of undifferentiated cells, indicative of a defect in proper differentiation. Furthermore, while the bulk of teratomas from each genotype was negative for Oct4 staining, indicating successful exit from pluripotency, small foci of Oct4 expression were retained in all cases (Figure 2.2F). Consistent with the *in vitro* differentiation data, teratomas derived from DKO ESCs contained significantly more undifferentiated, Oct4-positive nuclei than those from the other 3 lines. Taken together, our results indicate that while ESC differentiation *in vitro* and *in vivo* is delayed in the absence of BAX/BAK or CASP3, the impediment is more pronounced when BAX and BAK, the gatekeepers to the mitochondrial apoptotic pathway, are deleted. Interestingly,

these results mirror the greater degree of protection against apoptosis seen in *Bax*$^{-/-}$*Bak*$^{-/-}$ cells compared to *Casp3*$^{-/-}$ cells [20].

A previous study reported that CASP3 is activated during ESC differentiation but has a nonapoptotic role in promoting differentiation [12]. To test this result, we stained RA-treated ESCs cells with AnnexinV and propidium iodide (PI) during the course of differentiation and quantified apoptosis. Using this method, we found that the percentage of apoptotic cells is extremely low (~3%) in untreated, undifferentiated ESCs (Figure 2.3A). In contrast, approximately 10-12% of the ESC population actively undergoes apoptosis at 2 and 4 days after beginning RA-induced differentiation, while levels of apoptosis return to their pre-differentiation baseline by day 8 of RA treatment. In contrast, *Casp3*$^{-/-}$ and DKO ESCs lack evidence of apoptosis under both untreated and RA treated conditions (Figure 2.3A). Consistent with the above data, CASP3 is only cleaved and activated after RA treatment in WT and *Bax*$^{f/f}$ *Bak*$^{-/-}$ ESCs (Figure 2.3B). This absence of cleaved CASP3 and apoptosis in RA-treated DKO ESCs demonstrates that BAX and BAK are required for differentiation-induced apoptosis.

We next sought to determine the upstream factors responsible for activation of BAX/BAK during ESC differentiation. Based on a small microarray analysis of approximately 100 genes involved in cell death and survival, we found that mRNA expression of the death receptor FAS was upregulated >30 fold after 4 days of RA treatment; its cognate ligand FAS ligand (FAS-L) was upregulated >3 fold as well (data not shown). We confirmed that during differentiation, both FAS and FAS-L are markedly upregulated at the mRNA level (Figures 2.4A) and protein level (Figure 2.4C). A member of the tumor necrosis factor superfamily and a prototypical death receptor, FAS

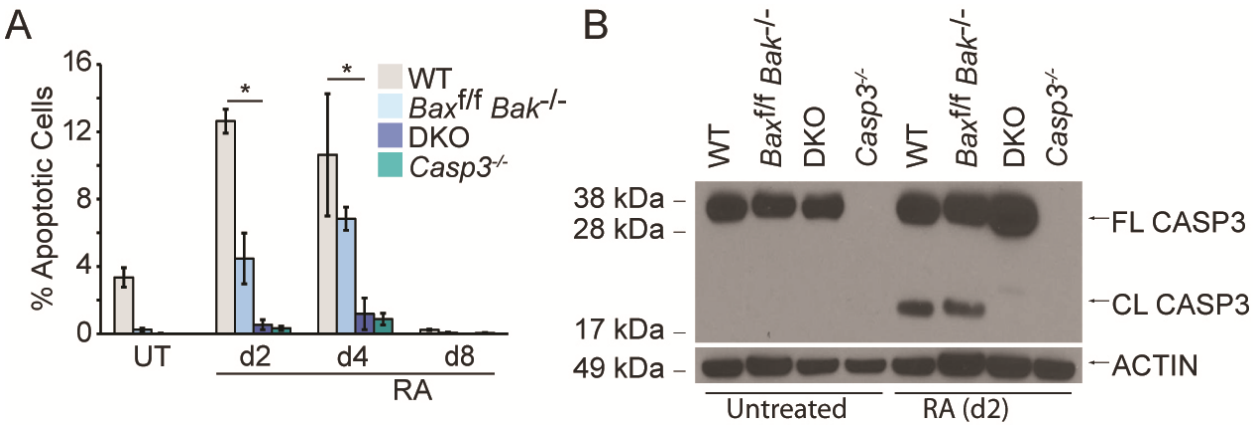

Figure 2.3. ESCs undergo BAX/BAK-dependent apoptosis during differentiation. (A) Quantification of percent apoptotic cells (AnnexinV positive/PI negative) during RA-mediated differentiation. (B) Immunoblot for full-length (FL) and cleaved (CL) CASP3 from ESCs untreated or treated with RA for two days.

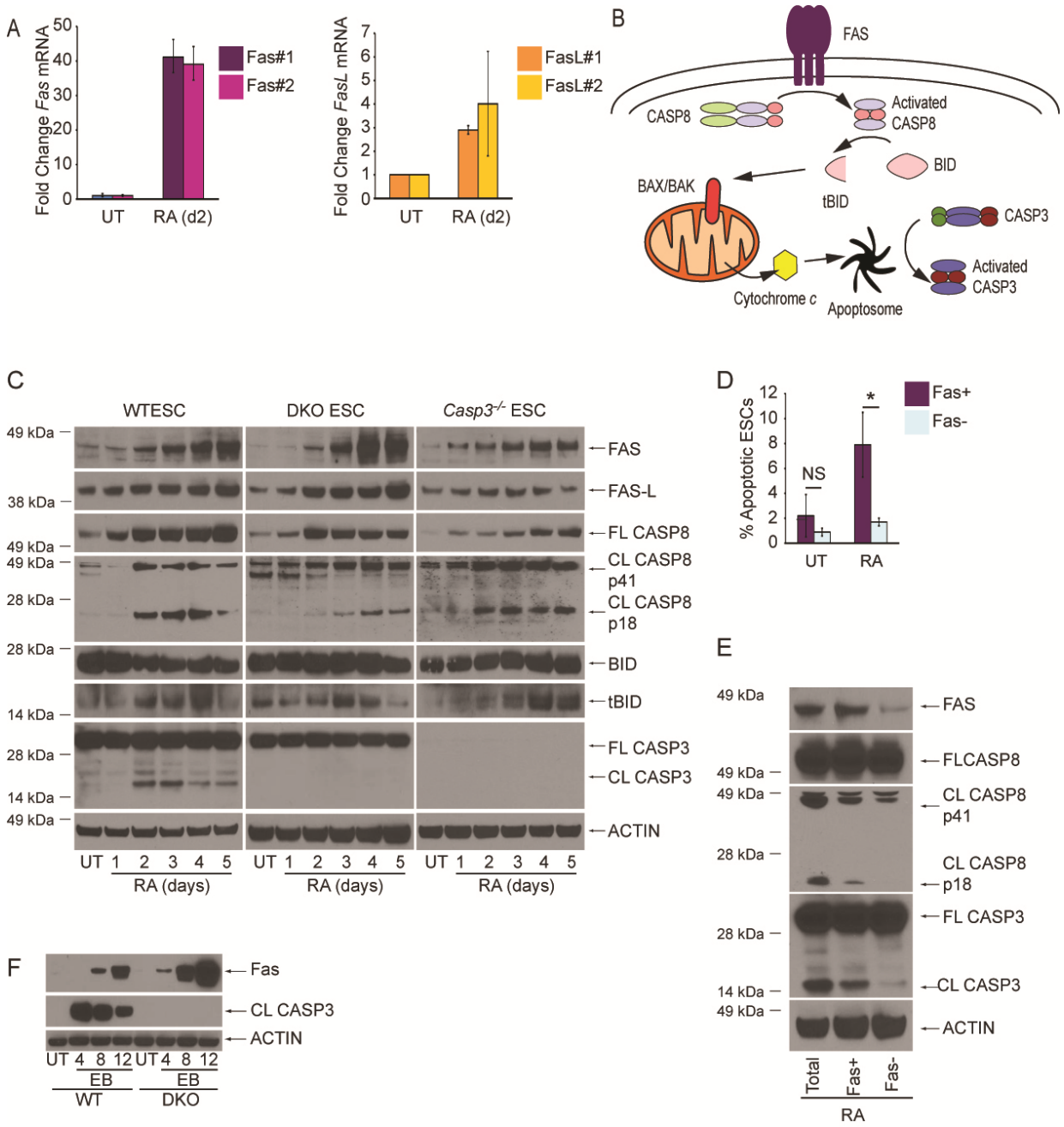

Figure 2.4. FAS is a major trigger of BAX/BAK-dependent apoptosis during differentiation.

(A) Representative Q-PCR of *Fas* and *FasL* mRNA levels during ESC differentiation. (B) Schematic of FAS-mediated activation of BAX/BAK-dependent apoptosis. (C) Immunoblot for components of the Type II FAS death receptor pathway during ESC differentiation. (D) FAS and AnnexinV co-staining in ESCs after two days of differentiation. (E) Immunoblot for CASP8 and CASP3 in ESCs sorted for FAS after two days of differentiation. (F) Immunoblots for FAS and CASP3 from WT or DKO cells induced to form embryoid bodies by the hanging drop method. Three independent biological samples were used for the AnnexinV assays. Data plotted as mean ± SD. * significant at $p < 0.05$ (Student t test).

can trigger apoptosis when bound by FAS-L through assembly of a multi-protein death-inducing signaling complex (DISC) and subsequent activation of Caspase-8 (CASP8) [21]. In some cells (Type I), FAS-mediated activation of CASP8 is sufficient to activate executioner CASP3; however, in other cells (Type II), FAS-mediated apoptosis requires amplification through CASP8-dependent activation of the BH3-only protein BID and subsequent engagement of BAX and BAK [21] (Figure 2.4B). As BAX and BAK are required for apoptosis during ESC differentiation, we next determined whether the Type II FAS pathway is engaged during this process.

First, we analyzed CASP8 and found that it was both upregulated and cleaved to form the active p18 fragment during ESC differentiation (Figure 2.4C). We also observed cleavage of BID during differentiation (Figure 2.4C). Importantly, cleavage of both CASP8 and BID occurred upstream of BAX/BAK and in the absence of CASP3, suggesting that these events occur due to engagement of an upstream death receptor rather than feedback loops from activated downstream caspases. We then costained differentiating ESCs for FAS and AnnexinV and found a significant enrichment of apoptotic cells in the FAS-positive subpopulation (Figure 2.4D). Consistent with this result, when we sorted differentiating WT ESCs for FAS, we found that both CASP8 and CASP3 activation were largely restricted to the FAS positive population (Figure 2.4E). We also observed a similar phenotype during EB formation, as FAS is strongly upregulated in both WT and DKO ESCs, while cleaved CASP3 is only detected in WT ESCs (Figure 2F).

To determine whether differentiated or undifferentiated ESCs are more susceptible to apoptosis, we utilized an Oct4-GFP ESC reporter line [22] to measure

levels of AnnexinV staining after RA treatment. Strikingly, we found that apoptosis is significantly enriched in the undifferentiated (GFP^{high}) population (Figure 2.5A). We then sorted these reporter cells for GFP expression and immunoblotted lysates from undifferentiated (GFP^{high}) and differentiated (GFP^{low}) populations for CASP3. Consistent with the previous result, we found elevated activation of CASP3 in undifferentiated (GFP^{high}/$Oct4^{high}$) cells (Figure 2.5B). Thus, a subgroup of poorly differentiating ESCs preferentially initiates apoptosis through the BAX/BAK pathway.

As we had previously found FAS to be highly upregulated during ESC differentiation (Figure 2.4A,C,F), we next determined its distribution among ESCs during differentiation. We again used the Oct4-GFP ESC reporter system and found that FAS-expressing cells are predominantly undifferentiated (GFP-positive/$Oct4^{high}$) (Figure 2.5C), consistent with the enrichment of apoptotic cells in this poorly differentiating subpopulation (Figure 2.5A). Accordingly, after sorting differentiating WT ESCs for FAS expression, we find that FAS^{high} cells have markedly higher levels of OCT4 than FAS^{low} cells (Figure 2.5D).

To determine the cellular source of FAS-L, we sorted Oct4-GFP ESCs for GFP expression, isolated mRNA, and measured *FasL* expression by real-time PCR. Interestingly, we found that *FasL* mRNA is upregulated in both undifferentiated and differentiated subpopulations (Figure 2.5E), suggesting that poorly differentiated cells acquire this death signal through both autocrine and paracrine sources.

To formally test the roles of FAS and CASP8 in ESC differentiation, we performed siRNA knockdowns (Figure 2.6A). In comparison to cells transfected with a nontargeting control siRNA, the levels of apoptotic cells were significantly reduced after

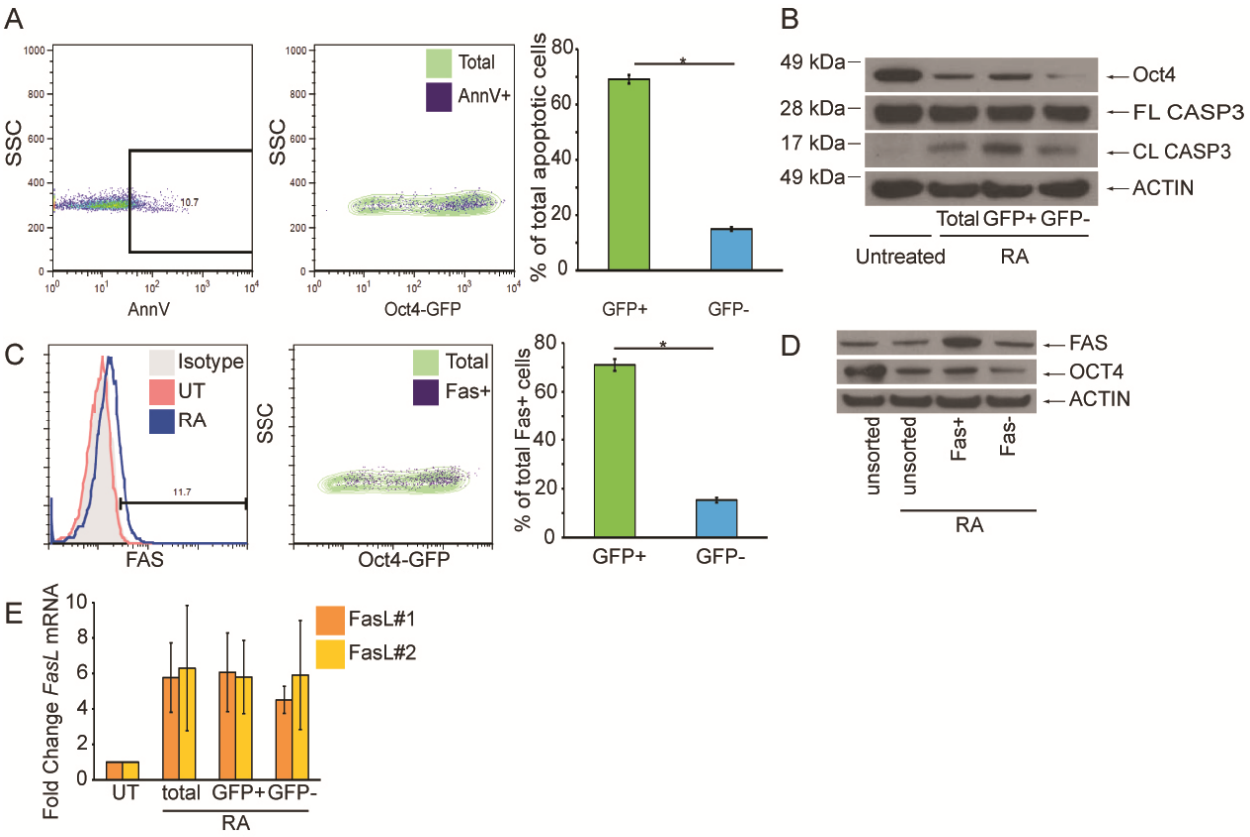

Figure 2.5. FAS is associated with apoptotic cells during ESC differentiation.
(A) Representative FACS plots and quantification of Oct4-GFP ESCs stained for AnnexinV after two days of RA treatment. (B) Immunoblots of lysates from 2-day treated Oct4-GFP ESCs after sorting for GFP expression. (C) Representative FACS plots and quantification of Oct4-GFP ESCs stained for FAS after two days of RA treatment. (D) Immunoblot for Oct4 from 2-day treated WT ESCs after sorting for FAS expression. (E) Q-PCR for *FasL* mRNA from Oct4-GFP ESCs treated or untreated with RA for two days.

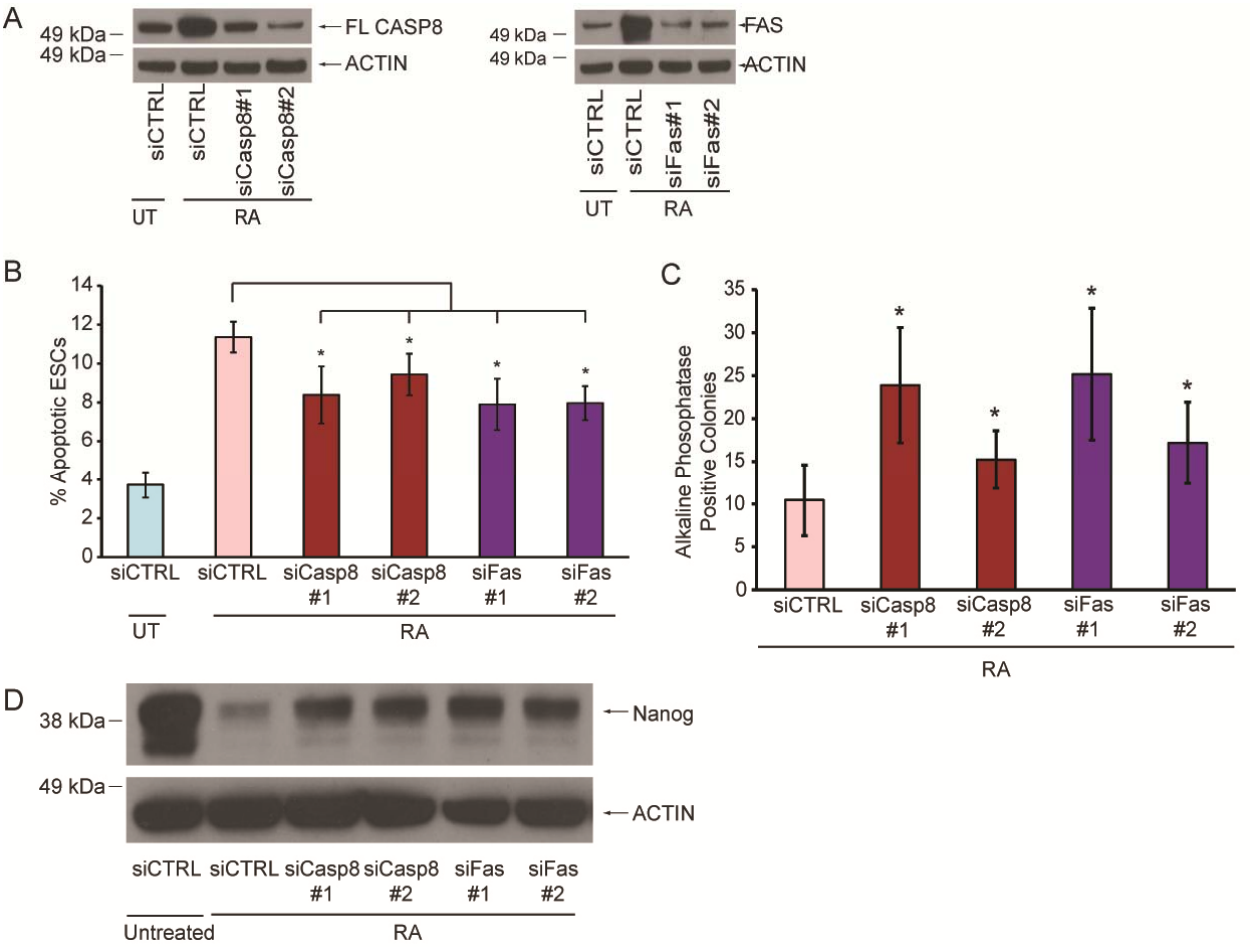

Figure 2.6. FAS and CASP8 promote the removal of poorly differentiating cells during ESC differentiation.

(A) Immunoblot of ESC lysates for CASP8 and FAS after siRNA knockdown and 2 days RA treatment. (B) AnnexinV staining of ESCs quantified by FACS after indicated siRNA knockdown and 2 days RA treatment. (C) Number of AP+ colonies after indicated siRNA knockdown and 2 days RA treatment. (D) Immunoblot of ESC lysates for Nanog after siRNA knockdown and 2 days RA treatment. Three independent biological samples were used for the AnnexinV, qPCR, and AP assays. Data plotted as mean ± SD. * significant at $p < 0.05$ (Student t test).

knockdown of FAS or CASP8 (Figure 2.6B), demonstrating a vital role for both proteins in triggering apoptosis. Furthermore, siRNA knockdown of either FAS or CASP8 resulted in a significantly increased number of AP-positive colonies after RA treatment and delayed the loss of Nanog (Figures 2.6C,D). Taken together, our data strongly suggest that engagement of FAS is a critical upstream activator of the intrinsic apoptotic pathway during ESC differentiation.

We next tested known transcriptional regulators of *Fas* to determine the factor responsible for its upregulation, and discovered that control of *Fas* mRNA and protein is largely dependent on p53 (Figure 2.7A-C). Interestingly, others have reported a nonapoptotic role for p53 in ESC differentiation [23]. To carefully examine the role of p53 in differentiation-induced apoptosis in ESCs, we examined both AnnexinV staining and CASP3 activation. Consistent with the inability of $p53^{-/-}$ ESCs to efficiently upregulate FAS, these cells were protected against apoptosis and CASP3 cleavage (Figure 2.7D,E).

In examining the role of p53 during differentiation, we found that, counterintuitively, p53 mRNA and protein levels actually decline during WT ESC differentiation (Figure 2.7F,G), a result consistent with several previous reports [23-25]. To mechanistically explain how p53 activity could increase despite a decrease in its levels, we reasoned that p53 activity may be restrained in undifferentiated ESCs, and this signaling brake could be lifted during differentiation. Indeed, a previous study demonstrated that Aurora Kinase A (AurA), a kinase that plays important roles during mitosis, phosphorylates p53 in undifferentiated ESCs to inhibit its transcriptional activity

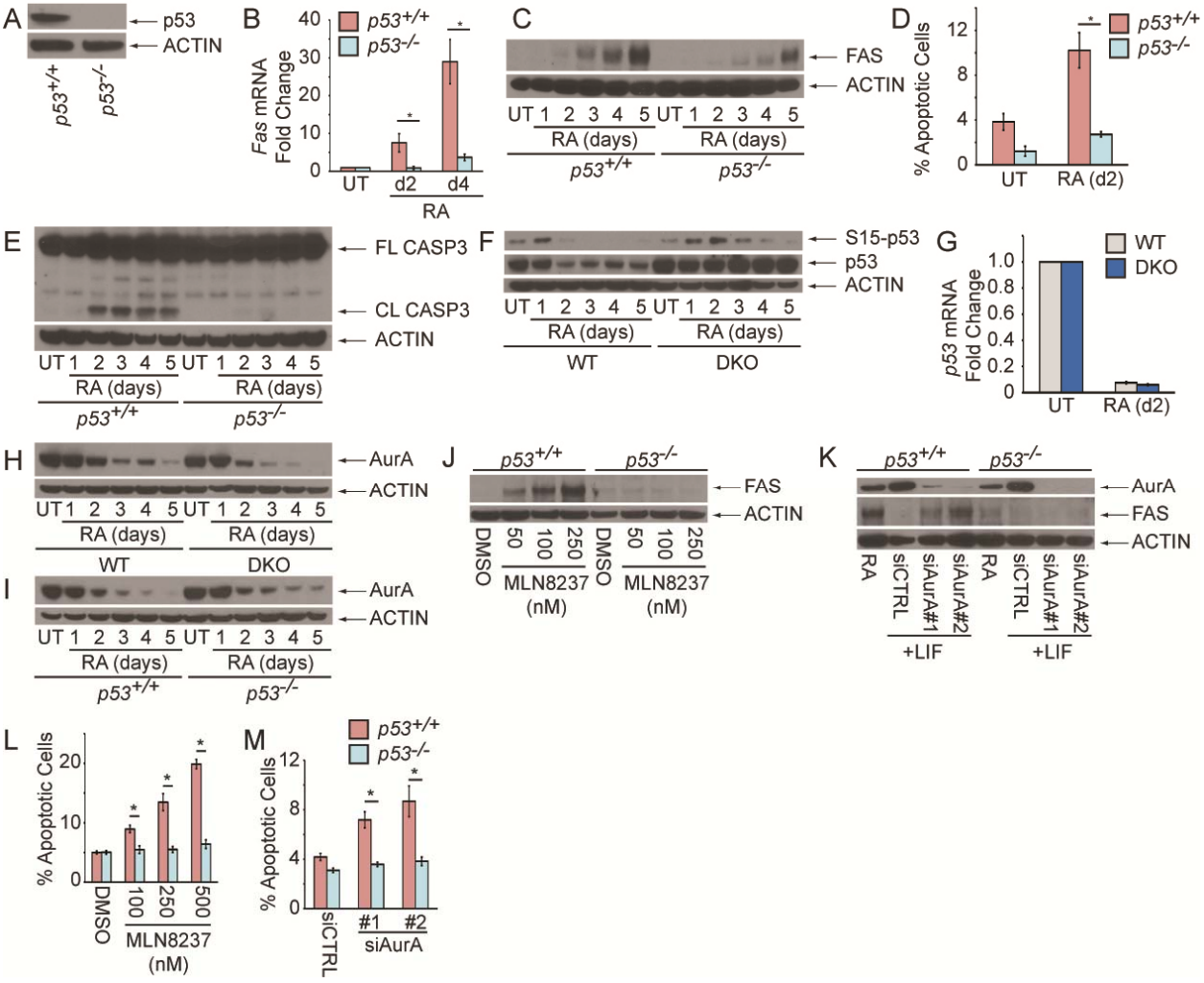

Figure 2.7. Upregulation of FAS and activation of apoptosis during ESC differentiation is dependent on p53.

(A) Immunoblot of p53 from *p53*$^{+/+}$ and *p53*$^{-/-}$ ESCs. (B) mRNA and (C) protein levels of *Fas* from RA-treated *p53*$^{+/+}$ and *p53*$^{-/-}$ ESCs. (D) AnnexinV staining of *p53*$^{+/+}$ and *p53*$^{-/-}$ ESCs after 2 days RA treatment. (E) Immunoblot of CASP3 from *p53*$^{+/+}$ and *p53*$^{-/-}$ ESCs treated with RA. (F) Immunoblot for p53 from WT and DKO ESCs during RA treatment. (G) mRNA levels of *p53* from WT and DKO ESCs during RA treatment. Immunoblot for AurA from (H) WT and DKO or (I) *p53*$^{+/+}$ and *p53*$^{-/-}$ ESCs during RA treatment. (J) Immunoblot for FAS from *p53*$^{+/+}$ and *p53*$^{-/-}$ ESCs treated with MLN8237 for 24 hr. (K) Immunoblot for FAS from *p53*$^{+/+}$ and *p53*$^{-/-}$ ESCs transfected with control siRNA or siRNA against AurA. AnnexinV staining of p53+/+ and p53-/- ESCs after treatment with (L) MLN8237 for 24 hr or (M) knockdown with control or AurA-specific siRNA. Three independent biological samples were used for the AnnexinV and qPCR assays. Data plotted as mean ± SD. * significant at $p < 0.05$ (Student t test).

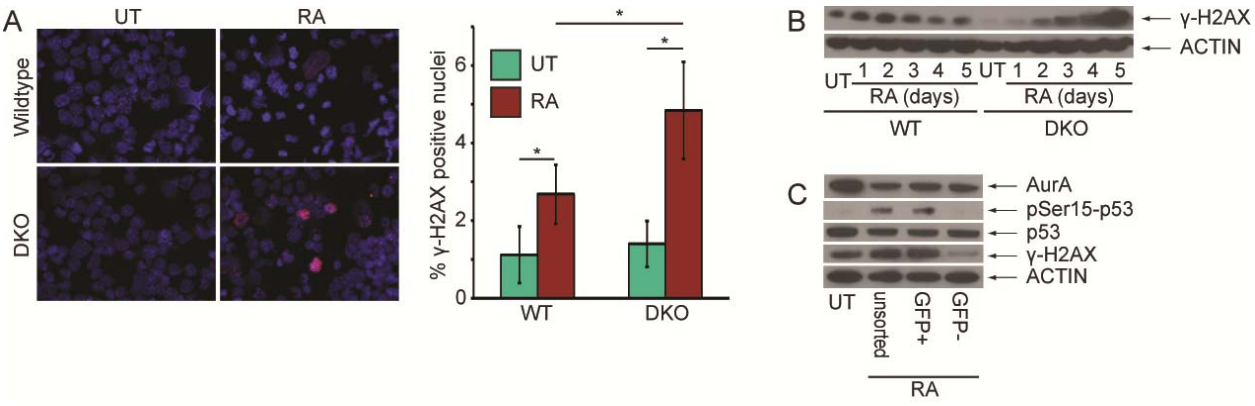

Figure 2.8. Markers of DNA damage are elevated during ESC differentiation.
(A) Immunblot for γ-H2AX from WT and DKO ESCs treated with RA. (B) Immunblot for AurA, p53, and γ-H2AX from Oct4-GFP ESCs sorted for GFP expression after 2 day RA treatment. (C) Representative immunofluorescence images and quantification of γ-H2AX+ nuclei from WT and DKO ESCs untreated or treated with RA for 4 days.

[24]. As such, we probed for AurA during ESC differentiation and found that its levels are significantly reduced, irrespective of *Bax/Bak* or *p53* status (Figure 2.7H,I).

If AurA is an inhibitor of p53, then decreasing its activity using small molecule kinase inhibitors or siRNA knockdown should allow p53 to upregulate *Fas* and to trigger apoptosis. Indeed, treatment of undifferentiated ESCs with the AurA-specific kinase inhibitor MLN8237 or siRNA knockdown of AurA was sufficient to induce upregulation of FAS (Figure 2.7J,K) and to trigger apoptosis (Figure 2.7L,M), both of which occurred in a p53-dependent manner. Thus, AurA restrains p53 function in undifferentiated ESCs, and its downregulation during differentiation allows p53-mediated upregulation of *Fas*.

As one of the canonical roles of p53 is to regulate the cellular response to DNA damage, we next tested ESCs for the presence of DNA damage markers. Interestingly, levels of phosphorylated histone protein H2AX (γ-H2AX), a classical marker of DNA damage, rise and fall during differentiation in WT ESCs but instead steadily accumulate in DKO ESCs (Figure 2.8B), suggesting that cells with pre-existing and/or differentiation-induced DNA damage are efficiently removed in WT ESC populations but not in apoptosis-deficient DKO ESC populations. We confirmed this finding by using immunofluorescence to look for the presence of γ-H2AX foci during differentiation, and found that while both DKO ESCs retained cells with intense γ-H2AX staining after 4 days of RA treatment (Figure 2.8A). Interestingly, p53 protein levels do not significantly decline in DKO ESCs during differentiation (Figure 2.7F), suggesting that the inability of DKO ESCs to remove damaged ESCs precludes the downregulation of p53 protein at the population level.

We next used Oct4-GFP reporter ESCs to investigate why Fas upregulation and

apoptosis primarily occur in poorly differentiating ESCs. Although we observed no significant difference in AurA or total p53 levels between GFP^{high} and GFP^{low} cells, we found increased levels of γ-H2AX and phospho-Ser15-p53 in undifferentiated ESCs (Figure 2.8C). As phosphorylation on Ser15 of p53 is a well-established activating modification, our data suggest that p53 activity is elevated in the poorly differentiated subpopulation.

Our data indicate that while AurA normally restrains p53 function in undifferentiated ESCs, its levels precipitously drop during differentiation to license p53 activity. Taken together, our data demonstrate that downregulation of AurA during ESC differentiation unleashes p53 to initiate FAS- and BAX/BAK-dependent apoptosis in poorly differentiating ESCs (Figure 2.9).

DISCUSSION

The removal of supernumerary or damaged cells by programmed cell death is crucial for organogenesis of all multicellular organisms [26]. While instances of apoptosis are well documented during the later stages of embryogenesis through the postnatal period, its role in ESC differentiation is not yet fully defined.

Here, we provide evidence that a substantial fraction of ESCs exposed to differentiation conditions activates CASP3 and undergoes BAX/BAK-dependent apoptosis. Moreover, we discovered that upregulation and engagement of the death receptor FAS on the surface of undifferentiated ESCs is a major trigger of the BAX/BAK pathway, restricting apoptosis largely to these poorly differentiating cells. As *Bax*$^{-/-}$*Bak*$^{-/-}$ ESCs exhibit a significant delay in differentiation both in culture and during teratoma

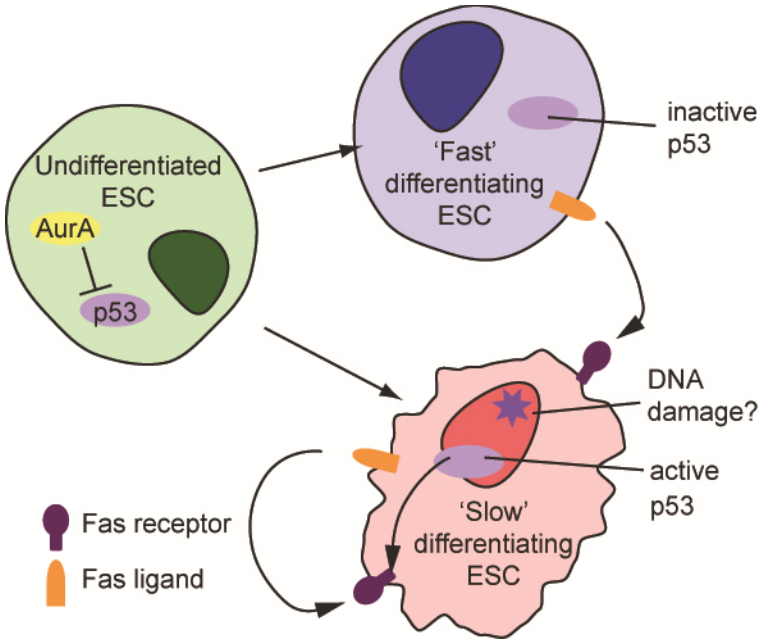

Figure 2.9. Schematic of FAS-L-mediated activation of FAS to induce apoptosis in undifferentiated ESCs.

formation, the most parsimonious explanation for the observed phenotype is their failure to selectively remove undifferentiated cells from the larger population.

The differentiation defect of *Bax*$^{-/-}$*Bak*$^{-/-}$ ESCs is consistent with a previous report that deletion of *Casp3* causes a delay in ESC differentiation [12] as well as the observed late embryonic lethal phenotype of *Casp3*$^{-/-}$ and *Bax*$^{-/-}$*Bak*$^{-/-}$ mice [3, 11], which demonstrates that cells lacking these pro-apoptotic genes can ultimately differentiate *in vivo*, certainly past the ESC stage. However, our results support a pro-apoptotic role for CASP3 in contrast to this previous study's report that CASP3 is activated to cleave the pluripotency factor Nanog rather than promote apoptosis [12]; the inability to find evidence of apoptosis during RA-induced ESC differentiation in this prior study may be due to a reliance on DAPI staining to identify apoptotic bodies rather than the more sensitive and specific markers employed here. Although our data strongly argue that the predominant role of CASP3 during differentiation is to promote apoptosis and thereby cull undifferentiated cells, it does not rule out the possibility that CASP3 may have additional non-apoptotic functions in enhancing differentiation.

While our studies on apoptosis have largely utilized cultured ESCs, cell death has been observed in the developing embryo at the blastocyst stage in a wide range of species, including mice and humans [27-30]. Reports have estimated that roughly 10-20% murine inner cell mass (ICM) cells, the source of ESCs, undergo apoptosis, and this may function to eliminate cells that fail to differentiate [27, 28]. Interestingly, there have also been several studies reporting upregulation of FAS and FAS-L in rodent and human blastocysts during early embryogenesis [31, 32]. While these findings are consistent with our results, careful studies regarding the roles of FAS and BAX/BAK in

regulating apoptosis in the ICM remain to be done.

Our findings also suggest an expanded role for p53 in ESCs. While p53 has been shown to promote murine ESC differentiation by transcriptionally repressing *Nanog* [23], it also plays an important role in the cellular response to DNA damage. Interestingly, while several groups have reported that murine and human ESCs are especially sensitive to DNA damage [33, 34], others have found that p53 accumulates in ESCs without activating transcription of its target genes [24, 35]. Consistent with the latter reports, we find that AurA restrains p53 activity in undifferentiated ESCs, and discovered a novel function for p53 in removing damaged cells during the differentiation process via mitochondrial apoptosis to promote efficiency and fidelity of ESC differentiation.

Furthermore, we uncovered a novel association between AurA and apoptosis in ESCs. As the primary pluripotency factors Oct4, Nanog, and KLF4 do not seem to be responsible for regulating AurA levels in ESCs (Figure 2.10), the mechanisms that control its expression remain to be defined. However, AurA clearly serves as a major restraint on p53-induced apoptosis since inhibiting it through pharmacologic or genetic maneuvers is sufficient to induce p53-dependent upregulation of FAS and apoptosis. This link immediately suggests AurA as a potential therapeutic target for malignant teratomas in humans, as these cells may be especially susceptible to inhibition of AurA. More generally, upregulation or hyperactivation of AurA may be a mechanism utilized by cancer cells to inhibit p53 signaling without mutating p53 itself. Thus, inhibition of AurA may “re-awaken” endogenous p53 in these tumors to promote apoptosis.

Finally, the striking accumulation of γ-H2AX in DKO ESCs coupled with the

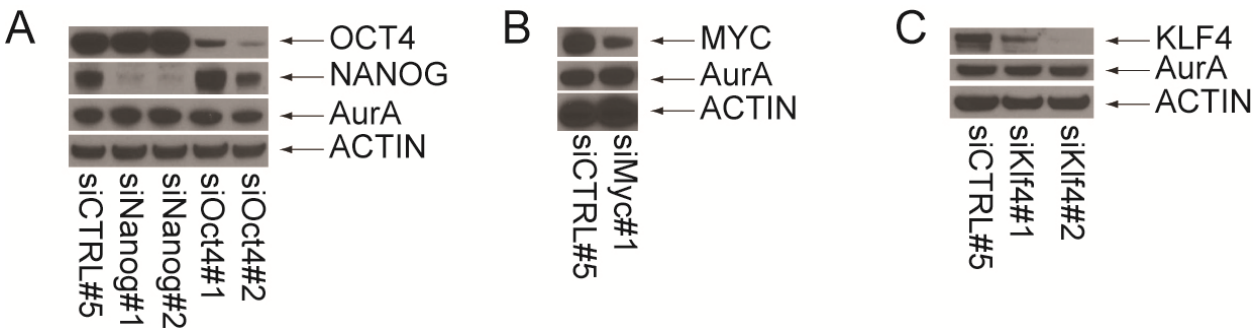

Figure 2.10. Core pluripotency factors do not transcriptionally regulate expression of Aurora Kinase A

Immunoblot for AurA after siRNA knockdowns of (A) Oct4 and Nanog, (B) c-Myc, and (C) KLF4.

efficient loss of this damage marker in WT ESCs during differentiation suggests that DNA damage may be a crucial trigger to fully activate p53. However, careful future studies are necessary to determine which upstream sensor of DNA damage is activated. In addition, crucial questions, such as whether a subpopulation of ESCs in the undifferentiated state has already accumulated DNA damage and is not efficiently removed due to AurA-mediated repression of p53 or whether the inability to differentiate can itself cause DNA damage response, remain to be addressed.

In summary, our findings show that the mitochondrial apoptotic pathway plays a critical role in ESC differentiation and that apoptotic signaling is necessary for the efficient removal of damaged and poorly differentiated cells. These results highlight the heterogeneity of isogenic ESCs and reveal a novel role for apoptosis in controlling cell fate decisions during ESC differentiation.

REFERENCES

1. Tait, S.W., and Green, D.R. (2010). Mitochondria and cell death: outer membrane permeabilization and beyond. Nature reviews. Molecular cell biology *11*, 621-632.
2. Wei, M.C., Zong, W.X., Cheng, E.H., Lindsten, T., Panoutsakopoulou, V., Ross, A.J., Roth, K.A., MacGregor, G.R., Thompson, C.B., and Korsmeyer, S.J. (2001). Proapoptotic BAX and BAK: a requisite gateway to mitochondrial dysfunction and death. Science *292*, 727-730.
3. Lindsten, T., Ross, A.J., King, A., Zong, W.X., Rathmell, J.C., Shiels, H.A., Ulrich, E., Waymire, K.G., Mahar, P., Frauwirth, K., et al. (2000). The combined functions of proapoptotic Bcl-2 family members bak and bax are essential for normal development of multiple tissues. Molecular cell *6*, 1389-1399.
4. Shamas-Din, A., Brahmbhatt, H., Leber, B., and Andrews, D.W. (2011). BH3-only proteins: Orchestrators of apoptosis. Biochimica et biophysica acta *1813*, 508-520.
5. Jiang, X., and Wang, X. (2004). Cytochrome C-mediated apoptosis. Annual review of biochemistry *73*, 87-106.
6. Parrish, A.B., Freel, C.D., and Kornbluth, S. (2013). Cellular mechanisms controlling caspase activation and function. Cold Spring Harbor perspectives in biology *5*.
7. Knudson, C.M., Tung, K.S., Tourtellotte, W.G., Brown, G.A., and Korsmeyer, S.J. (1995). Bax-deficient mice with lymphoid hyperplasia and male germ cell death. Science *270*, 96-99.

8. De Maria, R., Testa, U., Luchetti, L., Zeuner, A., Stassi, G., Pelosi, E., Riccioni, R., Felli, N., Samoggia, P., and Peschle, C. (1999). Apoptotic role of Fas/Fas ligand system in the regulation of erythropoiesis. Blood *93*, 796-803.

9. Honarpour, N., Du, C., Richardson, J.A., Hammer, R.E., Wang, X., and Herz, J. (2000). Adult Apaf-1-deficient mice exhibit male infertility. Developmental biology *218*, 248-258.

10. Kuida, K., Haydar, T.F., Kuan, C.Y., Gu, Y., Taya, C., Karasuyama, H., Su, M.S., Rakic, P., and Flavell, R.A. (1998). Reduced apoptosis and cytochrome c-mediated caspase activation in mice lacking caspase 9. Cell *94*, 325-337.

11. Kuida, K., Zheng, T.S., Na, S., Kuan, C., Yang, D., Karasuyama, H., Rakic, P., and Flavell, R.A. (1996). Decreased apoptosis in the brain and premature lethality in CPP32-deficient mice. Nature *384*, 368-372.

12. Fujita, J., Crane, A.M., Souza, M.K., Dejosez, M., Kyba, M., Flavell, R.A., Thomson, J.A., and Zwaka, T.P. (2008). Caspase activity mediates the differentiation of embryonic stem cells. Cell stem cell *2*, 595-601.

13. Duval, D., Malaise, M., Reinhardt, B., Kedinger, C., and Boeuf, H. (2004). A p38 inhibitor allows to dissociate differentiation and apoptotic processes triggered upon LIF withdrawal in mouse embryonic stem cells. Cell death and differentiation *11*, 331-341.

14. Akbari-Birgani, S., Hosseinkhani, S., Mollamohamadi, S., and Baharvand, H. (2014). Delay in Apoptosome Formation Attenuates Apoptosis in mouse Embryonic Stem Cell Differentiation. The Journal of biological chemistry.

15. Takeuchi, O., Fisher, J., Suh, H., Harada, H., Malynn, B.A., and Korsmeyer, S.J.

(2005). Essential role of BAX,BAK in B cell homeostasis and prevention of autoimmune disease. Proceedings of the National Academy of Sciences of the United States of America *102*, 11272-11277.

16. Jakel, H.P., Wobus, A.M., Bloch, C., Jakel, N., and Schoneich, J. (1983). A micromethod for the determination of alkaline phosphatase in mammalian cells. Biomedica biochimica acta *42*, 1123-1128.

17. Loh, Y.H., Wu, Q., Chew, J.L., Vega, V.B., Zhang, W., Chen, X., Bourque, G., George, J., Leong, B., Liu, J., et al. (2006). The Oct4 and Nanog transcription network regulates pluripotency in mouse embryonic stem cells. Nature genetics *38*, 431-440.

18. Chambers, I., Colby, D., Robertson, M., Nichols, J., Lee, S., Tweedie, S., and Smith, A. (2003). Functional expression cloning of Nanog, a pluripotency sustaining factor in embryonic stem cells. Cell *113*, 643-655.

19. Mitsui, K., Tokuzawa, Y., Itoh, H., Segawa, K., Murakami, M., Takahashi, K., Maruyama, M., Maeda, M., and Yamanaka, S. (2003). The homeoprotein Nanog is required for maintenance of pluripotency in mouse epiblast and ES cells. Cell *113*, 631-642.

20. Cheng, E.H., Wei, M.C., Weiler, S., Flavell, R.A., Mak, T.W., Lindsten, T., and Korsmeyer, S.J. (2001). BCL-2, BCL-X(L) sequester BH3 domain-only molecules preventing BAX- and BAK-mediated mitochondrial apoptosis. Molecular cell *8*, 705-711.

21. Kaufmann, T., Strasser, A., and Jost, P.J. (2012). Fas death receptor signalling: roles of Bid and XIAP. Cell death and differentiation *19*, 42-50.

22. Ying, Q.L., Nichols, J., Evans, E.P., and Smith, A.G. (2002). Changing potency by spontaneous fusion. Nature *416*, 545-548.

23. Lin, T., Chao, C., Saito, S., Mazur, S.J., Murphy, M.E., Appella, E., and Xu, Y. (2005). p53 induces differentiation of mouse embryonic stem cells by suppressing Nanog expression. Nature cell biology *7*, 165-171.

24. Lee, D.F., Su, J., Ang, Y.S., Carvajal-Vergara, X., Mulero-Navarro, S., Pereira, C.F., Gingold, J., Wang, H.L., Zhao, R., Sevilla, A., et al. (2012). Regulation of embryonic and induced pluripotency by aurora kinase-p53 signaling. Cell stem cell *11*, 179-194.

25. Lutzker, S.G., and Levine, A.J. (1996). A functionally inactive p53 protein in teratocarcinoma cells is activated by either DNA damage or cellular differentiation. Nature medicine *2*, 804-810.

26. Meier, P., Finch, A., and Evan, G. (2000). Apoptosis in development. Nature *407*, 796-801.

27. Pierce, G.B., Lewellyn, A.L., and Parchment, R.E. (1989). Mechanism of programmed cell death in the blastocyst. Proceedings of the National Academy of Sciences of the United States of America *86*, 3654-3658.

28. Hardy, K. (1997). Cell death in the mammalian blastocyst. Molecular human reproduction *3*, 919-925.

29. El-Shershaby, A.M., and Hinchliffe, J.R. (1974). Cell redundancy in the zona-intact preimplantation mouse blastocyst: a light and electron microscope study of dead cells and their fate. Journal of embryology and experimental morphology *31*, 643-654.

30. Hardy, K., Handyside, A.H., and Winston, R.M. (1989). The human blastocyst: cell number, death and allocation during late preimplantation development in vitro. Development *107*, 597-604.

31. Kelkar, R.L., Dharma, S.J., and Nandedkar, T.D. (2003). Expression of Fas and Fas ligand protein and mRNA in mouse oocytes and embryos. Reproduction *126*, 791-799.

32. Kawamura, K., Fukuda, J., Kodama, H., Kumagai, J., Kumagai, A., and Tanaka, T. (2001). Expression of Fas and Fas ligand mRNA in rat and human preimplantation embryos. Molecular human reproduction *7*, 431-436.

33. Dumitru, R., Gama, V., Fagan, B.M., Bower, J.J., Swahari, V., Pevny, L.H., and Deshmukh, M. (2012). Human embryonic stem cells have constitutively active Bax at the Golgi and are primed to undergo rapid apoptosis. Molecular cell *46*, 573-583.

34. Roos, W.P., Christmann, M., Fraser, S.T., and Kaina, B. (2007). Mouse embryonic stem cells are hypersensitive to apoptosis triggered by the DNA damage O(6)-methylguanine due to high E2F1 regulated mismatch repair. Cell death and differentiation *14*, 1422-1432.

35. Qin, H., Yu, T., Qing, T., Liu, Y., Zhao, Y., Cai, J., Li, J., Song, Z., Qu, X., Zhou, P., et al. (2007). Regulation of apoptosis and differentiation by p53 in human embryonic stem cells. The Journal of biological chemistry *282*, 5842-5852.

CHAPTER 3

Allosteric inhibition of the IRE1α RNase preserves cell viability and function during endoplasmic reticulum stress

SUMMARY

Depending on endoplasmic reticulum (ER) stress levels, the ER transmembrane multi-domain protein IRE1α promotes either adaptation or apoptosis. Unfolded ER proteins cause IRE1α lumenal domain homo-oligomerization, inducing *trans* auto-phosphorylation that further drives homo-oligomerization of its cytosolic kinase/ endoribonuclease (RNase) domains to activate mRNA splicing of adaptive XBP1 transcription factor. However, under high/chronic ER stress, IRE1α surpasses an oligomerization threshold that expands RNase substrate repertoire to many ER-localized mRNAs, leading to apoptosis. To modulate these effects, we developed ATP-competitive IRE1α *K*inase *I*nhibiting *R*Nase *A*ttenuators – KIRAs – that allosterically inhibit IRE1α's RNase by breaking oligomers. One optimized KIRA, KIRA6, inhibits IRE1α *in vivo* and promotes cell survival under ER stress. Intravitreally, KIRA6 preserves photoreceptor functional viability in rat models of ER stress-induced retinal degeneration. Systemically, KIRA6 preserves pancreatic β-cells, increases insulin, and reduces hyperglycemia in Akita diabetic mice. Thus, IRE1α powerfully controls cell fate, but can itself be controlled with small molecules to reduce cell degeneration.

INTRODUCTION

Secreted and transmembrane proteins fold and assemble in the endoplasmic reticulum (ER) through reactions catalyzed by ER-resident activities. When these reactions are saturated or corrupted, cells experience “ER stress,” and unfolded protein accumulation in the ER triggers intracellular signaling pathways termed the unfolded protein response (UPR). The UPR induces transcription of genes encoding ER chaperones, oxidoreductases, and ER-associated degradation (ERAD) components [1], while inhibiting translation [2]. These outputs are adaptive because they enhance ER protein-folding capacity, reduce secretory protein load, and promote degradation of ER unfolded proteins.

However, if ER stress remains irremediably high and adaptive outputs are overwhelmed, alternative “Terminal UPR” signals trigger apoptosis. While cell death under high ER stress may protect organisms from exposure to improperly folded secretory proteins, many human degenerative diseases, such as diabetes mellitus and retinopathies, may be caused by excessive ER stress-induced cell death [3]. Mechanistic understanding of critical Terminal UPR signaling events may lead to effective therapies for such conditions.

Unfolded ER proteins activate three ER transmembrane sensors, PERK, ATF6, and IRE1α, by changing their oligomerization state in the ER membrane [4]. IRE1α, the most ancient of these components, senses unfolded proteins either directly or indirectly through an ER lumenal domain that becomes oligomerized during stress [5, 6]. Subsequently, IRE1α’s bifunctional kinase/endoribonuclease (RNase) activities become juxtaposed on its cytosolic

face, allowing monomers to *trans*-autophosphorylate. Kinase autophosphorylation conformationally activates IRE1α's RNase to site-specifically cleave the XBP1 mRNA. Religation and translation of XBP1 mRNA in an alternate open reading frame produces the XBP1s transcription factor whose targets encode proteins that enhance ER protein folding and quality control [7-9]. Thus, IRE1α promotes adaptation via XBP1s.

However, under high ER stress, IRE1α's RNase relaxes its substrate specificity to endonucleolytically cleave many other mRNAs that localize to the ER membrane as their encoded proteins undergo co-translational translocation [10, 11]. IRE1 α's RNase also cleaves precursors of apoptosis-inhibitory microRNAs [12, 13].

Here we show that multiple Terminal UPR outputs, including cell proliferation blocks, sterile inflammation, and apoptosis result from kinase-driven increases in the oligomerization state of IRE1α's cytosolic domains that hyperactivate its RNase. These destructive events are prevented by breaking IRE1α oligomerization through rational mutations or somatic mutations found in the *Ire1α* gene of various human cancers. To test physiological effects of pharmacologically inhibiting IRE1α, we developed small molecule kinase inhibitors that prevent oligomerization and allosterically inhibit its RNase. One such IRE1α kinase inhibitor preserves viability and function in ER-stressed cells, pancreatic islet explants, and rodent models of ER stress-induced retinitis pigmentosa and diabetes.

RESULTS

IRE1α's kinase is a rheostat that employs self-association to control RNase activity

Previously, we proposed that IRE1α's kinase regulates catalytic activity of its adjoining RNase in a graduated manner to impact cell fate in mammals, yet the mechanistic basis for the rheostatic control remained unclear [10]. Here, we hypothesized that the degree of self-association of kinase/RNase subunits on the cytosolic face connects IRE1α phosphorylation status to RNase activation levels. Increasing phosphorylation of the IRE1α kinase may proportionally increase the oligomeric state of kinase/RNase subunits past a critical threshold, thereby driving RNase activity into a hyperactive state. Consequently, IRE1α RNase expands its specificity past its canonical XBP1 mRNA substrate, endonucleolytically cleaving many ER-localized mRNAs and pushing cells into apoptosis. In this view, IRE1α's lumenal domains are responsive to protein-folding conditions in the ER, but rheostatic control by the kinase over the RNase ultimately determines cell fate. If these predictions are correct, genetic and small molecule control over IRE1α kinase oligomerization should enable cell fate control, irrespective of upstream ER stress.

To begin testing this hypothesis, we employed IRE1α recombinant proteins and cell lines. Artificial ER stress agents are widely used to acutely activate the UPR, but saturating doses that have no natural pathophysiological correlate are often employed. To test cytoprotection later in the work, we established dose-response regimes using three ER stress agents that dose-

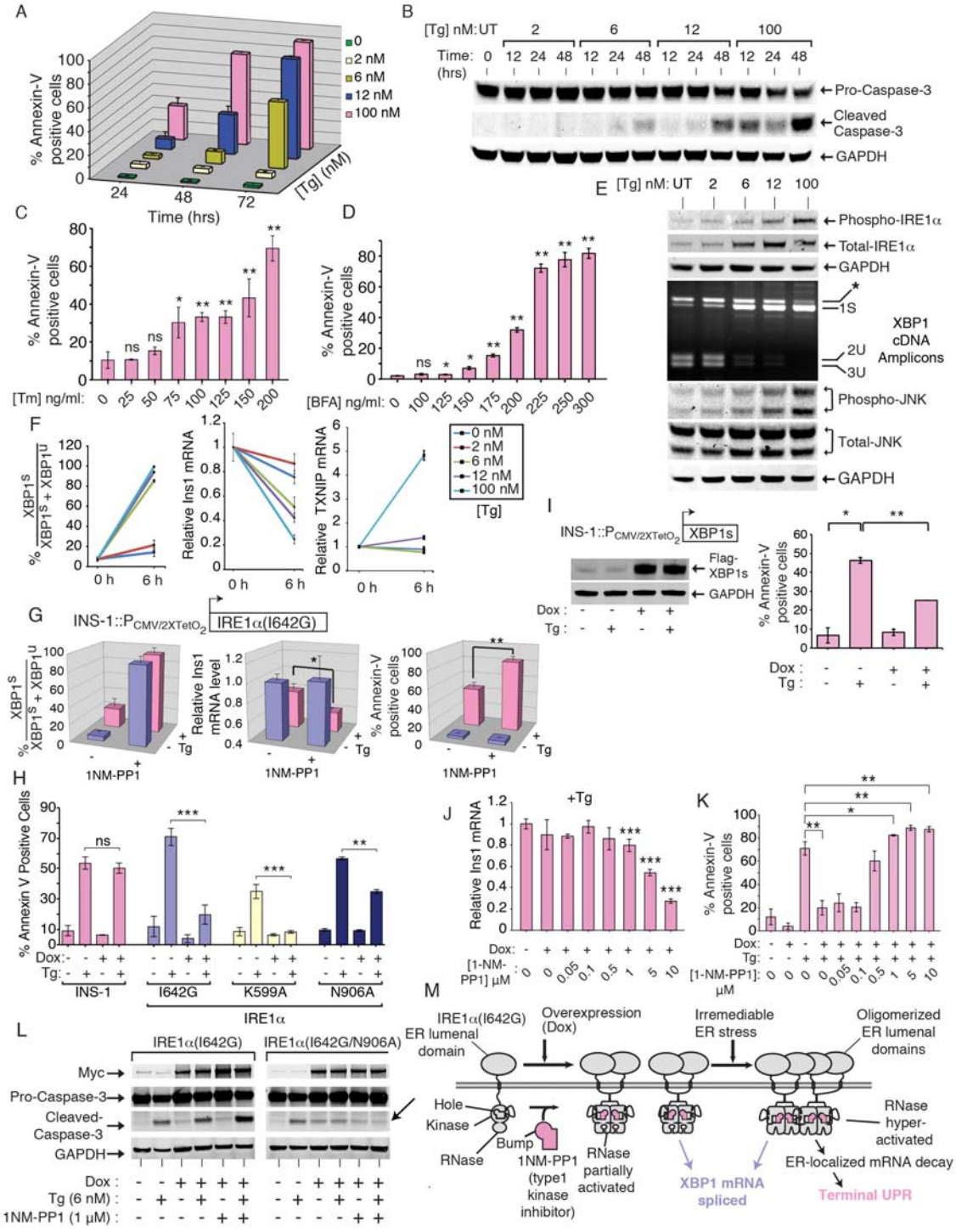

Figure 3.1. Irremediable ER stress activates IRE1α to induce a Terminal UPR and triggers apoptosis.

(A) Annexin-V staining of INS-1 cells exposed to increasing [Thapsigargin (Tg)] for up to 72hr. (B) Immunoblot of pro- and cleaved Caspase-3 from Tg-treated INS-1 cells. (C) Percent of INS-1 cells staining positive for Annexin V after

treatment with increasing concentrations of Tunicamycin (Tm) for 72hr. (D) Percent of INS-1 cells staining positive for Annexin V after treatment with increasing concentrations of Brefeldin A (BFA) for 72hr. Three independent biological samples were used. Data are plotted as means +/- SD. P-values: * <0.05, **<0.01. (E) Anti-phospho-IRE1α and anti-total IRE1α (upper), anti-phospho-JNK and anti-total JNK (lower) immunoblots of INS-1 cells treated for 12hr with increasing concentrations of Tg. GAPDH serves as a loading control. EtBr-stained agarose gel (middle) of XBP1 cDNA amplicons from INS-1 cells treated with increasing concentrations of Tg for 6hr. (F) Quantification of percent XBP1 splicing in same samples in (E). Real-Time PCR (Q-PCR) for Insulin1 and TXNIP mRNA (normalized to GAPDH) in INS-1 cells treated with increasing concentrations of Tg for 6hr. (G) Percent XBP1 splicing (24hr), relative Insulin1 (Ins1) mRNA levels by Q-PCR (24hr) and percent Annexin V staining (72hr) from 1 μg/ml doxycycline (Dox) treated INS-1 IRE1α (I642G) cells +/-1 μM 1NM-PP1 and +/-6 nM Tg. (H) Percent Annexin V staining (72 hr) of INS-1, INS-1 IRE1α (I642G), INS-1 IRE1α (K599A) and INS-1 IRE1α (N906A) cells exposed to +/- 1 μg/ml Dox and +/- 6 nM Tg. (I) Anti-Flag-XBP1s immunoblot (left panel) and percent Annexin V staining (right panel) of INS-1:: XBP1s (s=Spliced) cells exposed to +/- 1 μg/ml Dox for 24hr before exposure to +/- 6 nM Tg. (J) Q-PCR for Insulin1 mRNA (normalized to GAPDH) in 1 μg/ml Dox -induced INS-1 IRE1α (I642G) cells treated with Tg (6 nM) and increasing concentrations of 1NM-PP1 for 24hr. (K) Percentage of INS-1 IRE1α (I642G) cells staining positive for Annexin V after treatment for 72hr with Dox (1 μg/ml), Tg (6 nM) and increasing concentrations of 1NM-PP1. Three independent biological samples were used for each experiment and plotted as mean value +/- SD. P-values: *<0.05, ** <0.01 and *** <0.001, ns=not significant. (L) Immunoblot of Myc-IRE1α, Pro- and cleaved Caspase-3 from INS-1 IRE1α (I642G) and INS-1 IRE1α (I642G/N906A) cells treated for 72hr with combinations of Dox (1 μg/ml), 1NM-PP1 and Tg. (M) Model of intermediate oligomerization and activation of IRE1α (I642G) with 1NM-PP1, which is fully sufficient for XBP1 mRNA splicing without ER stress; higher-order oligomerization and extra-XBP1 endonucleolytic decay occurs under irremediable ER stress.

---

dependently push rat insulinoma (INS-1) cells, which have a well-developed ER and secrete insulin, past a stress threshold, and in switch-like manner, into apoptosis. The percentage of INS-1 cells entering apoptosis due to the ER Ca^{2+} pump inhibitor thapsigargin (Tg) depends aggregately on two variables: concentration and duration of exposure (Figure 3.1A,B). Similar results hold for the glycosylation inhibitor tunicamycin (Tm) and the anterograde trafficking inhibitor brefeldin A (BFA) (Figure 3.1C,D). Preceding apoptosis, increasing ER

stress agent levels progressively increases IRE1α phosphorylation, XBP1 mRNA splicing, endonucleolytic decay of the ER-localized mRNA, Ins1 mRNA (which encodes proinsulin), induction of thioredoxin-interacting protein (TXNIP) mRNA (whose product activates the NLRP3 inflammasome), and downstream c-Jun terminal kinase phosphorylation (JNKs) (Figure 3.1E,F).

All these signature events, culminating in apoptosis, can be simulated, without imposing ER stress, by conditionally over-expressing wild-type (WT) IRE1α in INS-1 stable lines [10]. Induced with doxycycline (Dox), the transgenic IRE1α (WT) proteins spontaneously self-associate, *trans*-autophosphorylate, and trigger XBP1 mRNA splicing (Figure 3.2A,B) [10]. Increasing [Dox] causes progressive decay of Ins1 mRNA, elevation of TXNIP mRNA, and apoptosis (Figure 3.2C,D). Thus, as with ER stress agents, dose escalation of the IRE1α (WT) transgene allows graduated control over the Terminal UPR and is sufficient to push cells, in switch-like manner, into apoptosis (Figure 3.2E).

To study how IRE1α autophosphorylation impacts oligomeric state and RNase substrate selectivity, we expressed and purified a recombinant soluble mini-protein containing the kinase/RNase domains—called IRE1α*. Salt bridges formed through phospho-amino groups in neighboring IRE1α kinases contribute to kinase/RNase homo-oligomerization [14, 15]. IRE1α* is basally autophosphorylated and spontaneously homo-oligomerizes as its concentration is raised (Figure 3.2F,G). Dephosphorylation of IRE1α* with λ-phosphatase—(dP-IRE1α*)—reduces the oligomer/monomer ratio, confirming that phosphorylation drives oligomerization.

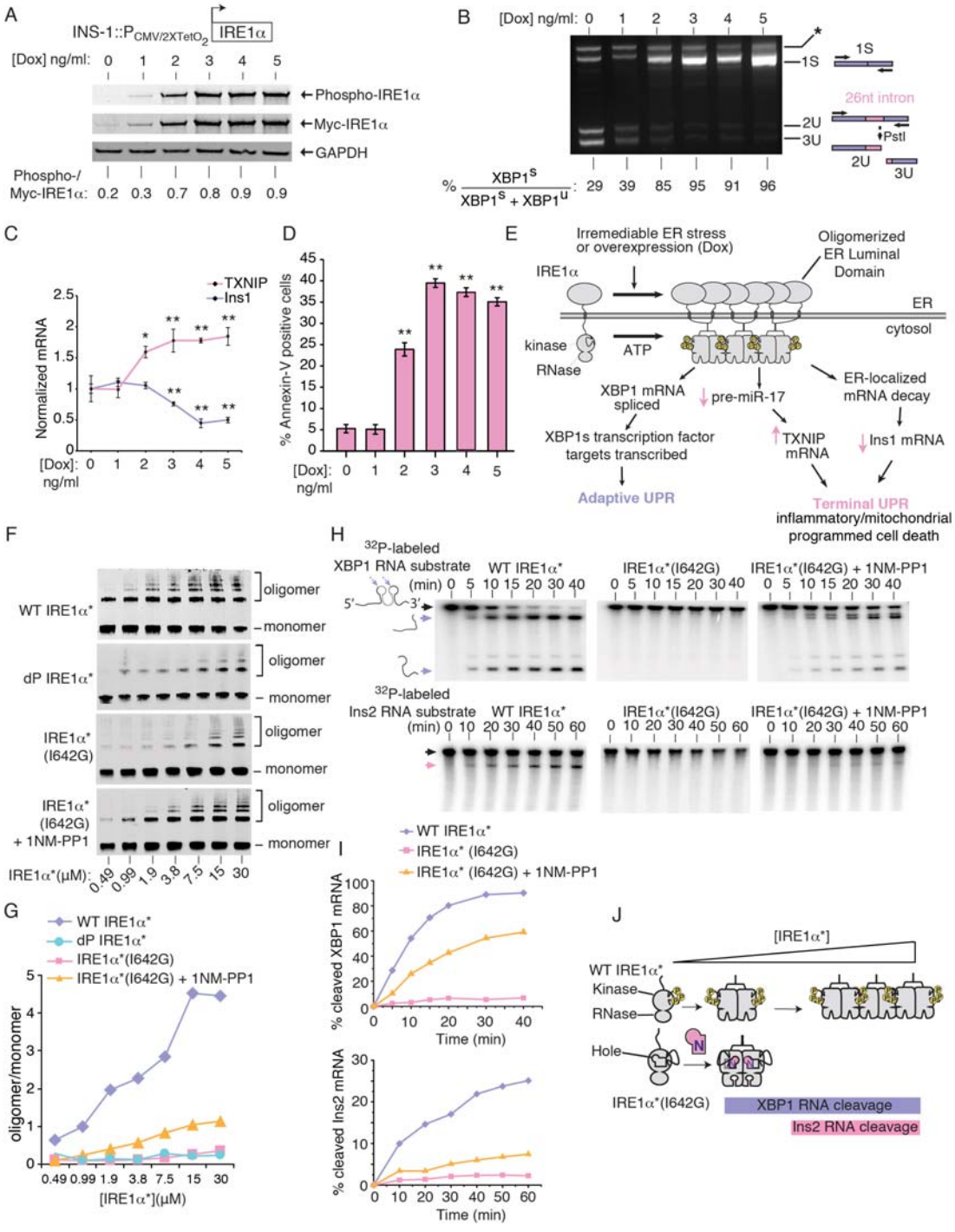

Figure 3.2. IRE1α's kinase uses homo-oligomerization as a rheostat to control RNase activity and apoptosis.
(A) Anti-phospho-IRE1α and anti-Myc immunoblots (ratiometric quantitation, normalized to GAPDH). (B) Agarose gel of PstI-digested XBP1 cDNA amplicons (ratiometric quantitation of spliced to total XBP1 cDNAs). (C) Q-PCR for Insulin1

(Ins1) and TXNIP mRNAs. (D) %Annexin-V positive staining. (A-C) utilized INS-1::IRE1α (WT) cells under increasing [Dox] at 24hr, whereas (D) is at 72 hr. (E) Model of how IRE1α promotes both adaptive and apoptotic outputs. (F) Immunoblots of increasing concentrations of IRE1α*(WT), dP-IRE1α*(WT), and IRE1α*(I642G) -/+ 1NM-PP1 (10 μM) followed by disuccinimidyl suberate (DSS) (250 μM) crosslinking, with oligomer/monomer quantification (G). (H) Time course urea PAGE of cleavage of ^{32}P-labeled XBP1 RNA and Insulin2 (Ins2) RNA by IRE1α*(WT) and IRE1α*(I642G) -/+ 1NM-PP1 (10 μM), with quantification (I). (J) Model of oligomerization-dependence of RNase activity against XBP1 and Ins2 RNAs by IRE1α*(WT) and IRE1α*(I642G). Three independent biological samples were used for XBP1 splicing, Q-PCR and Annexin V experiments. Data plotted as mean value ± SD. P-values: *<0.05 and ** <0.01, ns=not significant.

We next tested the impact of IRE1α*oligomerization on RNase activity against *in vitro*-transcribed XBP1 RNA and a less efficient substrate, Ins2 RNA, derived from one of the two mRNA isoforms encoding rodent proinsulin (Figure 3.2H,I). We also utilized an IRE1α* variant whose oligomeric state can be controlled with a small molecule. Mutation of IRE1α* at the isoleucine (I) gatekeeper residue to glycine (G) in its kinase ATP-binding pocket creates a "hole"—IRE1α* (I642G); in the full-length protein the I642G mutation cripples autophosphorylation [10]. As with dP-IRE1α*, IRE1α* (I642G) has reduced oligomerization compared to IRE1α* (Figure 3.2F,G). 1NM-PP1 is a "bumped" kinase inhibitor that selectively binds mutant kinases that contain glycine gatekeeper residues. Working as a ligand, 1NM-PP1 increases IRE1α* (I642G) oligomerization, but to levels well below those of equimolar IRE1α*.

Consistent with partial increases in oligomeric state, RNase activity is revived in 1NM-PP1-bound IRE1α* (I642G), but with activity largely confined to XBP1 RNA (Figure 3.2H,I). Therefore, both IRE1α* and 1NM-PP1-bound IRE1α* (I642G) efficiently cleave XBP1 RNA, but only IRE1α* surpasses the

oligomerization threshold needed to catalyze the more sluggish Ins2 RNA cleavage reaction (Figure 3.2J). Thus, oligomerization state directly impacts IRE1α's RNA substrate specificity.

We next tested effects *in vivo*. Upon self-association of its overexpressed lumenal domains, an INS-1 line expressing IRE1α (I642G) fully splices XBP1 mRNA under 1NM-PP1, without ER stress, and without causing Ins1 mRNA decay or apoptosis (Figure 3.1G). In fact, without 1NM-PP1, IRE1α (I642G) even reduces apoptosis under ER stress, acting as a strong dominant-negative (Figure 3.1H). Another kinase-dead mutant, IRE1α (K599A) (which is also RNase-dead), and an RNase-dead mutant, IRE1α (N906A) are also strongly dominant-negative for apoptosis (Figure 3.1H).

We previously showed that pre-emptively producing XBP1s, 1NM-PP1–activated IRE1α (I642G) provides a metastable degree of cytoprotection against subsequent ER stress [10, 16], as does forced expression of XBP1s, shown here (Figure 3.1I). However, without a window of sufficient time to permit adaptive pre-conditioning, simultaneous provision of 1NM-PP1 and ER stress agents rescues Ins1 mRNA decay and apoptosis, in 1NM-PP1 dose-dependent manner (Figure 3.1J,K).

Further supporting the notion that IRE1α triggers apoptosis using its RNase, a "holed"-RNase-dead double mutant—IRE1α (I642G/N906A)—remains dominant-negative under 1NM-PP1 (Figure 3.1L). In aggregate, the chemical-genetic studies show that the oligomeric state of IRE1α kinase/RNase subunits impacts both RNA substrate selection and cell fate, and that discrete,

intermediate activation states are available to the effector catalytic domains (Figure 3.1M).

Divergent allosteric modulation of IRE1α oligomeric state and RNase activity with distinct kinase inhibitors.

As with the rationally-engineered mutants, we find that intermediate activation states in IRE1α occur naturally through rare somatic *Ire1α* gene mutations found in human cancers, including glioblastoma, lung adenocarcinoma and serous ovarian cancer [17]. We predicted that five mutations spanning the kinase and RNase should affect function: four are missense, and one, Q780*, that is nonsense, amputates the entire RNase (Figure 3.3A). Expressed conditionally in isogenic INS-1 lines, the human IRE1α cancer mutants are all compromised for apoptosis (Figure 3.3B). Normalized to wild-type, the mutations significantly abrogate auto-phosphorylation and XBP1 splicing (Figure 3.3C-E). Expression of severely crippled IRE1α (Q780*) or IRE1 α (P830L) actually increases Ins1 mRNA levels (Figure 3.3F), suggesting that some basal decay may even be blocked. Cells expressing IRE1α (Q780*) or IRE1α (P830L) proliferate well, in contrast to those expressing IRE1α (WT) or parental lines under ER stress (Figure 3.3H). The mRNA encoding cyclin-dependent kinase inhibitor, p21, is strongly induced in cells expressing IRE1α (WT), but not IRE1α (Q780I) or IRE1α (P830L) (Figure 3.3I). Marking cycling cells, Ki67 sharply declines upon expression of IRE1α (WT), but not IRE1α (Q780*) or IRE1α (P830L) (Figure 3.3J).

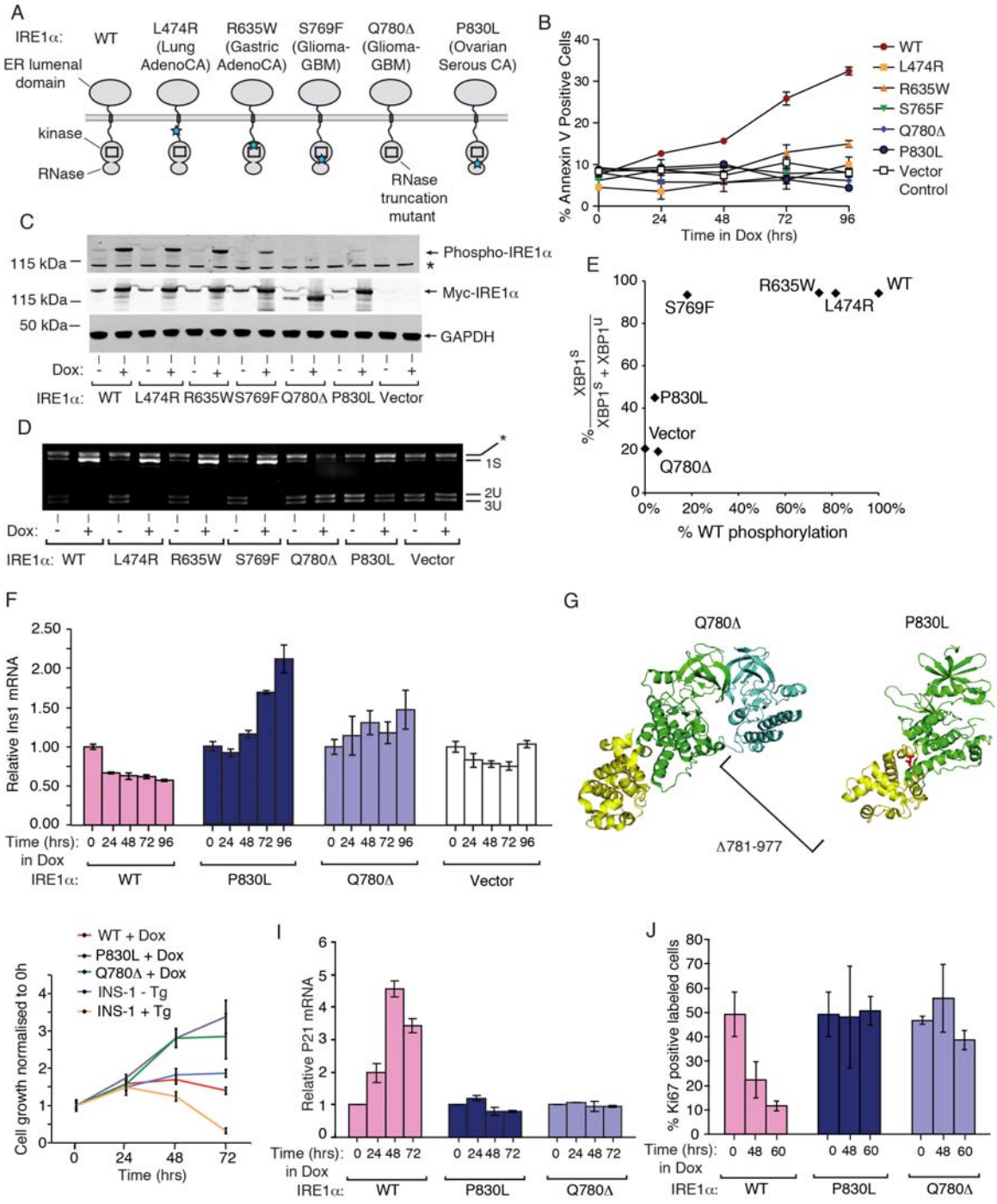

Figure 3.3. IRE1α cancer mutants are disabled for apoptosis.
(A) Cancer-associated mutations in human IRE1α. (B) Time course Annexin-V staining of INS-1 cells stably expressing human IRE1α (WT), (L474R), (R635W), (S765F), (Q780*), and (P830L) under saturating Dox (1μg/ml). (C) Anti-phospho-IRE1α and anti-Myc immunoblots, and (D) agarose gel of PstI-digested XBP1 cDNA amplicons from INS-1 cells expressing human IRE1α (WT) and mutants with Dox (1μg/ml) for 24hr. (E) XBP1 splicing from (D) as a function of IRE1α

phosphorylation from (C). (F) Time course Q-PCR of Ins1 mRNA from INS-1 cells expressing IRE1α (WT) and mutants under Dox (1μg/ml). (G) Cartoon of monomeric human IRE1α (P830L) (right panel) and IRE1α (Q780*) dimerized with a IRE1α (WT) subunit (left panel) based on PDB: 3P23. (H) Time course MTT staining of INS-1 cells expressing IRE1α (WT), IRE1α (P830L) or IRE1α (Q780*) -/+ Dox (1μg/ml), or parental INS-1 cells -/+ 100 nM Tg. (I,J) Time-course Q-PCR for p21 mRNA, and Ki67 staining, from INS-1 IRE1α (WT), IRE1α (P830L) or IRE1α (Q780*) cells under Dox (1μg/ml). Three independent biological samples were used for Q-PCR, Ki67, and Annexin V experiments. Data plotted as mean +/- SD.

Lack of the RNase in IRE1α (Q780*) converts it into a dominant-negative (Figure 3.4A-D). The destabilize a dimerization interface [18]. We predicted and tested that RNase activity in IRE1α (P830L) can be rescued with a kinase inhibitor, as IRE1α (I642G) can with 1NM-PP1.

We previously employed two distinct classes of kinase inhibitors—types I and II—to stabilize alternate kinase active site conformations in IRE1α [19]. APY29 is a type I kinase inhibitor of IRE1α that stabilizes an *active* kinase domain conformation, which is typically adopted by ATP-bound kinases. By stabilizing the active kinase conformation, type I inhibitors act as ligands that allosterically activate IRE1α's RNase; e.g., 1NM-PP1 is a type I inhibitor of IRE1α (I642G).

Compared to IRE1α* (WT), IRE1α* (P830L) has reduced kinase activity (Figure 3.5A), as the full-length protein does *in vivo* (Figure 3.3C). APY29 dose-dependently suppresses residual autophosphorylation of IRE1α* (P830L) (Figure 3.5B). IRE1α* (P830L) cannot cleave a FRET-quenched XBP1 RNA mini-substrate [10] (Figure 3.5C-E), consistent with reduced RNase activity *in vivo* (Figure 3.3D). But opposite to effects on kinase activity, APY29 increases IRE1α* (P830L)'s oligomeric state to rescue RNase activity (Figure 3.5D-G).

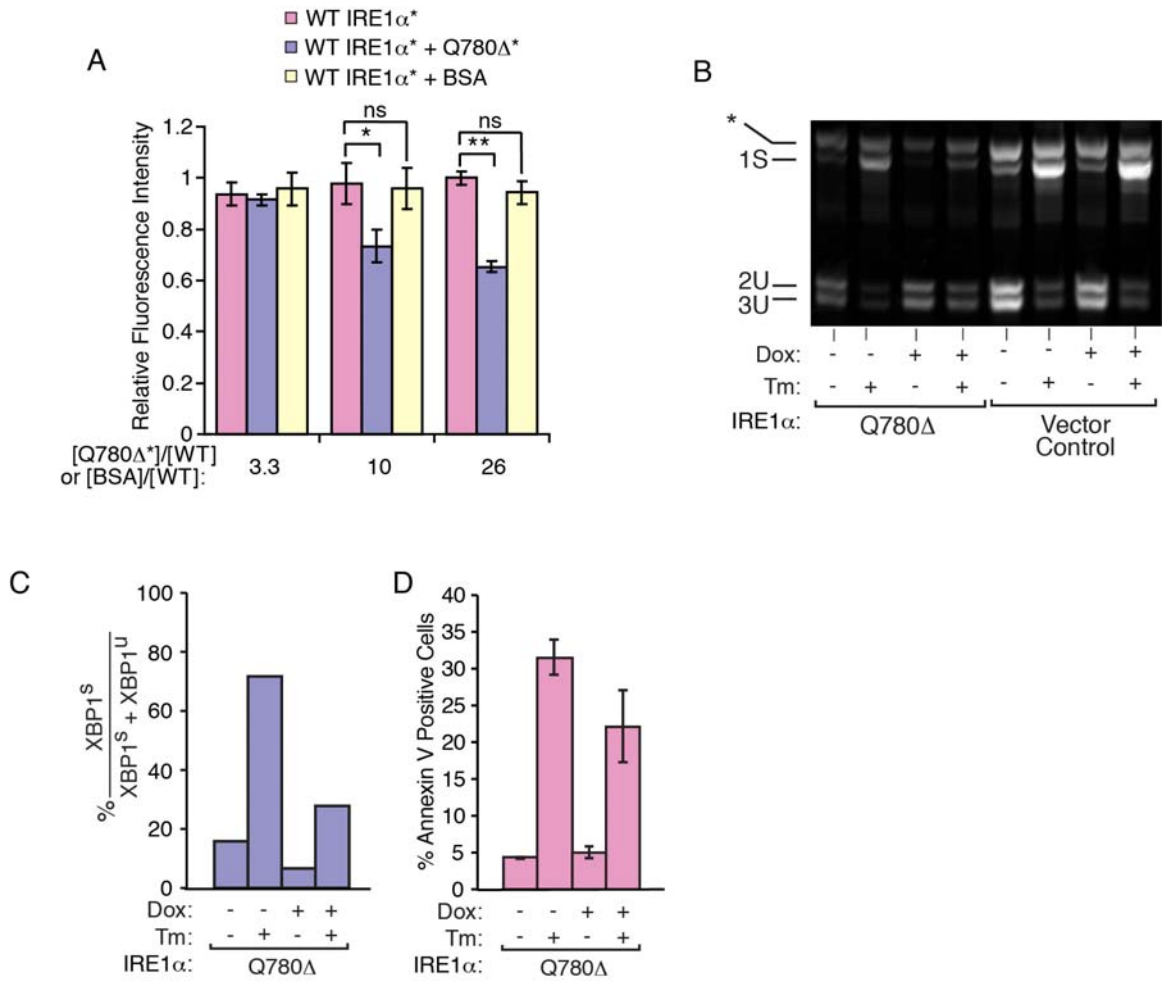

Figure 3.4. The IRE1α (Q780*) cancer mutant functions as a dominant negative against XBP1 splicing and apoptotic activities of IRE1α (WT). (A) RNase activities of recombinant IRE1α* as measured by the cleavage of the 5'FAM-3'BHQ-labeled XBP1 minisubstrate. Wild type (WT) IRE1α* was mixed with IRE1α*(Q780*) or BSA by fixing [WT IRE1α*] at 0.1 μM and varying [IRE1α*(Q780*)] or [BSA] as indicated. (B) EtBr-stained agarose gel of XBP1 cDNA amplicons from INS-1 IRE1α human (WT) and human IRE1α (Q780*) stable cells treated with 1 μg/ml Dox for 24hr prior to treatment with 100 ng/ml Tm for 8hr. (C) Quantification of percent XBP1 splicing from (B). (D) Percent of INS-1 human IRE1α (Q780*) stable cells staining positive for Annexin V after Dox (1 μg/ml) for 48hr followed by treatment with 50 ng/ml Tm for 72hr. Three independent biological samples were used for Annexin V staining experiments. Data are plotted as means +/- SD. p-values: * <0.05, **<0.01.

If, as all preceding results suggest, kinase-driven oligomerization of IRE1α hyperactivates its RNase to trigger apoptosis, then kinase inhibitors that block oligomerization should prevent apoptosis under ER stress. To this end, we employed type II kinase inhibitors that stabilize an *inactive* ATP-binding site conformation in IRE1α. We previously developed a subset of type II kinase inhibitors designated KIRAs, for Kinase-Inhibiting RNase-Attenuators, that inhibit IRE1α's RNase activity by breaking oligomers [19]. Since our original report, we have identified KIRA6 as a more potent version (Figure 3.5H). KIRA6 dose-dependently inhibits IRE1α* (WT) kinase activity, XBP1 RNA cleavage, Ins2 RNA cleavage (with lower IC_{50} than for XBP1 RNA in a competition assay), and oligomerization (Figure 3.5I-L).

To follow IRE1α oligomerization *in vivo,* we first tested a reporter called IRE1-3F6HGFP that contains an EGFP domain positioned near the kinase [20], but found that it has attenuated XBP1 splicing and fails to induce apoptosis (Figure 3.6A,B). To avoid potential steric effects on the kinase, we constructed a superfolder green fluorescent protein (sfGFP) N-terminally fused to the ER lumenal domain. Expressed isogenically in INS-1 cells, sfGFP- IRE1α retains apoptotic activity and gathers into discrete fluorescent foci in the ER membrane under the ER stress agent dithiothreitol (DTT) (Figure 3.5M, 3.6A,B). An (I642G) version of sfGFP- IRE1α fully splices XBP1 mRNA under 1NM-PP1 without forming foci (Figure 3.6C,D). In fact, without 1NM-PP1, sfGFP- IRE1α (I642G) resists forming foci under DTT, suggesting that without its ligand it adopts an inactive kinase conformation and explaining dominant-negative effects of IRE1α

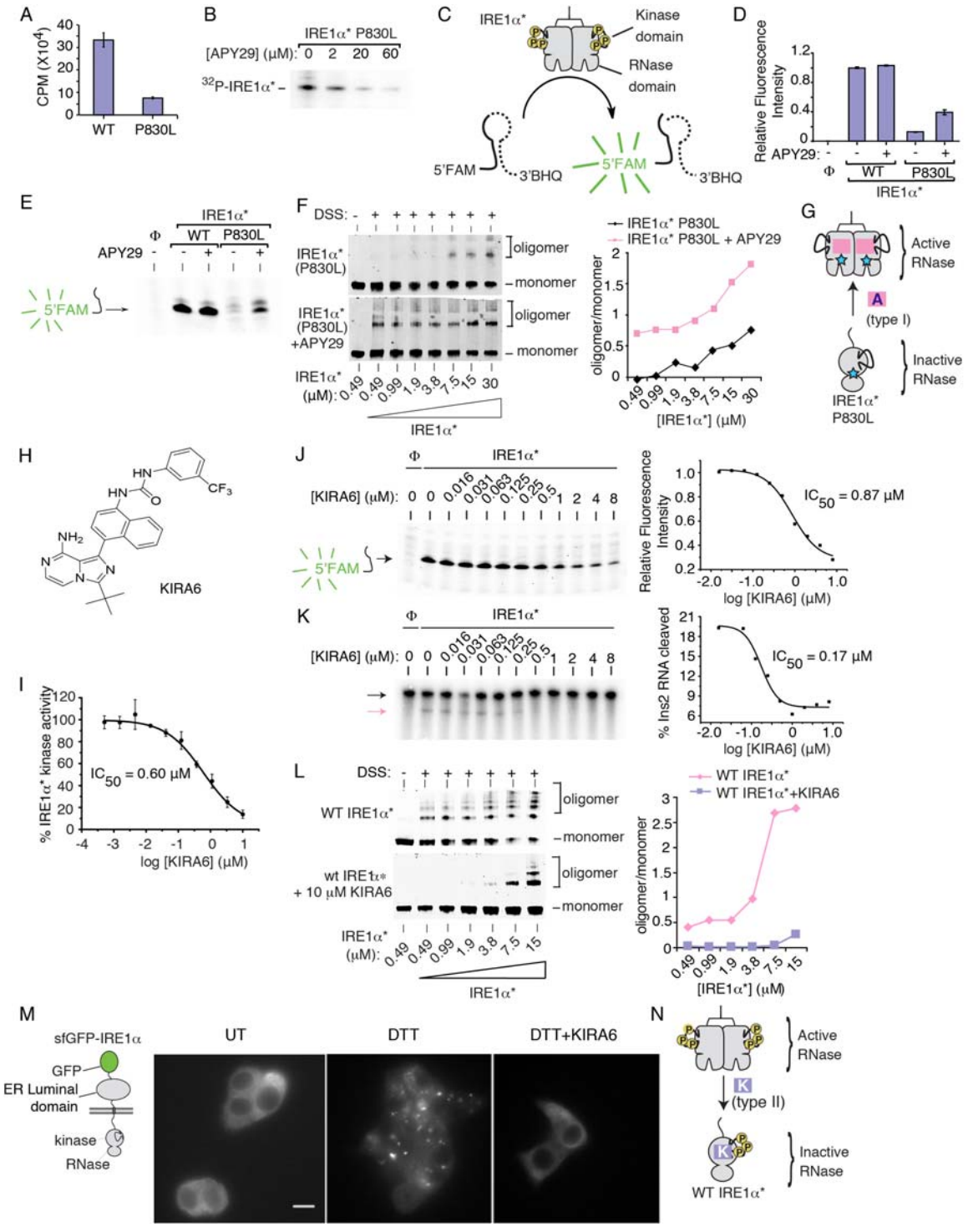

Figure 3.5. Divergent modulation of IRE1α RNase activity using distinct classes of kinase inhibitors.

(A) Phosphorimager analysis of human IRE1α* (25 nM) and IRE1α* (P830L) (25 nM) kinase activity against peptide substrate (PAKtide, 2 μM) in the presence of ^{32}Pγ-ATP. (B) Autoradiogram of IRE1α* (P830L) autophosphorylation under increasing [APY29]. (C) 5'FAM-3'BHQ XBP1 minisubstrate to measure RNase

activity. (D) RNase activities of IRE1α* and IRE1α* (P830L) -/+ APY29 (20 μM) per (C). (E) Urea PAGE of XBP1 cleavage products from (D). (F) Immunoblots of increasing IRE1α* (P830L) after incubation with DMSO or APY29 (200 μM) and DSS, with oligomer/monomer quantification. (G) Model of APY29 rescue of oligomerization and RNase activity in IRE1α* (P830L). (H) Structure of KIRA6. (I) KIRA6 inhibition of IRE1α* kinase activity. IC_{50} values by fitting percent kinase activity per assay in (A) (*n* = 3). (K) Urea PAGE of competition cleavage by IRE1α* of XBP1 RNA mini-substrate (J) and ^{32}P-labeled Ins2 RNA (K), under indicated [KIRA6]; IC_{50}s by fitting in-gel fluorescence intensities (XBP1) and phosphorimager (Ins2). (L) Immunoblots of increasing [IRE1α*] incubated with DMSO or KIRA6 (10 μM) and DSS, with oligomer/monomer quantification. (M) Left: cartoon of sfGFP-IRE1α reporter. Right: Images of sfGFP-IRE1α induced with (sub-apoptotic) 1ng/ml Dox for 24hr in INS-1 cells -/+ DTT (5 mM) for 1hr -/+ KIRA6 (1 μM). Scale bar is 5 μm. (N) Model for how KIRA6 lowers oligomeric status and RNase activity of IRE1α*. Data plotted as mean +/- SD.

(I642G)(Figure 3.1H). Similar to apoptosis, foci formation by sfGFP- IRE1α (I642G) requires both ER stress and 1NM-PP1, further supporting the tight link between IRE1α oligomerization—shown *in vivo* through foci—and apoptosis. Thus, using sfGFP- IRE1α, which faithfully recapitulates cytosolic events, we tested and found that KIRA6 prevents foci formation by DTT (Figure 3.5M). Hence, KIRAs fulfill their design principle of breaking kinase/RNase oligomers to inhibit the RNase (Figure 3.5N).

KIRA6 inhibits IRE1α in vivo to preserve cell viability and function in diverse cells and rodent tissues experiencing ER stress.

The remainder of our work focused on testing physiological effects of IRE1α kinase inhibition. APY29 showed pleiotropic toxicity, including proliferative blocks at low micromolar concentrations, precluding further *in vivo* testing of ON-target effects (Figure 3.7A). In contrast, KIRA6 had negligible toxicity up to 10 μM

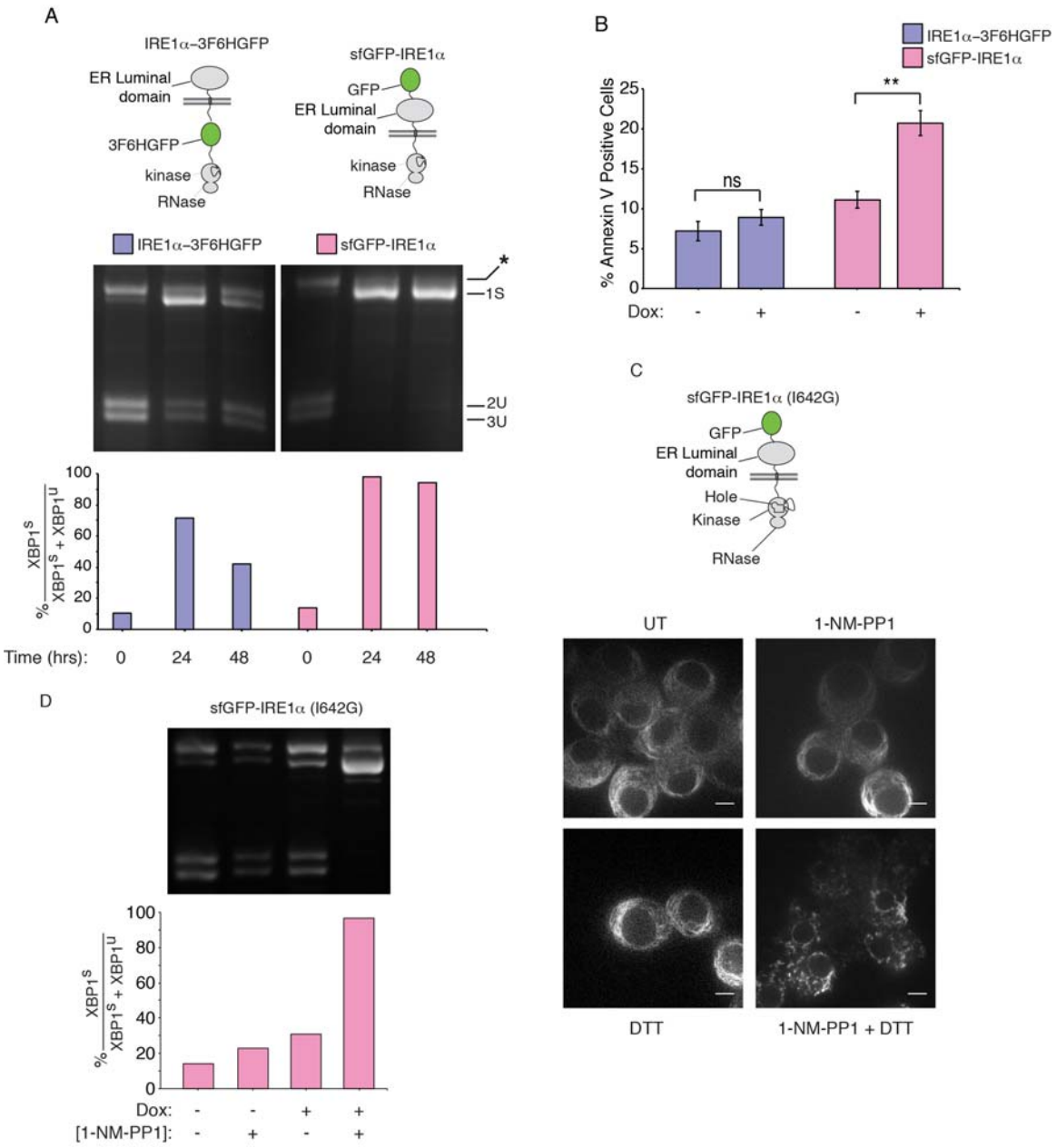

Figure 3.6. sfGFP-IRE1α reporter exhibits pro-apoptotic features of IRE1α and sfGFP- IRE1α (I642G) demonstrates graded oligomerization states. (A) Model of N-terminal sfGFP-IRE1α and Kinase/RNase linker IRE1α-3F6HGFP reporter (top panel). EtBr-stained agarose gel of XBP1 cDNA amplicons from INS-1 sfGFP-IRE1α and INS-1 IRE1α-3F6HGFP isogenic stable cells treated with 1 μg/mL Dox for indicated times (center panel). Lower panel shows quantification of percent XBP1 splicing above. (B) Percentage of Annexin V positive INS-1 sfGFP-IRE1α and IRE1α-3F6HGFP stable cells treated with 1 μg/mL Dox for 96hr. Three independent biological samples were used for Annexin V staining experiments. Data are plotted as means +/- SD. p-values: **<0.01, ns= not significant. (C) Model of N-terminal sfGFP-IRE1α (I642G)

reporter (top panel). Images show sfGFP-IRE1α (I642G) induced with 1 ng/ml Dox for 12hr in INS-1 cells +/- DTT (5 mM) for 20 min either in the presence or absence of 1NM-PP1 (5 μM). Scale bar is 5 μm. (D) EtBr-stained agarose gel of XBP1 cDNA amplicons from INS-1 sfGFP-IRE1α (I642G) stable cells treated with 1 μg/ml Dox for indicated times (center panel). Lower panel shows quantification of % XBP1 splicing above.

(Figure 3.7A), providing a favorable therapeutic index to test cytoprotection. INS-1 lines confirmed ON-target effects: Pro-Caspase-3 cleavage upon IRE1α (WT) expression is prevented by KIRA6 (Figure 3.8A). Moreover, despite its inability to directly inhibit JNK activity *in vitro,* KIRA6 strongly inhibits JNK phosphorylation from IRE1α hyperactivation or ER stress (Figure 3.8A-C). Also, KIRA6 dose-dependently inhibits Ins1 mRNA decay, proinsulin depletion, and apoptosis from IRE1α hyperactivation (Figure 3.8D-F).

Chemical-genetic tools enabled ON-target competition tests. KIRA6: [**1**] reduces 1NM-PP1-induced XBP1 RNA cleavage by IRE1α* (I642G) *in vitro* (Figure 3.8G); [**2**] antagonizes 1NM-PP1-induced XBP1 splicing by IRE1α (I642G) *in vivo* (Figure 3.8H); and [**3**] reduces 1NM-PP1 potentiation of Ins1 mRNA decay and apoptosis during ER stress, in dose-dependent manner (Figure 3.8I, 3.7B,C). KIRA6 does not inhibit the activity of a panel of Ser/Thr kinases (including JNK2 and 3) *in vitro* (Figure 3.7D). Moreover, KIRA6 does not inhibit nor secondarily promote eIF2α phosphorylation by PERK, the other UPR kinase (Figure 3.7E).

Having confirmed that KIRA6 has ON-target effects, we next tested efficacy against endogenous IRE1α using the established ER stress regimes in their linear ranges straddling the apoptotic trigger point (Figure 3.1A). In INS-1

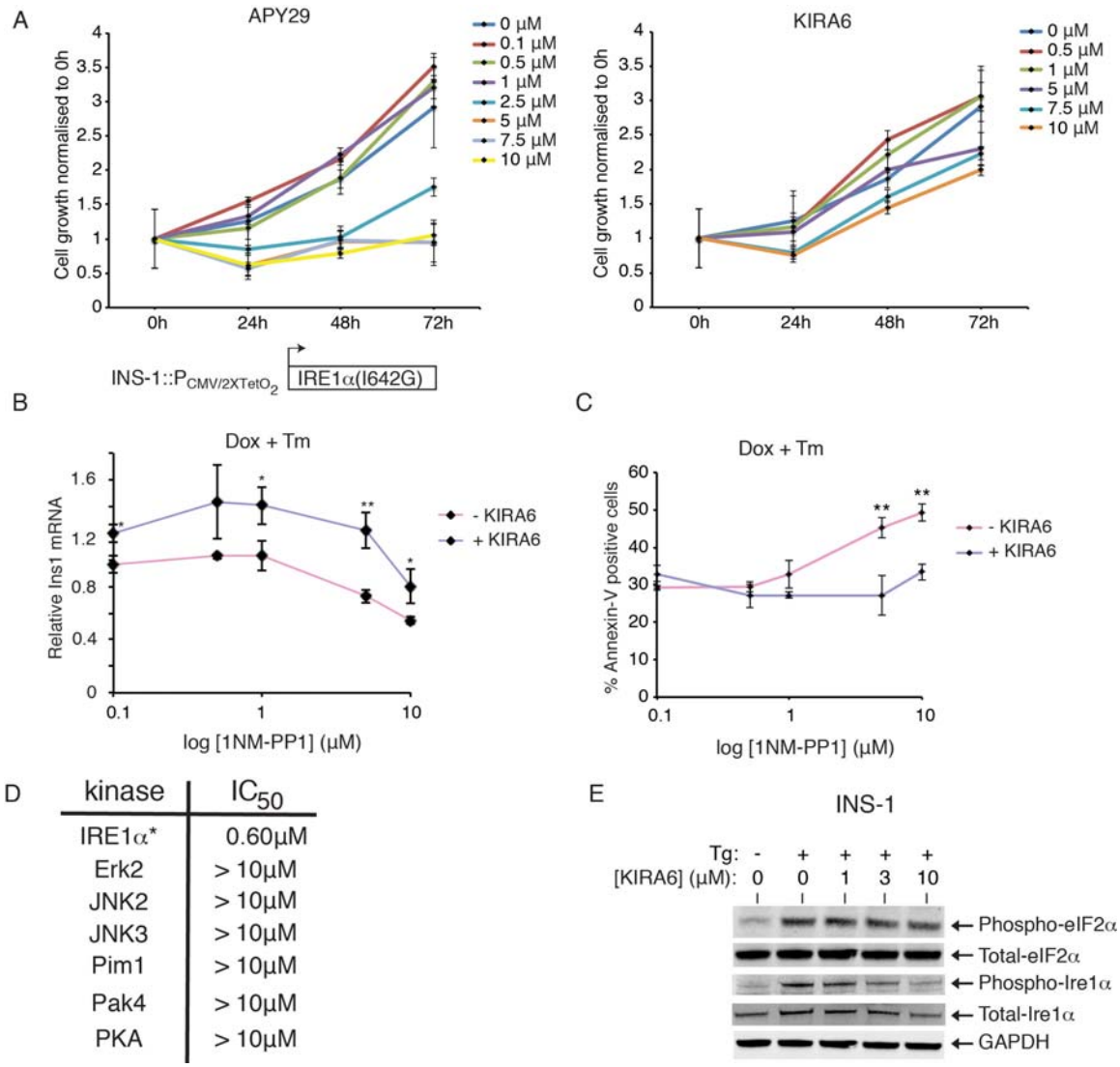

Figure 3.7. KIRA6 and 1NM-PP1 have opposing effects on IRE1α (I642G). (A) MTT assay of INS-1 cells treated with increasing concentration of APY29 (left panel) and KIRA6 (right panel) for indicated timepoints. Data are shown from 3 biological replicates and plotted as means +/- SD. (B) Q-PCR for Insulin1 (Ins1) mRNA (normalized to GAPDH) in Dox treated INS-1 IRE1α (I642G) cells treated with Tm (0.5 µg/ml) and increasing concentrations of 1NM-PP1 in the presence or absence of KIRA6 (1 µM) for 24hr. (C) Percentage of INS-1 IRE1α (I642G) cells staining positive for Annexin V after treatment for 72hr with Dox (1 µg/ml), Tm (0.5 µg/ml), and increasing concentrations of 1NM-PP1 in the presence or absence of KIRA6 (1 µM). Data are from 3 biological replicates and plotted as means +/- SD. p-values: *<0.05, ** <0.01. (D) Table showing IC_{50} values of kinase inhibitory activity of KIRA6 against a panel of 7 indicated kinases *in vitro*. (E) Immunoblots for phospho-eIF2α and total eIF2α, phospho-IRE1α and total IRE1α in INS-1 cells pretreated for 1hr with indicated concentrations of KIRA6, followed by treatment with Tg (1 µM) for 2hr. GAPDH serves as a loading control.

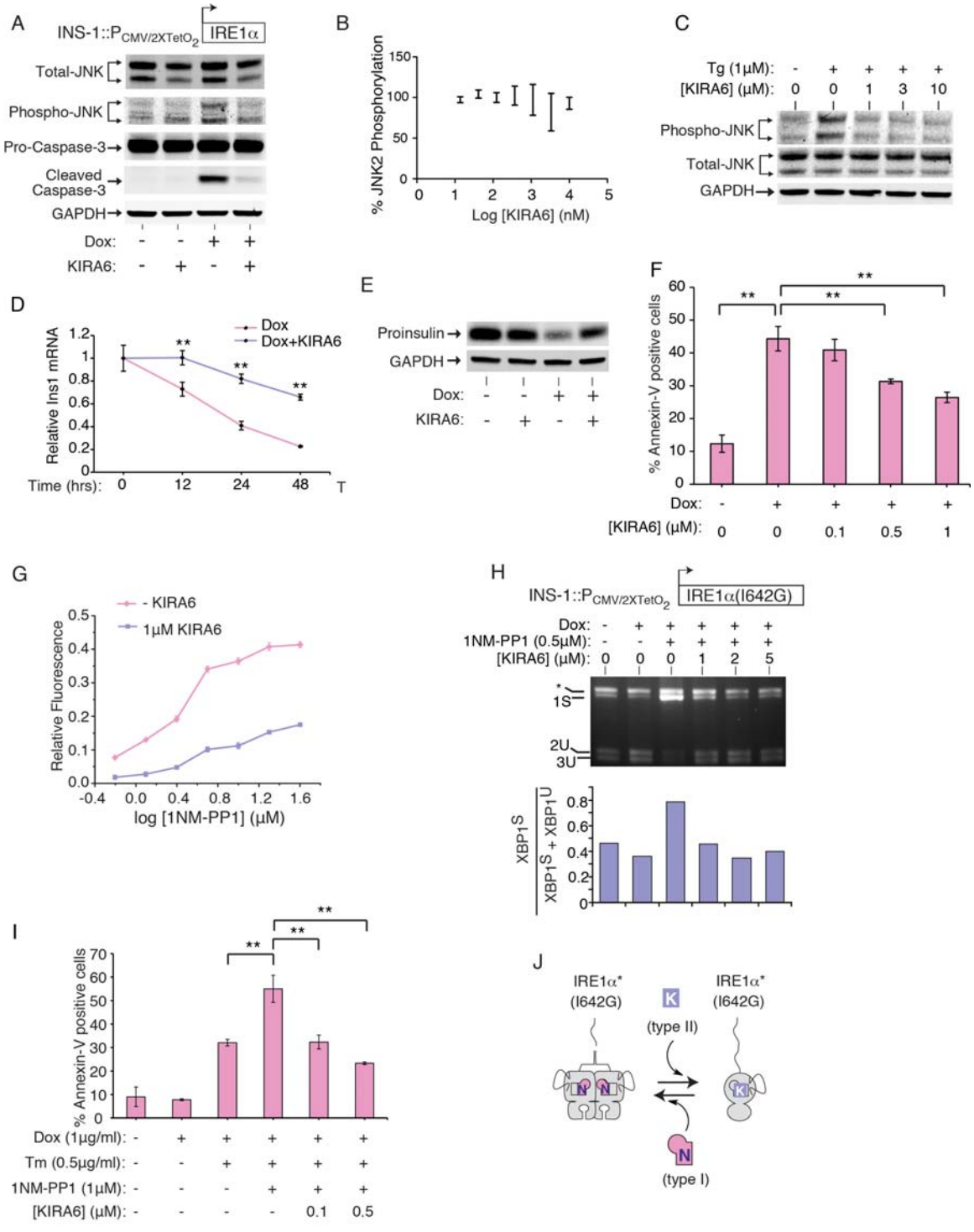

Figure 3.8. KIRA6 inhibits IRE1α Terminal UPR outputs and apoptosis. (A) Anti-total JNK, anti-phospho-JNK, and anti-Pro- and Cleaved Caspase-3 immunoblots of INS-1 IRE1α (WT) cells treated with Dox (5 ng/ml) -/+ 1μM KIRA6 for 72hr. (B) JNK2α1 phosphorylation under indicated [KIRA6] by *in vitro* ELISA-based anti-phospho-JNK assay. (C) Anti-total and phospho-JNK immunoblots of INS-1 cells pretreated for 1hr with indicated [KIRA6], then 1□M

Tg for 2hr. (D) Q-PCR for Ins1 mRNA in INS-1 IRE1α (WT) cells treated with Dox (5 ng/ml) -/+ KIRA6 (1 μM). (E) Anti-Proinsulin immunoblot of samples in (A). (F) % Annexin V staining in INS-1 IRE1α (WT) cells after 72hr in Dox (5 ng/ml) and indicated [KIRA6]. (G) Competition between indicated [1NM-PP1] and KIRA6 (1 μM) for IRE1α* (I642G) RNase. (H) Agarose gel of PstI-digested XBP1 cDNA amplicons from INS-1 cells IRE1α (I642G) cells induced by Dox (1 μg/ml) for 24hr, then 1NM-PP1 (0.5 μM) -/+ indicated [KIRA6] for 3hr, with quantitation. (I) Annexin V staining of INS-1 IRE1α (I642G) cells after 72hr with Dox (1 μg/ml), Tm (0.5 μg/ml), 1NM-PP1 (1 μM) and indicated [KIRA6]. (J) Model of 1NM-PP1 and KIRA6 competition of oligomerization and RNase activity in IRE1α* (I642G). Data plotted as mean +/- SD. P-values: *<0.05, ** <0.01.

cells, KIRA6 inhibits IRE1α auto-phosphorylation by Tg and XBP1 mRNA splicing by Tm in a dose-dependent manner (Figure 3.9A-C); whereas, a control analog, (NMe)KIRA6, incapable of binding to the kinase hinge region, inhibits neither output at 10 μM (Figure 3.9A,B, 3.10A,B).

We next tested multiple Terminal UPR endpoints and found that KIRA6: [**1**] Inhibits Ins1 and Ins2 mRNA decay by Tm in INS-1 cells in dose-dependent manner (Figure 3.9D, 3.10C). We noted that the *in vivo* IC_{50} of KIRA6 for Ins1 mRNA rescue is lower than that for inhibiting XBP1 splicing, and Ins2 mRNA levels recover even at 20 nM KIRA6 and exceed basal, untreated levels in dose-dependent manner. Furthermore, KIRA6: [**2**] Inhibits TXNIP induction by Tm in murine C57BL/6 pancreatic islets (Figure 3.9E); [**3**] Inhibits IRE1α-dependent activation of a TXNIP 3'UTR luciferase reporter containing its two miR-17 binding sites (Figure 3.10D); [**4**] Prevents 1L-1β secretion by Tm and Tg (but not ATP) in THP1 macrophage lines (Figure 3.9F); [**5**] Prevents loss of INS-1 Ki67-positive cells and C57BL/6 pancreatic islet double-positive Nkx6.1/EdU β-cells under ER stress (Figure 3.9G,H, 3.10E); [**6**] Dose-dependently inhibits apoptosis of INS-1 cells under BFA (Figure 3.9I); [**7**] Reduces TUNEL staining of β-cells in C57BL/6

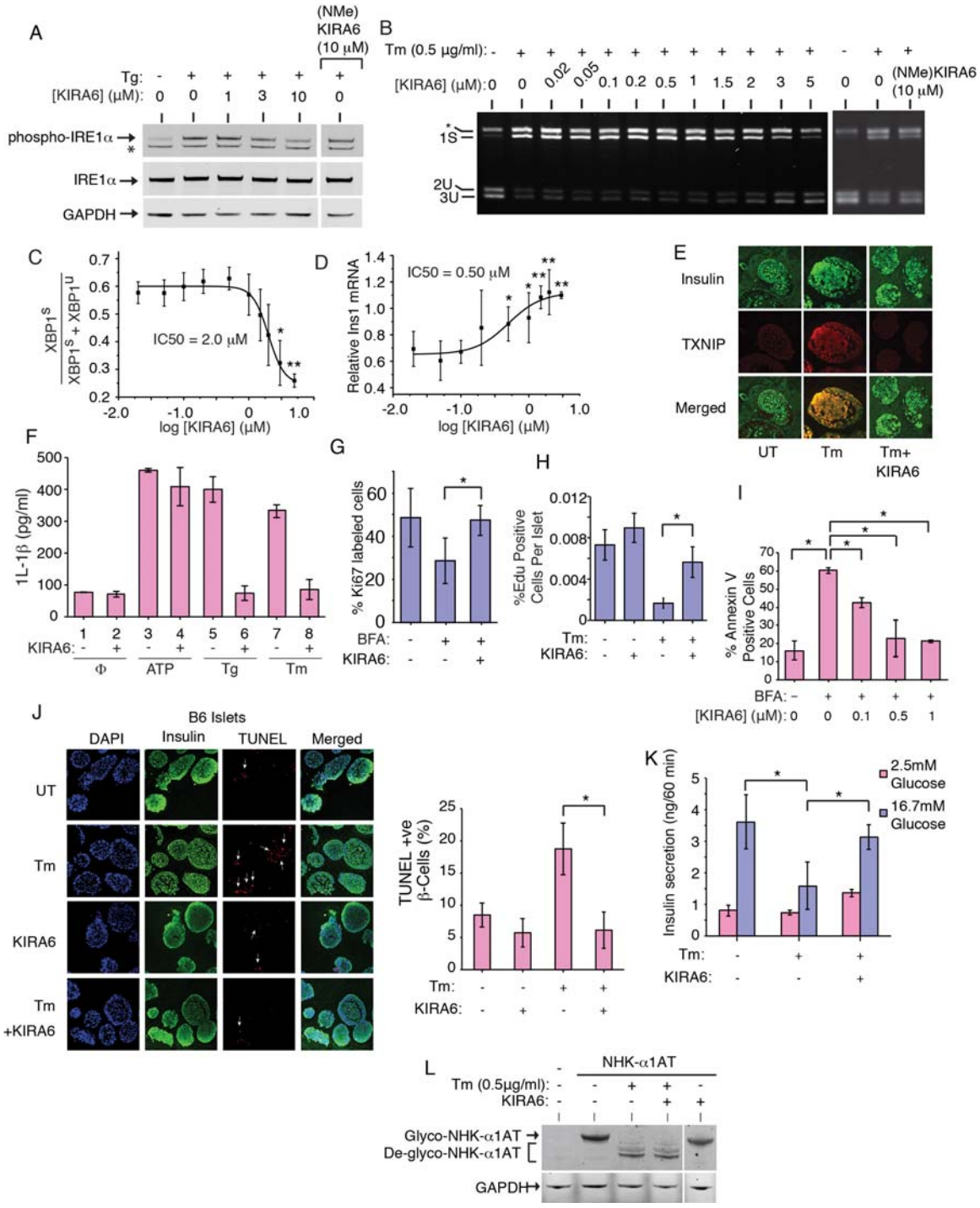

Figure 3.9. KIRA6 reduces ER stress-induced death of cultured cells and in pancreatic islet explants.

(A) Immunoblots for total and phospho-IRE1α in INS-1 cells pretreated for 1hr with indicated [KIRA6], or 10 μM (NMe)KIRA6, then Tg (1 μM) for 2hr. (B) Agarose gel of XBP1 cDNA amplicons from INS-1 cells pre-treated with indicated [KIRA6] for 1hr, or 10 μM (NMe)KIRA6, followed by 0.5 μg/ml Tm for 8hr. (C) Ratios of $XBP1^S$ over ($XBP1^S$ + $XBP1^U$) from (B). (D) Q-PCR for Ins1 mRNA

(normalized to no Tm) in INS-1 cells pretreated for 1hr with indicated [KIRA6], then 12hr in Tm (0.5 μg/ml). (E) Immunofluorescence: Insulin (green) and TXNIP (red) in islets of C57BL/6 mice under 0.5μg/ml Tm -/+ 0.5 μM KIRA6 for 16hr. (F) IL-1β secretion from THP-1 cells after 4hr -/+ 0.5 μM KIRA6, 5 μg/ml Tm, 1 μM Tg, or 5 mM ATP. (G) Ki67+ INS1 cells under 0.25 μg/ml BFA -/+ 0.5 μM KIRA6 for 48hr. (H) Proliferating mouse islet β-cells under 0.5 μg/mL Tm -/+ 0.5 μM KIRA6 for 48hr (nuclei double-positive for EdU and β-cell nuclear marker, Nkx6.1, over total Nkx6.1 positive nuclei). (I) Annexin-V staining of INS-1 cells treated with 0.25 μg/ml BFA and indicated [KIRA6] for 72hr. (J) Immunofluorescence images of C57BL/6 islets treated with 0.5 μg/mL Tm -/+ 0.5 μM KIRA6 for 16 hr. Co-stained for DAPI (blue), insulin (green), and TUNEL (red). Quantification of TUNEL+ β-cells (white arrows) normalized to DAPI+ cells. (K) Glucose-stimulated insulin secretion (GSIS) by C57BL/6 islets after 0.5μg/mL Tm -/+ 0.5 μM KIRA6 for 16hr; [Glucose] was 2.5 mM or 16.7 mM for 60 min. (L) Immunoblots for alpha-1 anti-trypsin in HEK293 cells transfected with pCDNA3.1-α1hAT-NHK, then treated with KIRA6 (1 μM) -/+ Tm (0.5 μg/ml) for 20hr. Three independent biological samples were used for XBP1 splicing, Q-PCR, Annexin V and immunofluorescence experiments. Data plotted as mean +/- SD. P-values: *<0.05, ** <0.01.

and human islets under Tm (Figure 3.9J, 3.10F); and [**8**] preserves glucose-stimulated insulin secretion (GSIS) in C57BL/6 islets under Tm (Figure 3.9K).

We also tested effects of STF-083010, a small molecule tool compound that reactively modifies Lysine 907 in the RNase active site [21](Figure 3.10G). As with KIRA6, STF-083010 (at 50 μM) also decreases Ins1 mRNA decay under IRE1α hyperactivation and apoptosis by Tm (Figure 3.10H,I). Moreover, when used in combination at doses that are sub-therapeutic individually, STF-083010 (1 μM) and KIRA6 (50 nM) afford significant cytoprotection under Tm (Figure 3.10J). Together, these data further implicate IRE1α's RNase in promoting apoptosis, in this case by showing that the RNase can even be inhibited combinatorially through two distinct sites in IRE1α for cytoprotection.

To rule out the possibility that KIRA6 defeats ER stress agents upstream of IRE1α, we tested whether blocks to ER post-translational modification still

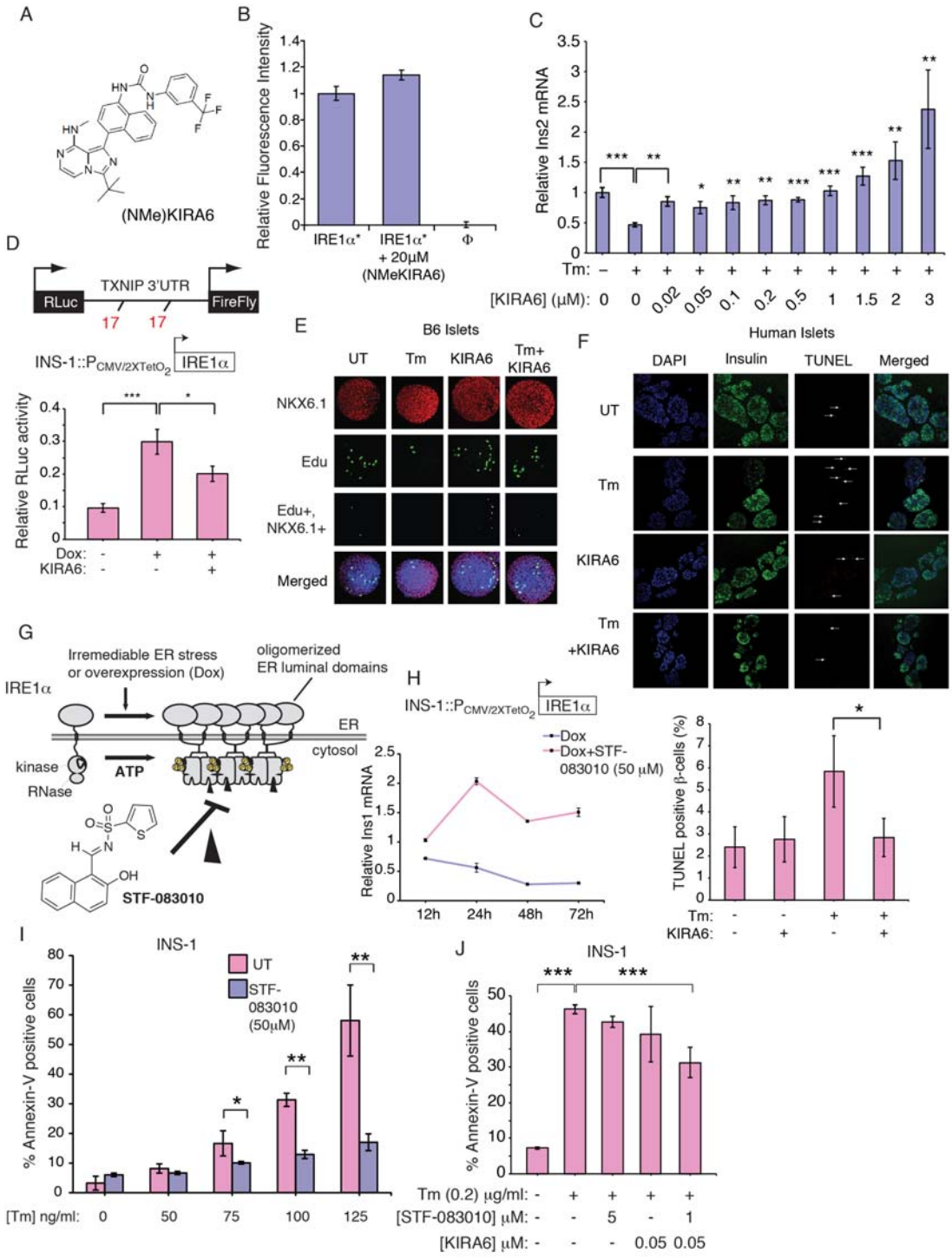

Figure 3.10. KIRA6 inhibits Terminal UPR outputs of IRE1α to protect against ER stress-induced apoptosis.

(A) Structure of (NMe)KIRA6.(B) RNase activity of IRE1α* in the presence or absence of (NMe)KIRA6 (20 μM) as measured by the cleavage of the 5'FAM-3'BHQ-labeled XBP1 minisubstrate. (C) Q-PCR for Insulin2 (Ins2) mRNA in INS-

1 cells 12hr after Tm (0.5 μg/ml) in cells pre-treated for 1hr with indicated [KIRA6]. (D) IRE1α induction of miR-17 binding dependent TXNIP reporter is attenuated by KIRA6. Dox-inducible INS-1 IRE1α (WT) cells were transfected with a luciferase reporter construct containing TXNIP 3' UTR. The cells were treated with or without 100 ng/ml Dox for 24hr, lysed and then analyzed for luciferase activity. Three independent biological samples were used for luciferase experiments. Data are shown as mean +/- SD. *p < 0.05 ;**p < 0.01;***p < 0.005. (E) Immunofluorescence staining of EdU (green) and β-cell nuclear marker, Nkx6.1(red), in C57BL/6 mouse islets treated with 0.5 μg/ml Tm +/-0.5 μM KIRA6 for 48hr. White color shows the co-localization of the red and green channels. (F) Immunofluorescence staining of healthy non-diabetic human islets treated with 0.5 μg/mL Tm +/-0.5 μM KIRA6 for 16hr as indicated. Co-stained for DAPI (blue), insulin (green), and TUNEL (red). Merged image is also shown. Lower panel shows quantification of TUNEL positive β-cells (white arrows) normalized to DAPI-positive cells. **(**G) Structure of STF-083010 and cartoon showing that it directly inhibits the RNase of IRE1α (through covalent modification). **(**H**)** Q-PCR for Ins1 mRNA in INS-1 IRE1α (WT) cells treated with Dox (5 ng/ml) +/- STF-083010 (50 μM) over the indicated timecourse. **(I)** Annexin V staining of INS-1 cells after 72hr with indicated [Tm] +/- STF-083010 (50 μM). **(**J**)** Annexin V staining of INS-1 cells after 72hr with Tm (0.2 μg/ml), STF-083010 (1 or 5 μM), and KIRA6 (0.05 μM) as indicated. Data plotted as mean +/- SD. P-values: *<0.05, ** <0.01, *** <0.005.

persist under KIRA6. A test substrate, the null Hong Kong variant of alpha-1 anti-trypsin (NHK-A1AT), normally glycosylated and ER-retained, is deglycoslyated under Tm. NHK-A1AT clearly remains deglycoslyated under both Tm and KIRA6 (Figure 3.9L).

Encouraged by clear and convincing evidence that KIRA6 preserves cell viability and function in multiple cell and explant systems under diverse ER stress regimes, we next applied a higher evidentiary standard by testing disease-relevant animal models. Given compelling evidence that ER stress contributes to photoreceptor loss in many retinal diseases, including retinitis pigmentosa (RP) [22], we tested KIRA6 in two rodent models. Transgenic rats expressing a misfolded Rhodopsin mutant (P23H) exhibit spontaneous photoreceptor degeneration and are a model of autosomal dominant RP [23]. Retinas of

hemizygous P23H rats develop normally but lose photoreceptors beginning on postnatal day (P) 10; by P40, the outer nuclear layer (ONL), representing photoreceptor nuclei, is reduced to ~50% of the thickness of wild-type rats [24]. We intravitreally injected KIRA6 or carrier into either eye of individual P23H rats at P9 and P15. ONL thickness at P40 revealed partial, yet statistically significant, protection from photoreceptor loss in KIRA6-treated eyes (Figure 3.11A,B).

Given rapid clearance of intravitreally injected small molecules (half-life <60h), we were unable to maintain sufficient KIRA6 in the vitreous over the ~30d progression of retinal degeneration in P23H rats to test for functional protection. Therefore, we used a model of acute photoreceptor loss occurring over 7 days from single intravitreal injection of Tm into adult rats [25]. Intravitreal co-injection of KIRA6 with Tm significantly reduces XBP1 splicing, TXNIP induction, and decay of the ER-localized photoreceptor-specific Rhodopsin mRNA (Figure 3.12A-C). Rhodopsin mRNA may be an IRE1α RNase substrate since Rhodopsin RNA is cleaved by IRE1α*, but not RNase-dead IRE1α* (N906A), at a G/C site with flanking similarity to scission sites in XBP1 (Figure 3.11C; 3.12D,E). KIRA6 dose-dependently inhibits Rhodopsin RNA cleavage by IRE1α* (Figure 3.12F,G). Concomitant with blockage of Terminal UPR outputs, co-injection of KIRA6 in the Tm model reduces photoreceptor loss by Optical Coherence Tomography (OCT) and histology (Figure 3.12H).

Next, to test whether KIRA6 also provides functional protection, we established a dose-response curve to determine threshold [Tm] that cause functional retinal damage as measured by scotopic electroretinograms (ERG)

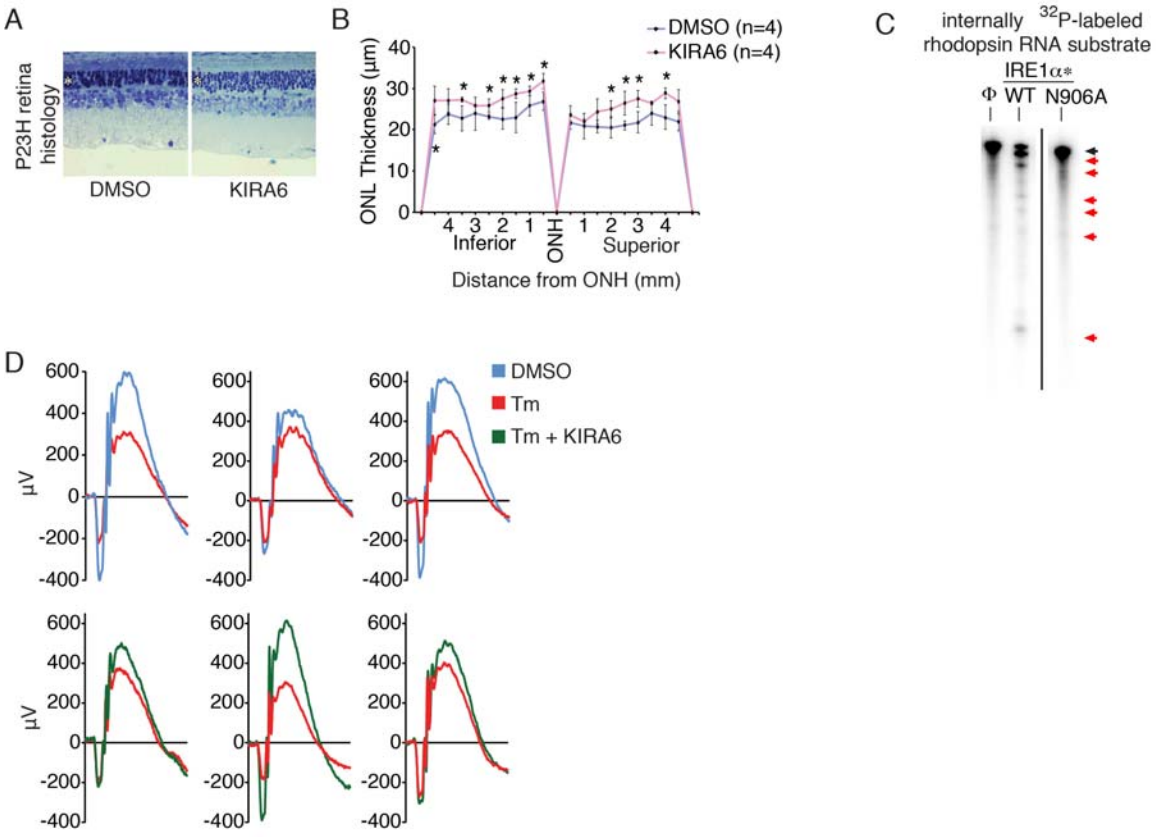

Figure 3.11. KIRA6 protects against cell degeneration and death in rodent model of ER stress-induced retinal degeneration.
(A-B) Histological sections of retinas from P23H rats (asterisks indicate outer nuclear layer (ONL)) and quantification of ONL thickness (n=4) of P23H and Sprague-Dawley (SD) rats. P23H rats were injected with 10 μM KIRA6 or DMSO at P9 and P15 and analyzed at P40. (C) Urea PAGE of cleavage reactions of ^{32}P-labeled Rhodopsin mRNA by IRE1α*(WT) or the RNase-dead mutant, IRE1α*(N906A), incubated with indicated doses of KIRA6. Black arrow indicates intact RNA and red arrows indicate cleavage products. (D) Representative ERG recordings of wild-type SD rats that were intravitreally injected with 2 μl Tm (n=10), Tm + KIRA6 (n=7) or an equivalent amount of DMSO (n=3) to achieve a final concentration of 3 μg/ml Tm and 10 μM KIRA6 in the vitreous at P21; ERG measurements at a light intensity of 0 dB were recorded at P28.

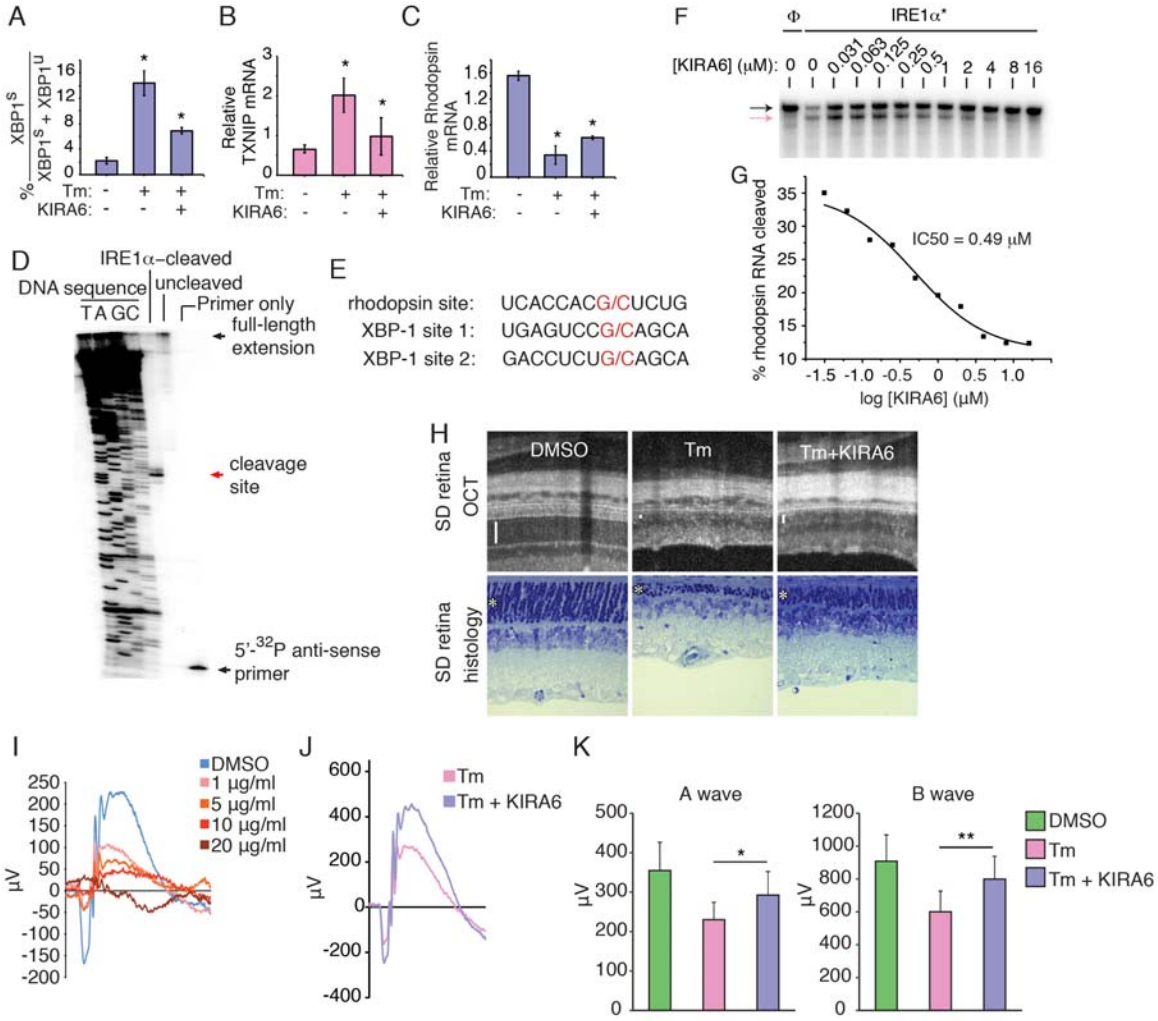

Figure 3.12. Intravitreal KIRA6 preserves photoreceptor cell numbers and function under ER stress.

(A) % XBP1 splicing in SD rat retinas 72hr post-intravitreal—and Q-PCR for TXNIP mRNA (B) and Rhodopsin mRNA (C) 96hr post-intravitreal—injection of 20 μg/ml Tm -/+ 10 μM KIRA6. (D) Primer extension mapping of IRE1α cleavage site in Rhodopsin RNA with alignment of Rhodopsin and XBP1 mRNA (E). Urea PAGE of cleavage of ^{32}P-labeled Rhodopsin mRNA by IRE1α* with indicated [KIRA6], with IC_{50} (F); black arrow: intact RNA; red arrow: cleaved RNA. (H) OCT images and histological sections of SD rats 7d post-intravitreal injection of 20 μg/ml Tm -/+ 10 μM KIRA6; bars and asterisks denote ONLs. (I) SD rats intravitreally injected at P21with 2 μl Tm or DMSO to achieve indicated [Tm]; ERG measurements at a light intensity of 0 dB recorded at P28. (J) Representative scotopic ERG at a light intensity of 0 dB from a SD rat treated with Tm (3μg/ml) +/- KIRA6 (10 μM) at P21 and analyzed at P28. (K) Quantified a- and b-wave amplitudes of 0 dB scotopic ERGs from SD rats treated with DMSO or Tm (3μg/ml) +/- KIRA6 (10 μM) at P21 and analyzed at P28.

(Figure 3.12I). Based on the results, we injected Tm at 3 μg/ml. In this regime, co-injection with KIRA6 substantially protects against loss of ERG responsiveness, significantly preserving both a- and b-wave amplitudes (Figure 3.12J,K, 3.11D).

Finally, to test *in vivo* efficacy of systemic KIRA6, we chose the *Ins2*$^{+/Akita}$ (Akita) mouse, which expresses a mutant (C96Y) proinsulin unable to complete oxidative folding, thus causing chronic ER stress, β-cell apoptosis, and diabetes in infancy [13]. Pharmacokinetic profile of KIRA6 in BALB/c mice intraperitoneally (i.p.) dosed at 10 mg/kg showed good drug plasma AUC levels (AUC 0-24h = 14.3 μM*h) with moderate clearance (22.4 mL/min/kg). Drug half-life was 3.90 hours, C_{max} was 3.3 μM, and plasma levels at 4 and 8hr were 1.2 μM and 0.33 μM, respectively. Initial systemic studies utilized a Tm i.p. challenge in C57BL/6 mice, with and without KIRA6 co-injection, and UPR markers measured in liver. Low dose Tm (2 μg/kg) elevates liver XBP1 splicing without decay of ER-localized Blos1 mRNA [11], while KIRA6 co-provision reduces XBP1 splicing (Figure 3.13A,B). Escalation of Tm to 100 □g/kg further increases XBP1 splicing and triggers Blos1 mRNA decay, with both markers attenuated by KIRA6 (Figure 3.13C,D).

Based on low micromolar KIRA6 needed for protection in cell culture, we chose i.p. dosing regimens of 5 or 10 mg/kg b.i.d for Akita chronic efficacy studies to provide similar exposure. We injected KIRA6 into randomized 3-week old male Akita mice when their random blood glucose levels were at prediabetic range (~200 mg/dl). In both dosing regimes, we observed significant amelioration

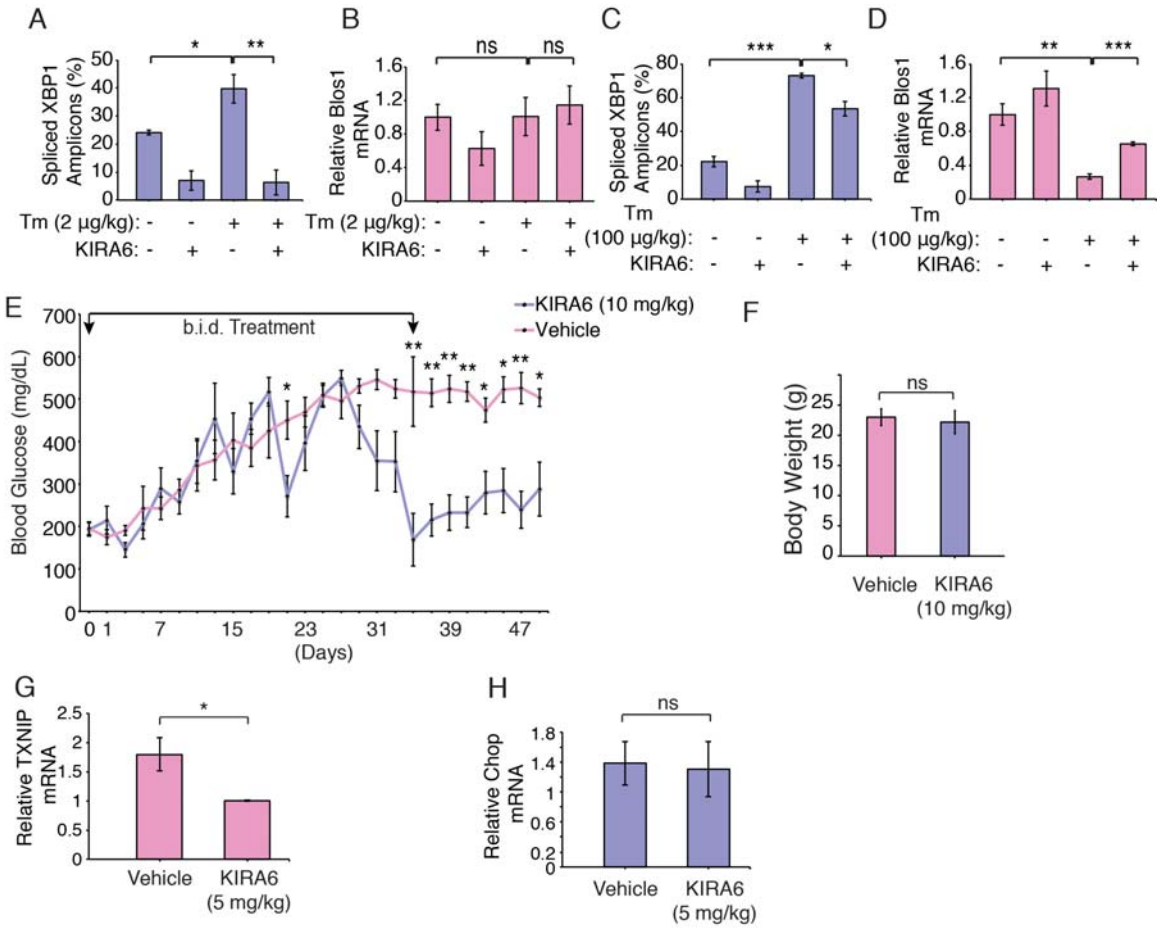

Figure 3.13. Systemic KIRA6 reduces Terminal UPR endpoints and protects against cell degeneration and death in the Akita diabetic mouse.
(A-D) XBP1 splicing (A,C) and Blos1 mRNA levels (B,D) were measured in livers of 8 week-old male C57BL/6 mice. Mice were injected with KIRA6 (25 mg/kg) intraperitoneally twice with an 8hr interval. After 4hr of first KIRA6 dose, the animals were injected with Tunicamycin (2 µg/kg) (A,B) or (100 µg/kg) (C,D). Animals were sacrificed 12hr after first KIRA6 injection and their livers were harvested for RNA collection. Averages from 3 biological replicates with *n* = 3. Data are plotted as mean +/- SEM. P-values: *<0.05, ** <0.01, ***<0.001. (E) Random blood glucose measurement of male *Ins2*$^{+/Akita}$ mice injected with either KIRA6 (10 mg/kg body weight)(n=4) or vehicle (n=6) b.i.d. starting at 3 weeks of age. Injections were stopped after 33 days. BGs (mean +/- SEM) also analyzed for significance by Two-way RM ANOVA; p-value = 0.0145. (F) Total body weight of the mice in (K) at day 49. Data are plotted as means +/- SD. p-values: *<0.05, ** <0.01. (G) TXNIP mRNA levels were measured in islets of male *Ins2*$^{+/Akita}$ mice injected with either KIRA6 (5 mg/kg body weight)(n=3) or vehicle (n=2) b.i.d. starting at 3 weeks age. Injections were continued for 7 days after which islets were harvested. (H) CHOP mRNA levels of the same samples as in (G). Data are plotted as means +/- SD. p-values: *<0.05.

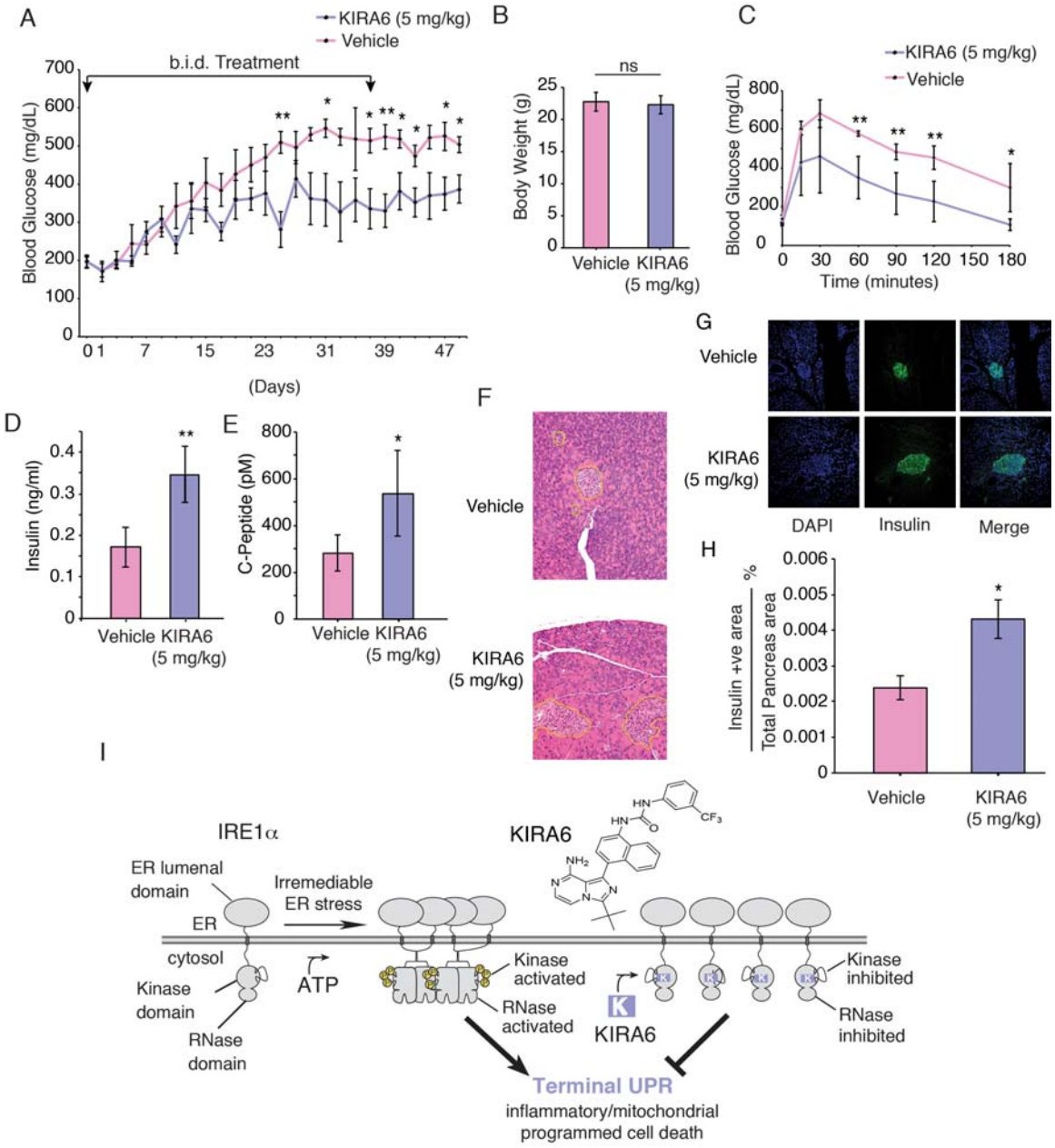

Figure 3.14. Systemic KIRA6 attenuates β-cell functional loss, increases insulin levels, and ameliorates hyperglycemia in the Akita mouse.
(A) Random AM blood glucose (BG) levels in male *Ins2*$^{+/Akita}$ mice intraperitoneally (i.p) injected for 37 days b.i.d. with KIRA6 (5 mg/kg)(n=6) or vehicle (n=6) starting at P21 (i.e., Day 1). BGs (mean +/- SEM), also analyzed by Two-way RM ANOVA; p-value = 0.0122. (B) Cohort body weights at Day 49. (C) Glucose tolerance tests on Day 49 (12d post injections) of O/N fasted *Ins2*$^{+/Akita}$ mice (P53) after i.p. (2 g/kg) glucose (KIRA6 n=6, Vehicle n=3). (D-E) Random insulin and C-peptide levels in *Ins2*$^{+/Akita}$ mice on Day 58 (21d post injections). KIRA6 (5 mg/kg)(n=5) and vehicle (n=4). (F) Whole pancreatic histological sections from *Ins2*$^{+/Akita}$ mice on Day 53 (15d post injections). Islets delineated by

dashed outline. Immunofluorescence micrographs of samples in (F): co-stained for DAPI (blue), insulin (green), with merge. (H) Total β-cell area as a percentage of total pancreas area on Day 55 (18d post injections). KIRA6 (5 mg/kg)(n=6) and vehicle (n=3). (I) Model of how KIRA6 prevents the terminal UPR by inhibiting IRE1α oligomers. Data plotted as mean +/- SD. P-values: *<0.05, ** <0.01.

of random glucose levels over several weeks in KIRA6-treated mice compared to vehicle, both fed ad lib (Figure 3.14A, 3.13E). TXNIP mRNA levels decline in islets of KIRA6-treated mice within one week, without compensatory increase of CHOP mRNA (downstream of PERK) (Figure 3.13G,H). KIRA6-treated mice appeared healthy even after 49 days from initial injection and displayed no significant differences in weight from vehicles (Figure 3.14B, 3.13F). Even 12 days after stopping injections, the 5mg/kg KIRA6-treated mice show significantly improved random blood glucose levels and glucose tolerance tests (GTT) (Figure 3.14C). Even 21 days after stopping injections, KIRA6-treated mice display statistically significant doubling in both plasma insulin and C-peptide levels (Figure 3.14D,E). H&E and insulin staining of whole pancreas sections reveals increased islet size in KIRA6 treated-animals (Figure 3.14F,G). Insulin-positive islet areas remained significantly higher in the KIRA6-treated group 18 days after stopping injections (Figure 3.14H).

DISCUSSION

In the baker's yeast *S. cerevisiae*, the UPR is a homeostatic signaling pathway controlled by IRE1-mediated splicing of an mRNA encoding an adaptive transcription factor called Hac1 [26]. Following this paradigm from this unicellular eukaryote, reports have suggested that the signaling outputs of mammalian

IRE1α are likewise solely restricted to restoring homeostasis and promoting survival under ER stress [27]. Furthermore, these models posit that when ER stress becomes irremediable, IRE1α's pro-survival signaling through XBP1 splicing circumstantially wanes (through an unknown mechanism), even as apoptotic outputs from PERK rise to promote cell death, without further opposition by IRE1α [28]. These arguments therefore predict that sustained IRE1α activation (even if artificially imposed) should universally promote cell survival under ER stress; whereas genetic or pharmacological inhibition of IRE1α should hasten cell death. Through forcibly activating and inhibiting IRE1α in a variety of cell systems and animal models, here we generated extensive data that refute these aforementioned predictions to instead support opposite conclusions.

An alternative model that we previously proposed [10], and mechanistically substantiated here, is that IRE1α switches outputs depending on the level of ER stress. Under low, manageable levels of ER stress, adaptive UPR signaling promotes secretory homeostasis, partly through IRE1α-mediated splicing of XBP1 mRNA and consequent XBP1s outputs. Likewise, pre-emptive PERK activation affords a measure of cytoprotection against subsequent ER stress by attenuating translation [29], as does pre-conditioning with 1NM-PP1-bound IRE1 α (I642G) to transiently stabilize an intermediate activation mode of the RNase confined to XBP1 splicing [16].

However, under high ER stress, IRE1α acquires endonucleolytic activity against a large plethora of RNA targets, first identified in *D. melanogaster* and

termed RIDD [30], including ER-localized mRNAs and non-coding RNAs in mammals [10-13]. These extra-XBP1 RNA cleavage events precede and closely track with entry of ER-stressed cells into apoptosis, and we showed here that their amelioration with small molecule inhibitors of IRE1α kinase/RNase inhibits apoptosis. Thus, rather than have the two UPR kinases working in opposition, multiple lines of evidence suggest that a continuum of graded activation states (dependent upon the strength of upstream stress) is available to either IRE1α or PERK, both of which under high activation undergo switch-like conversion from promoting homeostasis to promoting cell death [10, 28]. Similar switching mechanisms occur in other cell surface death receptors that respond divergently depending on the strength or context of upstream inputs [31, 32].

Further supporting a model of binary, rather than unitary outputs, three postulates that we posed and tested reasonably establish causality between IRE1α hyperactivation and cell death:

(I) First, forced hyperactivation of IRE1α's RNase should suffice to lead cells into the Terminal UPR and along a continuum of destructive outcomes, including proliferative blocks, loss of differentiated cell identity, and eventually into apoptosis. In line with this expectation, past a critical oligomerization threshold, IRE1α's RNase degrades key mediators of specialized cell function, including abundant insulin-encoding mRNAs in pancreatic β-cells and Rhodopsin mRNAs in retinal photoreceptor cells (both ER-localized). Also, as previously shown, mRNAs encoding ER-resident enzymatic activities are also targeted by hyperactive IRE1 α RNase, potentially compromising ER function [10]. Thus, at

high activation, IRE1α's adaptive outputs become overshadowed by its destructive outputs and further amplified downstream by TXNIP, causing IL-1β secretion, sterile inflammation/pyroptosis (linked to both types 1 and 2 diabetes) [13, 33] and JNK signaling [34]. Further linking IRE1α to cell death, IRE1α cancer mutants show defective homo-oligomerization and RNase activity, which may allow the Terminal UPR to become disabled or co-opted for survival advantage. Indeed, proliferative blocks normally imposed through IRE1α are defeated in the cancer mutants. Given these results, future studies of mutated IRE1α in cancer are warranted.

(II) Second, a class of IRE1α inhibitors that disrupt oligomerization should reduce RNase activity and Terminal UPR events in tandem. Unique among multi-domain kinases, the mechanistic relationship between IRE1α's kinase and RNase allows divergent small molecule allosteric control [19]. Whereas both are ATP-competitive, IRE1α type I kinase inhibitors increase oligomerization to increase RNase activity, while IRE1α type II kinase inhibitors decrease oligomerization to decrease RNase activity. Here we developed and tested the effects of KIRA6, a novel IRE1α type II kinase inhibitor. Given that KIRA6 has a favorable therapeutic index and shows IRE1α ON-target effects, we predicted that it would reduce cell death under ER stress. Remarkably, blocking IRE1α with KIRA6 raises the apoptotic threshold and enhances survival during ongoing upstream ER stress, indicating that destructive signaling rather than a compromised ER micro-environment *per se* promotes cell death (Figure 3.14I). While poly-pharmacological toxicity precluded testing ON-target effects of APY29,

our results justify development and testing of non-toxic type I kinase inhibitors against IRE1α cancer mutants.

(III) Third, blocking IRE1α with KIRA6 should protect against ER stress-mediated cell degeneration *in vivo*, leading not only to increased cell survival but also preserved physiological function. Consistent with this, in various cell types and explants, KIRA6 not only reduced cell loss under acute ER stress, but also prevented proliferative blocks and preserved function (e.g., GSIS). Encouraged by these data, we tested KIRA6 in rodent models of chronic ER stress-induced retinal degeneration. P23H rats intravitreally treated with KIRA6 had significantly preserved photoreceptor numbers, and in the Tm co-injection model, functional protection was found. Finally, systemic administration of KIRA6 in Akita diabetic mouse significantly reduced random blood glucose levels, improved glucose tolerance acutely, preserved β-cells, and elevated blood insulin and C-peptide levels. Remarkably, beneficial effects persisted even several weeks after stopping treatment. To our knowledge, this is the first work showing small molecule efficacy in the highly penetrant Akita genetic model.

Thus, we conclude that IRE1α exerts powerful effects on cell fate and function under ER stress, and that its kinase domain presents an attractive target for small molecule modulation. In summary, KIRA6, a novel small molecule kinase inhibitor of IRE1α, reduces cell death in several disease relevant models of ER stress-induced cell degeneration. While homozygous deletion of either *Ire1α* or *Xbp1* impedes embryogenesis and secretory cell development [34-37], the ability to titrate down IRE1α's catalytic activities with a small molecule

provides an opportunity to uncouple extra-XBP1 destructive outputs from XBP1-dependent adaptation. From this work, we propose the existence of a natural therapeutic window for IRE1α inhibition owing to the higher oligomeric state needed for extra-XBP1 endonucleolytic activation (RIDD); thus, lower concentrations of IRE1α type II kinase inhibitors block RIDD while maintaining XBP1 splicing (Figure 3.9D). Subsequent work is necessary to understand the consequences of long-term IRE1α inhibition. While further medicinal chemistry to optimize KIRA6 is beyond the scope of this study, such efforts may lead to first-in-class agents capable of preventing cell loss and affording therapeutic benefit in myriad human degenerative diseases, including retinitis pigmentosa and diabetes.

REFERENCES

1. Travers, K.J., Patil, C.K., Wodicka, L., Lockhart, D.J., Weissman, J.S., and Walter, P. (2000). Functional and genomic analyses reveal an essential coordination between the unfolded protein response and ER-associated degradation. Cell *101*, 249-258.
2. Harding, H.P., Novoa, I., Zhang, Y., Zeng, H., Wek, R., Schapira, M., and Ron, D. (2000). Regulated translation initiation controls stress-induced gene expression in mammalian cells. Molecular cell *6*, 1099-1108.
3. Shore, G.C., Papa, F.R., and Oakes, S.A. (2011). Signaling cell death from the endoplasmic reticulum stress response. Current opinion in cell biology *23*, 143-149.
4. Kohno, K. (2007). How transmembrane proteins sense endoplasmic reticulum stress. Antioxid Redox Signal *9*, 2295-2303.
5. Credle, J.J., Finer-Moore, J.S., Papa, F.R., Stroud, R.M., and Walter, P. (2005). On the mechanism of sensing unfolded protein in the endoplasmic reticulum. Proc Natl Acad Sci U S A *102*, 18773-18784.
6. Zhou, J., Liu, C.Y., Back, S.H., Clark, R.L., Peisach, D., Xu, Z., and Kaufman, R.J. (2006). The crystal structure of human IRE1 luminal domain reveals a conserved dimerization interface required for activation of the unfolded protein response. Proceedings of the National Academy of Sciences of the United States of America *103*, 14343-14348.

7. Calfon, M., Zeng, H., Urano, F., Till, J.H., Hubbard, S.R., Harding, H.P., Clark, S.G., and Ron, D. (2002). IRE1 couples endoplasmic reticulum load to secretory capacity by processing the XBP-1 mRNA. Nature *415*, 92-96.

8. Yoshida, H., Matsui, T., Yamamoto, A., Okada, T., and Mori, K. (2001). XBP1 mRNA is induced by ATF6 and spliced by IRE1 in response to ER stress to produce a highly active transcription factor. Cell *107*, 881-891.

9. Lee, A.H., Iwakoshi, N.N., and Glimcher, L.H. (2003). XBP-1 regulates a subset of endoplasmic reticulum resident chaperone genes in the unfolded protein response. Mol Cell Biol *23*, 7448-7459.

10. Han, D., Lerner, A.G., Vande Walle, L., Upton, J.P., Xu, W., Hagen, A., Backes, B.J., Oakes, S.A., and Papa, F.R. (2009). IRE1alpha kinase activation modes control alternate endoribonuclease outputs to determine divergent cell fates. Cell *138*, 562-575.

11. Hollien, J., Lin, J.H., Li, H., Stevens, N., Walter, P., and Weissman, J.S. (2009). Regulated Ire1-dependent decay of messenger RNAs in mammalian cells. The Journal of cell biology *186*, 323-331.

12. Upton, J.P., Wang, L., Han, D., Wang, E.S., Huskey, N.E., Lim, L., Truitt, M., McManus, M.T., Ruggero, D., Goga, A., et al. (2012). IRE1alpha cleaves select microRNAs during ER stress to derepress translation of proapoptotic Caspase-2. Science *338*, 818-822.

13. Lerner, A.G., Upton, J.P., Praveen, P.V., Ghosh, R., Nakagawa, Y., Igbaria, A., Shen, S., Nguyen, V., Backes, B.J., Heiman, M., et al. (2012). IRE1alpha induces thioredoxin-interacting protein to activate the NLRP3

inflammasome and promote programmed cell death under irremediable ER stress. Cell metabolism *16*, 250-264.

14. Korennykh, A.V., Egea, P.F., Korostelev, A.A., Finer-Moore, J., Zhang, C., Shokat, K.M., Stroud, R.M., and Walter, P. (2009). The unfolded protein response signals through high-order assembly of Ire1. Nature *457*, 687-693.

15. Ali, M.M., Bagratuni, T., Davenport, E.L., Nowak, P.R., Silva-Santisteban, M.C., Hardcastle, A., McAndrews, C., Rowlands, M.G., Morgan, G.J., Aherne, W., et al. (2011). Structure of the Ire1 autophosphorylation complex and implications for the unfolded protein response. EMBO J *30*, 894-905.

16. Han, D., Upton, J.P., Hagen, A., Callahan, J., Oakes, S.A., and Papa, F.R. (2008). A kinase inhibitor activates the IRE1alpha RNase to confer cytoprotection against ER stress. Biochemical and biophysical research communications *365*, 777-783.

17. Greenman, C., Stephens, P., Smith, R., Dalgliesh, G.L., Hunter, C., Bignell, G., Davies, H., Teague, J., Butler, A., Stevens, C., et al. (2007). Patterns of somatic mutation in human cancer genomes. Nature *446*, 153-158.

18. Xue, Z., He, Y., Ye, K., Gu, Z., Mao, Y., and Qi, L. (2011). A conserved structural determinant located at the interdomain region of mammalian inositol-requiring enzyme 1alpha. J Biol Chem *286*, 30859-30866.

19. Wang, L., Perera, B.G., Hari, S.B., Bhhatarai, B., Backes, B.J., Seeliger, M.A., Schurer, S.C., Oakes, S.A., Papa, F.R., and Maly, D.J. (2012). Divergent allosteric control of the IRE1alpha endoribonuclease using kinase inhibitors. Nature chemical biology *8*, 982-989.

20. Li, H., Korennykh, A.V., Behrman, S.L., and Walter, P. (2010). Mammalian endoplasmic reticulum stress sensor IRE1 signals by dynamic clustering. Proc Natl Acad Sci U S A *107*, 16113-16118.

21. Papandreou, I., Denko, N.C., Olson, M., Van Melckebeke, H., Lust, S., Tam, A., Solow-Cordero, D.E., Bouley, D.M., Offner, F., Niwa, M., et al. (2011). Identification of an Ire1alpha endonuclease specific inhibitor with cytotoxic activity against human multiple myeloma. Blood *117*, 1311-1314.

22. Zhang, S.X., Sanders, E., Fliesler, S.J., and Wang, J.J. (2014). Endoplasmic reticulum stress and the unfolded protein responses in retinal degeneration. Experimental eye research *125C*, 30-40.

23. Gorbatyuk, M.S., Knox, T., LaVail, M.M., Gorbatyuk, O.S., Noorwez, S.M., Hauswirth, W.W., Lin, J.H., Muzyczka, N., and Lewin, A.S. (2010). Restoration of visual function in P23H rhodopsin transgenic rats by gene delivery of BiP/Grp78. Proceedings of the National Academy of Sciences of the United States of America *107*, 5961-5966.

24. Pennesi, M.E., Nishikawa, S., Matthes, M.T., Yasumura, D., and LaVail, M.M. (2008). The relationship of photoreceptor degeneration to retinal vascular development and loss in mutant rhodopsin transgenic and RCS rats. Experimental eye research *87*, 561-570.

25. Shimazawa, M., Inokuchi, Y., Ito, Y., Murata, H., Aihara, M., Miura, M., Araie, M., and Hara, H. (2007). Involvement of ER stress in retinal cell death. Molecular vision *13*, 578-587.

26. Cox, J.S., and Walter, P. (1996). A novel mechanism for regulating activity of a transcription factor that controls the unfolded protein response. Cell *87*, 391-404.

27. Lin, J.H., Li, H., Yasumura, D., Cohen, H.R., Zhang, C., Panning, B., Shokat, K.M., Lavail, M.M., and Walter, P. (2007). IRE1 signaling affects cell fate during the unfolded protein response. Science *318*, 944-949.

28. Lin, J.H., Li, H., Zhang, Y., Ron, D., and Walter, P. (2009). Divergent effects of PERK and IRE1 signaling on cell viability. PloS one *4*, e4170.

29. Lu, P.D., Jousse, C., Marciniak, S.J., Zhang, Y., Novoa, I., Scheuner, D., Kaufman, R.J., Ron, D., and Harding, H.P. (2004). Cytoprotection by pre-emptive conditional phosphorylation of translation initiation factor 2. Embo J *23*, 169-179.

30. Hollien, J., and Weissman, J.S. (2006). Decay of endoplasmic reticulum-localized mRNAs during the unfolded protein response. Science *313*, 104-107.

31. Ofengeim, D., and Yuan, J. (2013). Regulation of RIP1 kinase signalling at the crossroads of inflammation and cell death. Nature reviews. Molecular cell biology *14*, 727-736.

32. Festjens, N., Vanden Berghe, T., Cornelis, S., and Vandenabeele, P. (2007). RIP1, a kinase on the crossroads of a cell's decision to live or die. Cell death and differentiation *14*, 400-410.

33. Schroder, K., Zhou, R., and Tschopp, J. (2010). The NLRP3 inflammasome: a sensor for metabolic danger? Science *327*, 296-300.

34. Urano, F., Wang, X., Bertolotti, A., Zhang, Y., Chung, P., Harding, H.P., and Ron, D. (2000). Coupling of stress in the ER to activation of JNK protein kinases by transmembrane protein kinase IRE1. Science *287*, 664-666.

35. Tirasophon, W., Welihinda, A.A., and Kaufman, R.J. (1998). A stress response pathway from the endoplasmic reticulum to the nucleus requires a novel bifunctional protein kinase/endoribonuclease (Ire1p) in mammalian cells. Genes & development *12*, 1812-1824.

36. Reimold, A.M., Iwakoshi, N.N., Manis, J., Vallabhajosyula, P., Szomolanyi-Tsuda, E., Gravallese, E.M., Friend, D., Grusby, M.J., Alt, F., and Glimcher, L.H. (2001). Plasma cell differentiation requires the transcription factor XBP-1. Nature *412*, 300-307.

37. Zhang, K., Wong, H.N., Song, B., Miller, C.N., Scheuner, D., and Kaufman, R.J. (2005). The unfolded protein response sensor IRE1alpha is required at 2 distinct steps in B cell lymphopoiesis. J Clin Invest *115*, 268-281.

CHAPTER 4

Materials and Methods

Chapter 2: *FAS-activated mitochondrial apoptosis culls stalled embryonic stem cells to promote differentiation*

ESC Cultures

Mouse ESC lines were maintained in ESC Media: DMEM containing high glucose (Sigma #D7777; pH 7.3, 285-290 mOsm/kg) with HEPES hemisodium salt (MP Biomedical), 15% ESC-qualified fetal bovine serum (Gibco #10439024), 1% L-glutamine (UCSF Cell Culture Facility #CCFGB002), 1% non-essential amino acids (UCSF Cell Culture Facility #CCFGA001), 100 mM β-mercaptoethanol (Gibco #21985-023), and LIF (made in-house). Cells were maintained on irradiated mouse embryonic fibroblasts (MEFs). For differentiation experiments, ESCs were first plated away from MEFs onto gelatinized dishes (0.2% gelatin from porcine skin, Sigma #G2500) and then treated with 1 μM retinoic acid (Sigma #R2625) in ESC media without LIF for the indicated time points. *Casp3*$^{-/-}$ ESCs were a generous gift from T. Zwaka (Mt. Sinai). Embryoid bodies were formed using the hanging drop method, with 400 cells plated in 20 μl drops of ESC media without LIF.

Generation of Bax$^{-/-}$Bak$^{-/-}$ ESCs

ESCs were obtained from timed matings of *Bax*$^{f/f}$*Bak*$^{-/-}$ animals. *Bax*^{flox} [1] and *Bak*$^{-/-}$ [2] mice were backcrossed to C57BL/6J background for 6 generations before breeding together. Blastocysts were harvested at E3.5, plated on irradiated MEFs, trypsinized

and allowed to grow until confluency. Three independent lines were obtained and transfected with pCre-pac. Cells were selected with puromycin at 2 μg/ml for 1 week until visible colonies formed. Four independent clones were screened for *Bax* mRNA and protein levels, and genotyped for *Cre* recombinase.

Quantitative RT-PCR

Total RNA was extracted from ESCs using Trizol (Invitrogen) or RNeasy Mini Kit (Qiagen) (for Bax transcript levels). cDNA was generated using the SuperScript II Reverse Transcriptase Kit (Invitrogen). Quantitative PCR was performed using Power SYBR Green PCR Master Mix (Applied Biosystems). *Bax* transcript levels were normalized to hypoxanthine phosphoribosyltransferase (*HPRT*), while other targets were normalized to 60S ribosomal protein-7 (*RPL7*). Samples were run in triplicate. Primer sequences are listed below.

Oligonucleotides Used for Quantitative RT-PCR.

	Forward Primer (5' – 3')	**Reverse Primer (5' – 3')**
Cre	CTGCATTACCGGTCGATGCAA	TGCTAACCAGCGTTTTCGTTCTGCC
Bax	GCTGACATGTTTGCTGATGG	GATCAGCTCGGGCACTTTAG
Oct4	AAAGCCCTGCAGAAGGAGCTAGAA	AACACCTTTCCAAAGAGAACGCCC
Nanog	AAAGCCCTGCAGAAGGAGCTAGAA	TCCAGATGCGTTCACCAGATAG
RPL7	GATTGTGGAGCCATACATTGCA	TGCCGTAGCCTCGCTTGT
Actin	CACAGCTTCTTTGCAGCTCCT	CGTCATCCATGGCGAACTG
Fas#1	TGAATGGGGGTACACCAACC	TTCCATGTTCACACGAGGCG

Fas#2	AGATGCACACTCTGCGATGA	AGGCGATTTCTGGGACTTTGT
FasL#1	GAACTGGCAGAACTCCGTGA	TGAGTGGGGGTTCCCTGTTA
FasL#2	GGCTCTGGTTGGAATGGGAT	GGTGTACTGGGGTTGGCTATT
p53#1	CGAAGACTGGATGACTGCCA	CGTCCATGCAGTGAGGTGAT
p53#2	TGCTCACCCTGGCTAAAGTT	TCCGACTGTGACTCCTCCAT
AurA#1	TGGATGCTGCAAACGGATAG	TGAGACGGAATCTGCTCAGTC
AurA#2	ACTCTCCAAGTTTGACGAGCA	ACACATTGTGGTTCTCCTGGAAG

Flow Cytometry and Antibodies

Cells were harvested, washed in PBS twice, and incubated with AnnexinV-FITC (Biovision) or AnnexinV-APC (BD Pharmingen). Surface expression of FAS was measured using anti-mouse CD95-PE (clone 15A7, eBioscience) or a matched IgG1-PE isotype control (eBioscience); for analysis of FAS, cells were collected in citric saline (135mM potassium chloride, 15mM sodium citrate) with 1mM EDTA to avoid enzymatic digest of cell surface proteins. Propidium iodide (Biovision) or 4',6-diamidino-2-phenylindole (DAPI; Invitrogen) was added to cells immediately before flow cytometry analysis.

Western Blots and Antibodies

Cells were lysed in RIPA buffer (20 mM Tris-MOPS [pH 7.4], 150 mM NaCl, 1mM EDTA, 1 mM EGTA, 1% NP-40) containing protease inhibitor cocktail (Thermo Scientific), sonicated and centrifuged at 13,000 rpm for 5 minutes at 4ºC. Protein concentration was measured using a BCA assay (Pierce). Equivalent amounts of each

sample were loaded on 10% Bis-Tris gels (Invitrogen), transferred to PVDF membranes, and immunoblotted with antibodies against BAX, Nanog, phosphor-Ser15-p53, total p53, γ-H2AX, cJun, CASP3, CASP8, and cleaved CASP8 (all Cell Signaling Technology); FAS (M-20), FAS-L (N-20), and Oct4 (all Santa Cruz Biotechnology); BID (R&D Biosystems #AF860); AurA (BD Biosciences), and Actin (Sigma). Horseradish peroxidase-conjugated secondary antibodies were purchased from Jackson ImmunoResearch. Membranes were developed with SuperSignal West Chemiluminescent Substrate (Thermo Scientific).

Alkaline Phosphatase Staining

Untreated or RA treated ESCs were plated onto irradiated MEFs in a 6-well plate at 2000 cells/well and allowed to grow for a week or until visible colonies formed. Cells were washed with PBS, fixed, and stained for alkaline phosphatase using the Vector Red Alkaline Phosphatase Substrate Kit I (Vector Laboratories).

Teratoma Formation

One million wildtype (*Bax*$^{+/+}$*Bak*$^{+/+}$), parental (*Bax*$^{f/f}$ *Bak*$^{-/-}$), DKO (*Bax*$^{-/-}$*Bak*$^{-/-}$), or *Casp3*$^{-/-}$ ESCs were injected subcutaneously into nude mice. Tumors that formed were isolated, sectioned, and stained with hematoxylin and eosin or anti-Oct4 (H-134; Santa Cruz Biotechnology #9081).

siRNA Knockdown

ESCs were plated away from MEFs the day before transfection with Dharmafect1

(Dharmacon) and 50 nM siRNA. 24 hrs after transfection, the cells were treated with RA. siRNAs were purchased from Thermo Fisher Scientific against *Casp8* (D0-43044-02 and -03), *Fas* (D-045283-19 and -20), and *AurA* (D-065109-01 and -03); a non-targeting siRNA (D-001210-05) was used as a control.

Immunofluorescence

ESCs were left in undifferentiated conditions or treated with RA for 4 days. Subsequently, they were collected and spun onto frosted glass slides (Fisher) using a Cytospin 4 (Thermo Scientific). Cells were fixed with 4% paraformaldehyde, permeabilized with 0.5% Trixon-X, and stained with anti-γ-H2AX (Cell Signaling). γ-H2AX positive nuclei were quantified using Metamorph (Molecular Device Inc.). Results shown are mean +/- SD from five independent samples.

Chapter 3: *Allosteric inhibition of the IRE1α RNase preserves cell viability and function during endoplasmic reticulum stress*

Tissue Culture

INS-1 cells with doxycycline (Dox)-inducible expression of wild-type and mutant mouse IRE1α were grown in RPMI, 10% fetal bovine serum, 1 mM sodium pyruvate, 10 mM HEPES, 2 mM glutamine, 50 μM β-mercaptoethanol, as described previously (Han *et al*., 2009). To generate the Dox-inducible IRE1α human (WT) and IRE1α human cancer mutant cell lines, INS-1/FRT/TO cells were grown in the above media with 10 μg/ml blasticidin. Cells were then grown in 200 μg/ml zeocin, cotransfected with 1 μg pcDNA5/FRT/TO:IRE1α human (WT), (L474R), (R635W), (S769F), (Q780*) and (P830L) mutant constructs and 1 μg FLP recombinase (pOG44) using Lipofectamine (Invitrogen). After 4hr, cells were switched to zeocin-free media, trypsinized 48hr later, and then plated in media containing hygromycin (150 μg/ml), which was replaced every 3 days until colonies appeared. Thapsigargin (Tg), Brefeldin A (BFA), and Dox were purchased from Sigma-Aldrich. Tunicamycin (Tm) was purchased from Millipore. APY29, KIRA6, 1NM-PP1 and (NMe)KIRA6 were synthesized in house.

Western Blots and Antibodies

For protein analysis, cells were lysed in M-PER buffer (Thermo Scientific) plus complete EDTA-free protease inhibitor (Roche) and phosphatase inhibitor cocktail (Sigma). The concentration of samples was determined using BCA Protein Assay (Thermo). Western blots were performed using 10% and 12% Bis-Tris precast gels (NuPage) on Invitrogen

XCell SureLock® Mini-Cell modules. Gels were run using MES buffer and transferred onto nitrocellulose transfer membrane using an XCell II™ Blot Module. Blocking, antibody incubation, and washing were done in PBS or TBS with 0.05% Tween-20 (v/v) and 5% (w/v) non-fat dry milk or BSA, or blocking buffer (Licor-Odyssey). Antibodies used were: mouse anti-Actin (Sigma-Aldrich); rabbit anti-cleaved Caspase-2 (Abcam); mouse anti-GAPDH, anti-c-Myc, anti-rabbit, anti-proinsulin, and anti-IRE1α (Santa Cruz Biotechnology); anti-phospho-IRE1α and anti-full length Caspase-2 (Novus Biologicals); and rabbit anti-Caspase-3, anti-JNK, anti-eIF2α, anti-phospho-eIF2α, and mouse anti-phospho-JNK (Cell Signaling). Antibody binding was detected by using near-infrared-dye-conjugated secondary antibodies (Licor) on the LI-COR Odyssey scanner or visualized by capturing on a CL-XPosure film using ECL SuperSignal West Dura Extended Duration Substrate (both from Thermo Scientific).

RNA isolation, Real-Time PCR (Q-PCR), and Primers

RNA was isolated from whole cells using either Qiagen RNeasy kits or Trizol (Invitrogen). TissueLyser II (Qiagen) was used for RNA isolation from liver and retina. Primers used for Q-PCR were as follows: Rat TXNIP: 5'-CTGATGGAGGCACAGTGAGA-3' and 5'-CTCGGGTGGAGTGCTTAGAG-3'; rat GAPDH 5'-AGTTCAACGGCACAGTCAAG-3' and 5'-ACTCAGCACCAGCATCACC-3'; rat Ins1, 5'-GTCCTCTGGGAGCCCAAG-3' and 5'-ACAGAGCCTCCACCAGG-3'; rat Ins2, 5'-ATCCTCTGGGAGCCCCGC-3' and 5'-AGAGAGCTTCCACCAAG-3'; rat p21, 5'-TGAACCGCTGTCTTGAGATG-3' and 5'-TCTTGGTTGCCTCTTTTGCT-3'; mouse Blos1, 5'-CAAGGAGCTGCAGGAGAAGA-3' and 5'-GCCTGGTTGAAGTTCTCCAC-3';

mouse Beta-Actin, 5'-GCAAGTGCTTCTAGGCGGAC-3' and 5'-AAGAAAGGGTGTAAAACGCAGC-3'.For standard mRNA, 1 µg total RNA was reverse transcribed using the QuantiTect Reverse Transcription Kit (Qiagen). For Q-PCR, we used SYBR green (Qiagen) and StepOnePlus Real-Time PCR System (Applied Biosystems). Thermal cycles were: 5 min at 95 °C, 40 cycles of 15 s at 95 °C, 30 s at 60 °C. Gene expression levels were normalized to GAPDH or Actin.

For TaqMan Q-PCR, cDNA was produced using a target-specific probe, TaqMan Universal PCR Master Mix, the TaqMan microRNA reverse transcription kit (both Applied Biosystems) and the Bio-Rad iCycler Thermal cycler. For both regular Q-PCR and TaqMan Q-PCR, the reactions were performed on C1000 thermal cycler and measurements were recorded on a CFX96 Real-Time PCR Detection System (both from Bio-Rad). The following targeted primers and probes sets were used in TaqMan Q-PCR: snoRNA135, RPL21 and hsa-miR-17 (all from Applied Biosystems).

XBP-1 mRNA splicing

RNA was isolated from whole cells or tissues and reverse transcribed as above to obtain total cDNA. Then, XBP-1 primers were used to amplify an XBP-1 amplicon spanning the 26 nt intron from the cDNA samples in a regular 3-step PCR. Thermal cycles were: 5 min at 95 °C, 30 cycles of 30 s at 95 °C, 30 s at 60 °C, and 1 min at 72 °C, followed by 72 °C for 15 min, and a 4 °C hold. Sense primer rat XBP1.3S (5'-AAACAGAGTAGCACAGACTGC-3') and antisense primer rat XBP1.2AS (5'-GGATCTCTAAGACTAGAGGCTTGGTG-3') were used. PCR fragments were then digested by PstI, resolved on 2% agarose gels, stained with EtBr and quantified by

densitometry using ImageJ (U. S. National Institutes of Health). Spliced XBP1 was also determined in mouse liver by Q-PCR using mouse XBP1 sense (5'-AGGAAACTGAAAAACAGAGTAGCAGC-3') and antisense (5'-TCCTTCTGGGTAGACCTCTGG-3') primers.

Flow Cytometry

For assaying apoptosis by Annexin V staining, cells were plated in 12-well plates overnight. Cells were then treated with various reagents for indicated time periods. On the day of flow cytometry analysis, cells were trypsinized and washed in PBS and resuspended in Annexin V binding buffer with Annexin-V FITC (BD Pharmingen™). Flow cytometry was performed on a Becton Dickinson LSRII flow cytometer.

Islet staining

Islets were extracted from C57BL/6 mice using previously reported methods [3], and cultured in RPMI + 10% FBS with 0.5 μg/mL Tm with or without KIRA6 (0.5 μM) or left untreated for 16hr. Approximately 150 islets were cultured for each condition in triplicate. Non-diabetic human islets were obtained from Prodo Labs (Irvine, CA) and cultured in Prodo Islet Medium (PIM from Prodo Labs). For analysis of non-ER stress treated conditions, islets were cultured in PIM for 16hr before harvesting. Islets were then spun, washed once with PBS, and fixed for 30 min with 4% PFA. After fixation, islets were washed twice with PBS, followed by a wash in 100% ethanol. After removal of all ethanol, 100 μl of prewarmed Histogel (Thermo Scientific) was added to the eppendorf tube and placed at 4°C to solidify before paraffin embedding and 5 μm

sectioning of the islets. Islets were stained with TUNEL using ApopTag® Red In Situ Apoptosis Detection Kit (Millipore) according to the manufacturer's instructions. Islets were also co-stained with anti-TXNIP (MBL International), guinea pig anti-insulin (Zymed), DAPI (Sigma), and goat anti-guinea pig secondary (Rockland) before mounting onto slides with VectaShield (Vector Laboratories). At least 10 islets and > 500 β-cell nuclei were counted per group, in triplicate. Cells were considered TUNEL positive if staining was present and colocalized with DAPI staining, indicating nuclear localization.

MTT assay

INS-1 CAT, IRE1α human (WT) and IRE1α human mutant cells were seeded at 40% confluence in a 96-well plate and treated or not treated with indicated concentrations of Tg or Dox (1 μg/ml). At the indicated time points, medium was replaced with 100 μl of 1 mg/ml 3-(4,5-dimethylthiazol-2-yl)-2.5-diphenyltetrazolium bromide (MTT) (Molecular Probes) in RPMI. After incubation at 37°C for 4hr, 75 μl MTT medium was removed, and 50 μl DMSO were added to dissolve precipitate. Absorbance was recorded at 540 nm using a Spectramax M5 microplate reader (Molecular Devices).

Superfolder GFP-IRE1α construction and microscopy

The first 27 amino acids of mouse IRE1α containing the signal peptide were cloned just before the first ATG of sfGFP lacking the stop codon, and the rest of the sequence of mouse IRE1α (WT) or IRE1α (I642G) was cloned in frame after the sfGFP in a pCDNA5 FRT/TO mammalian expression plasmid. INS1- FRT/TO cells were transfected as

described previously (Han *et al*., 2009) to generate stable cell lines expressing the above constructs, as well as the previously described reporter, IRE1-3F6HGFP that contains an EGFP domain positioned close to the kinase [4]. After induction of INS1-sfGFP-IRE1α cells for 24hr with 1 ng/ml Dox (a sub-apoptotic dose sufficient for imaging the reporter), live cells were imaged on a widefield microscope after a further treatment with 1 mM DTT in the presence or absence of 1 μM KIRA6 (Axiovert 200; Carl Zeiss MicroImaging, Inc.) with a 63X/1.4 NA oil objective and a 450-490nm excitation/500-550 emission bandpass filter using a Retiga 2000R camera. Composite figures were prepared using ImageJ (NIH), Photoshop CS4 and Illustrator CS4 software (Adobe). For INS1-sfGFP-IRE1α (I642G) cells, 5 μM 1NM-PP1 was used for induction in presence of 1 ng/ml Dox for 12hr. Live cells were imaged (Nikon Eclipse Ti-Yokogawa CSU22 spinning disk confocal) with Apo 100X/1.49 oil objective and a 491nm excitation/525-50 emission filter. Figures were prepared using ImageJ (NIH).

Null Hong Kong α-1 Antitrypsin De-glycosylation immunoblots

pCDNA3.1-α1 hAT-NHK plasmid expressing the NHK-α1AT, a kind gift of Rick Siefers (Baylor College of Medicine) was transfected into HEK293 cells. Cells were then treated with Tm +/- KIRA6 to check protein glycosylation status. NHK-α1AT remains glycosylated under normal conditions producing a protein band at ~ 50 kDa by immunoblot. However, Tm treatment inhibits glycosylation and the deglycosylated band appears at ~ 42 kDa. Goat anti-human α1-antitrypsin antibody (MP biomedicals) was used for detection by immunoblot.

Detection of IL1-β

Human THP-1 cells were grown in RPMI-1640 with 10% FBS and 50 μM 2-mercaptoethanol, differentiated for 2hr with 0.5 μM phorbol-12-myristate-13-acetate (Sigma), and primed for 18hr with 1 μg/ml ultrapure lipopolysaccharide (LPS; Sigma). Cell culture media was changed to media without LPS and treated with 0.5 μM KIRA6 for 2hr prior to the addition of 5 mM ATP (Roche), or 1 μM Tg or 10 μg/ml Tm. After 4hr incubation, media supernatant was collected and assayed for hIL-1β by ELISA (Thermo Scientific).

TXNIP 3'UTR Reporter Luciferase Assay

Luciferase reporter containing TXNIP 3' UTR with miR-17 binding sites was used as described [5]. To measure luciferase activity a Dual-Glo (Promega #E2920) kit was used as per manufacturer's instructions. The luciferase enzyme activity was detected on a Spectramax M5 microplate reader (Molecular Devices).

Glucose-stimulated insulin secretion (GSIS) assay

Freshly isolated islets from 9-week-old C57BL/6 mice were cultured in RPMI-1640 with 10% FCS, 2 mM L-glutamine, 0.1 mM 2-mercaptoethanol, and 11 mM glucose with or without Tm (500 ng/ml) for 16hr before the GSIS assay. KIRA6 (0.5 μM) was added 2hr before treating with Tm. In the GSIS assay, islets were preincubated in HEPES-buffered Krebs-Ringer bicarbonate solution (KRBH) (10 mM HEPES [pH 7.4], 129 mM NaCl, 4.7 mM KCl, 1.2 mM KH_2PO_4, 1.2 mM $MgSO_4$, 2 mM $CaCl_2$, 5 mM $NaHCO_3$, and 0.1% BSA) containing 2.5 mM glucose for 30 min at 37°C. Thirty islets per condition were

incubated with either 2.5 mM or 16.7 mM glucose in KRBH at 37°C for 60 min. Collected media were analyzed by anti-insulin ELISA (EMD Millipore).

Intravitreal Injections of small molecules

2 µl was injected intravitreally into each eye to achieve the indicated final concentrations based on known rat vitreous volumes. Tm (20 µg/µl final concentration) +/- KIRA6 (10 µM final concentration) was injected into SD rats at P21 with an equivalent amount of DMSO as a vehicle control. Retinas were collected at 72 and 96hr after injections in Trizol (Invitrogen) for Q-PCR analysis. Eyes were examined by optical coherence tomography (OCT) 7 days post injection and subsequently collected for morphological analysis. P23H rats were injected with KIRA6 (10 µM final concentration) or DMSO vehicle control at P9 and P15, and eyes were examined at P40 by OCT and by morphological analysis.

Image guided optical coherence tomography (OCT)

Mice were anaesthetized with 1.5-3% isoflurane, eyes were dilated with 2.5% phenylephrine hydrochloride and 1% tropicamide, and corneas were kept moist with regular application of 2.5% methylcellulose. Eyes were examined using a Micron III retinal imaging system (Phoenix Research Labs). Spectral domain OCT images were acquired with a Micron Image Guided OCT System (Phoenix Research Labs) by averaging 10 to 50 scans.

Morphological analysis of retinas

Outer nuclear layers (ONL) were quantified as previously described [6]. Briefly, rats were euthanized by CO_2 inhalation and their eyes were immediately enucleated and immersed in 2% paraformaldehyde and 2.5% glutaraldehyde in phosphate buffered saline. Subsequently, eyes were bisected on the vertical meridian through the optic nerve head and embedded in Epon-Araldite resin; 1 μm sections were cut and stained with toluidine blue. ONL thickness was measured at 54 locations around the retina using Bioquant image analysis (Bioquant; R&M Biometrics).

Electroretinography (ERG)

Rats dark-adapted overnight were anesthetized with ketamine (87 mg/kg) and xylazine (13 mg/kg) via i.p. injection in dim red light. Pupils were dilated with 2.5% phenylephrine hydrochloride and 1.0% tropicamide, and corneas were anesthetized with 0.5% proparacaine. Scotopic ERG recordings were performed as previously described [7]. Briefly, 10-μsec flashes of white light of increasing intensities were used to induce bilateral, full-field ERGs; responses were recorded using contact lens electrodes with a UTAS-E 3000 Visual Electrodiagnostic System (LKC Technologies, Inc.).

Electroretinography (ERG)

Islet culture and proliferation assessment (EdU staining)

C57BL/6 mouse islets were isolated as previously described [3], cultured for 5 days, followed by 2 days of indicated treatment. DMSO was utilized as control, Tm at 0.5 μg/ml, and KIRA6 at 1 μM. After 48hr, islets were treated with 10 mM 5-Ethynyl-2-deoxyuridine (EdU) for 3hr, and then immediately fixed in 4% paraformaldehyde/10 mM

PBS solution for 25 min. Islets were washed 3 times with 10 mM PBS for 20 min, permeabilized with 0.3% TritonX-100 in 10 mM PBS for 3hr, then blocked in 5% goat serum/0.15% Triton-X 100/10 mM PBS overnight at 4°C and washed twice with antibody dilution buffer for 15 min at room temperature. Primary antibody, rabbit anti-human NKX6.1 1:500 (Sigma-Aldrich), and secondary antibody, Cy3 conjugated goat anti-rabbit 1:500 (Sigma), were diluted in 1% BSA/0.2% Triton X-100/10 mM PBS and incubated for 24hr at 4°C. Click-iT® EdU Alexa Fluor® Imaging Kit (Invitrogen) was used to identify dividing cells after immunostaining. Islets were mounted with Fluoromount™ (Sigma) and imaged using a Leica SP5 confocal laser scanning microscope (Leica). The Volocity software (PerkinElmer) colocalization macro was utilized to quantify dual EdU and the unique β-cell nuclear marker Nkx6.1.

Animal analytic studies

C567BL/6 and C57BL/6 Ins2 $^{WT/C96Y}$ (*Ins2*$^{+/Akita}$) mice were obtained from Jackson Laboratories. Glucose levels were measured from tail snips obtained between 9:00 and 11:00 AM using a glucometer (Nova Statstrip Xpress, Data Sciences International). Serum insulin and C-peptide levels were measured using mouse ultra-sensitive insulin and C-peptide ELISA (Mercodia). All procedures described involving animals were performed in accordance with protocols approved by the Institutional Animal Care and Use Committee at the University of California, San Francisco. Animals were maintained in a specific pathogen-free animal facility on a 12hr light–dark cycle at an ambient temperature of 21°C. They were given free access to water and food. All experiments used age-matched male mice.

Ins2$^{+/Akita}$ mouse genotyping

Akita mouse colonies were maintained and genotyped as described previously [5].

Glucose Tolerance Test

Mice were fasted for 17hr before i.p. injection with glucose (2 g/kg). Blood was collected from the tail, and glucose levels were determined using a glucometer (Nova Statstrip Xpress, Data Sciences International).

Mouse injections

Male *Ins2*$^{+/Akita}$ mice were injected i.p. with KIRA6 in a 2 mg/ml solution made of 3% Ethanol: 7% Tween-80: 90% Saline twice a day (b.i.d). Same solution without KIRA6 is denoted as Vehicle. C567BL/6 mice were also injected with same KIRA6 solution and indicated doses of Tm for liver analysis.

Pancreatic Insulin-positiveβ-cell area determination

Pancreatic sectioning, staining and analysis were done as described previously [8]. Briefly, whole pancreas in paraffin-embedded blocks from vehicle (n=3) and KIRA6 (n=6) treated mice were serially sectioned at intervals of 250 μm. Every 10th section was stained with anti-insulin (Invitrogen). Nuclei were stained with DAPI (Sigma-Aldrich). A minimum of 2% of the total organ volume was stained and measured. The pancreas and β-cell areas were measured with the Zeiss AxioImager Brightfield Microscope and quantified with VOLOCITY software.

Rat husbandry

All studies and procedures were performed in accordance with the guidelines of the Institutional Animal Care and Use Committee at the University of California, San Francisco, and in compliance with the ARVO Statement for the Use of Animals in Ophthalmic and Vision Research. P23H rhodopsin transgenic rats (line 1) were described previously (http://www.ucsfeye.net/mlavailRDratmodels.shtml); wild-type Sprague-Dawley (SD) rats served as controls. All animals were housed in barrier facility free of specific pathogens on a 12hr light/dark cycle with food and water available *ad libitum*.

KIRA6 and KIRA6_NMe synthesis

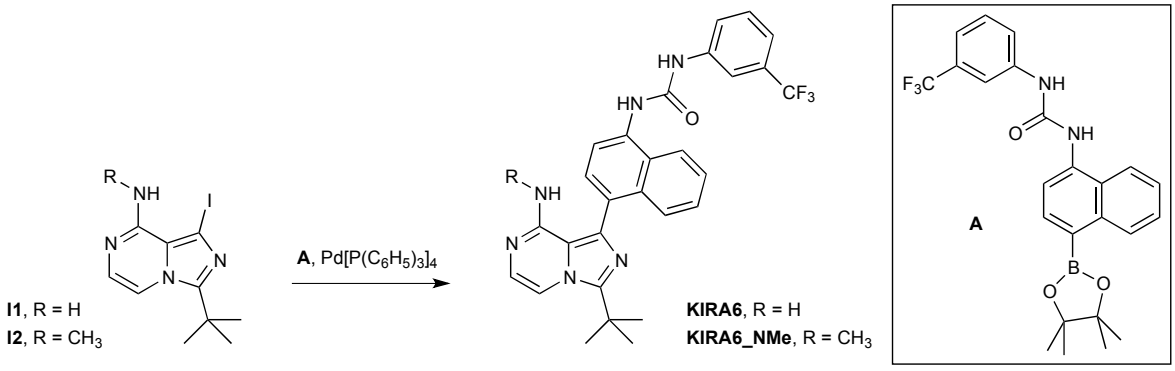

I1, R = H
I2, R = CH_3

KIRA6, R = H
KIRA6_NMe, R = CH_3

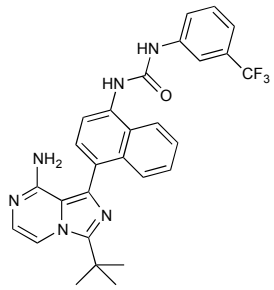

KIRA6

1-(4-(8-amino-3-tert-butylimidazo[1,5-a]pyrazin-1-yl)naphthalen-1-yl)-3-(3-(trifluoromethyl)phenyl)urea (KIRA6). A mixture of **I1** (60.0 mg, 0.120 mmol), **A** (66 mg, 0.15 mmol), tetrakis(triphenylphosphine)palladium (5 mg, 4 µmol) and sodium carbonate (928 mg, 0.27 mmol) was dissolved in a 3:1 mixture of DME/water (0.5 ml). The mixture was heated overnight at 85°C. The crude mixture was cooled to room temperature, diluted in a mixture of acetonitrile/water and purified by reverse phase chromatography (HPLC) to obtain 53 mg of KIRA6. TLC (CH_2Cl_2:MeOH, 95:5 v/v): R_f = 0.4; ^{1}H NMR (300 MHz, MeOD): δ 8.26 (m, 1H), 8.08-7.99 (m, 2H), 7.90-7.86 (m, 1H), 7.83-7.79 (m, 1H), 7.69- 7.52 (m, 5H), 7.35 (d, *J* = 7.4 Hz, 1H), 6.98 (m, 1H), 1.65 (s, 9H); ^{13}C NMR (126 MHz, MeOD): δ 154.8, 140.2, 135.7, 133.0, 132.4, 131.7, 131.6, 131.0, 130.7, 129.4, 128.8, 128.6, 128.5, 127.0, 126.6, 125.9, 125.4, 123.2, 121.9, 120.1, 118.7, 115.0, 114.4, 110.1, 33.6, 27.3; ESI-MS (m/z): [M]+ calcd. for $C_{28}H_{25}F_3N_6O$ ($M+H^+$): 519.2; found 519.4.

The purity of KIRA6 was determined with two analytical RP-HPLC methods, using a Varian Microsorb-MV 100-5 C18 column (4.6 mm x 150 mm), and eluted with either H_2O/CH_3CN or H_2O/ MeOH gradient solvent systems (+0.05% TFA) run over 30 min. Products were detected by UV at 254 nm. KIRA6 was found to be >95% pure in both

solvent systems.

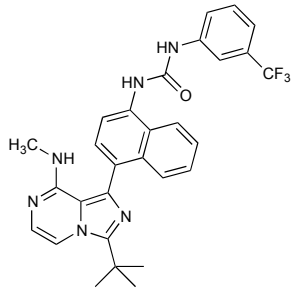

(NMe)KIRA6

1-(4-(8-methylamino-3-tert-butylimidazo[1,5-a]pyrazin-1-yl)naphthalen-1-yl)-3-(3-(trifluoromethyl)phenyl)urea ((NMe)KIRA6). A mixture of **I2** (14.6 mg, 0.044 mmol), **A** (22 mg, 0.048 mmol), tetrakis(triphenylphosphine)palladium (2.0 mg, 1.73 μmol) and sodium carbonate (13.6 mg, 0.128 mmol) was dissolved in a 3:1 mixture of DME/water (0.22 ml). The mixture was heated overnight at 85°C. The crude mixture was cooled to room temperature, diluted in a mixture of acetonitrile/water and purified by reverse phase chromatography (HPLC) to obtain 10.2 mg of (NMe)KIRA6. TLC (CH_2Cl_2:MeOH, 95:5 v/v): R_f = 0.4; 1H NMR (300 MHz, Chloroform-d) δ 9.06 (m, 1H) , 8.63 (m, 1H) , 8.19 (d, *J* = 6.7 Hz, 1H), 8.05 (m, 1H), 7.68 (s, 1H), 7.56 – 7.46 (m, 3H), 7.18 (m, 3H), 7.01 – 6.95 (m, 1H), 3.08 (s, 3H), 1.58 (s, 9H); ESI-MS (m/z): [M]+ calcd. for $C_{29}H_{27}F_3N_6O$ ($M+H^+$): 533.2; found 533.6.

The purity of (NMe)KIRA6 was determined with two analytical RP-HPLC methods, using a Varian Microsorb-MV 100-5 C18 column (4.6 mm x 150 mm), and eluted with either H_2O/CH_3CN or H_2O/ MeOH gradient solvent systems (+0.05% TFA) run over 30 min. Products were detected by UV at 254 nm. (NMe)KIRA6 was found to be >95% pure in both solvent systems.

In vitro IRE1α* protein preparation, crosslinking, RNase and kinase assay

A construct containing the cytosolic kinase and RNase domains of human IRE1α (residues 469-977, IRE1α*) or equivalent IREα mutants was expressed in SF9 insect cells using the Bac-to-Bac baculovirus expression system (Invitrogen) as described [9]. λ-PPase (NEB)-treated dephosphorylated IRE1α* (dP-IRE1α*) was also prepared and all the crosslinking experiments were performed as described [9]. The RNase assay using 5'FAM-3'BHQ-labeled XBP1 single stem-loop minisubstrate (5'FAM-CUGAGUCCGCAGCACUCAG-3'BHQ, from Dharmacon), and the IRE1α* auto-phosphorylation kinase assay were both done as described [9]. The ability of KIRA6 to inhibit the catalytic activity of Erk2, JNK2, JNK3, PKA, and Pim1 was determined using previously reported assay conditions (Hill *et al*., 2012). Internally ^{32}P-labeled RNAs (mouse XBP1 RNA and Ins2 RNA, as described in [10], and rat rhodopsin mRNA) were also used as substrates. For time-course determination, IRE1α* proteins (16 nM) were incubated with or without 10 μM 1NM-PP1 for 20 min prior to addition of 20 nM radio-labeled RNAs. Reactions were quenched by addition of 4 M urea at different time points and then were subjected to urea 6% PAGE analysis. For the endpoint readings of APY29-mediated rescue of IRE1α* P830L RNase activity, 160 nM of IRE1α* (WT or P830L) was incubated with 20 μM APY29 and mixed with 13 nM radio-labeled mouse Ins2 RNA for 1hr reaction and subsequently resolved by urea 6% PAGE. Determination of KIRA6-mediated inhibition of WT IRE1α* was done by incubating16 nM IRE1α* and 20 nM radio-labeled mouse Ins2 RNA or 0.8 μM IRE1α* and 40 nM radio-labeled miR17 as described (Upton *et al*., 2012), or 0.33 μM IRE1α* and 20 nM radio-labeled rat

rhodopsin mRNA. The cleavage buffer and general manipulation are the same as described [9]. cDNA for rat rhodopsin was purchased from Invitrogen and amplified by PCR using primers: 5'-GAAATTAATACGACTCACTATAGGGGGTCCAGGTACATCCCCGAG-3' (forward) and 5'-TTAGGCTGGAGCCACCTGGCT-3' (reverse). RNA was *in vitro* transcribed, cleaved by IRE1α*, and the cleavage sites mapped as described [9].

REFERENCES

1. Takeuchi, O., Fisher, J., Suh, H., Harada, H., Malynn, B.A., and Korsmeyer, S.J. (2005). Essential role of BAX,BAK in B cell homeostasis and prevention of autoimmune disease. Proceedings of the National Academy of Sciences of the United States of America *102*, 11272-11277.
2. Lindsten, T., Ross, A.J., King, A., Zong, W.X., Rathmell, J.C., Shiels, H.A., Ulrich, E., Waymire, K.G., Mahar, P., Frauwirth, K., et al. (2000). The combined functions of proapoptotic Bcl-2 family members bak and bax are essential for normal development of multiple tissues. Molecular cell *6*, 1389-1399.
3. Szot, G.L., Koudria, P., and Bluestone, J.A. (2007). Murine pancreatic islet isolation. J Vis Exp, 255.
4. Li, H., Korennykh, A.V., Behrman, S.L., and Walter, P. (2010). Mammalian endoplasmic reticulum stress sensor IRE1 signals by dynamic clustering. Proc Natl Acad Sci U S A *107*, 16113-16118.
5. Lerner, A.G., Upton, J.P., Praveen, P.V., Ghosh, R., Nakagawa, Y., Igbaria, A., Shen, S., Nguyen, V., Backes, B.J., Heiman, M., et al. (2012). IRE1alpha induces thioredoxin-interacting protein to activate the NLRP3 inflammasome and promote programmed cell death under irremediable ER stress. Cell metabolism *16*, 250-264.
6. Lewin, A.S., Drenser, K.A., Hauswirth, W.W., Nishikawa, S., Yasumura, D., Flannery, J.G., and LaVail, M.M. (1998). Ribozyme rescue of photoreceptor cells in a transgenic rat model of autosomal dominant retinitis pigmentosa. Nature medicine *4*, 967-971.

7. McGill, T.J., Prusky, G.T., Douglas, R.M., Yasumura, D., Matthes, M.T., Nune, G., Donohue-Rolfe, K., Yang, H., Niculescu, D., Hauswirth, W.W., et al. (2007). Intraocular CNTF reduces vision in normal rats in a dose-dependent manner. Invest Ophthalmol Vis Sci *48*, 5756-5766.

8. Chintinne, M., Stange, G., Denys, B., In 't Veld, P., Hellemans, K., Pipeleers-Marichal, M., Ling, Z., and Pipeleers, D. (2010). Contribution of postnatally formed small beta cell aggregates to functional beta cell mass in adult rat pancreas. Diabetologia *53*, 2380-2388.

9. Wang, L., Perera, B.G., Hari, S.B., Bhhatarai, B., Backes, B.J., Seeliger, M.A., Schurer, S.C., Oakes, S.A., Papa, F.R., and Maly, D.J. (2012). Divergent allosteric control of the IRE1alpha endoribonuclease using kinase inhibitors. Nature chemical biology *8*, 982-989.

10. Han, D., Lerner, A.G., Vande Walle, L., Upton, J.P., Xu, W., Hagen, A., Backes, B.J., Oakes, S.A., and Papa, F.R. (2009). IRE1alpha kinase activation modes control alternate endoribonuclease outputs to determine divergent cell fates. Cell *138*, 562-575.

Publishing Agreement

It is the policy of the University to encourage the distribution of all theses, dissertations, and manuscripts. Copies of all UCSF theses, dissertations, and manuscripts will be routed to the library via the Graduate Division. The library will make all theses, dissertations, and manuscripts accessible to the public and will preserve these to the best of their abilities, in perpetuity.

Please sign the following statement:

I hereby grant permission to the Graduate Division of the University of California, San Francisco to release copies of my thesis, dissertation, or manuscript to the Campus Library to provide access and preservation, in whole or in part, in perpetuity.

Eric Wang
Author Signature

6/24/2015
Date